NANO-STRUCTURED MEMBRANES FOR CLEAN ENERGY HARVESTING FROM SALINITY GRADIENT AND LOW-GRADE WASTE HEAT

A Dissertation
Presented to
The Academic Faculty

by

Xin Tong

In Partial Fulfillment
of the Requirements for the Degree
Doctor of Philosophy in the
School of Civil and Environmental Engineering

Georgia Institute of Technology

December 2018

NANO-STRUCTURED MEMBRANES FOR CLEAN ENERGY HARVESTING FROM SALINITY GRADIENT AND LOW-GRADE WASTE HEAT

Approved by:

Dr. Yongsheng Chen, Advisor
School of Civil and Environmental Engineering
Georgia Institute of Technology

Dr. Ching-Hua Huang
School of Civil and Environmental Engineering
Georgia Institute of Technology

Dr. John Crittenden
School of Civil and Environmental Engineering
Georgia Institute of Technology

Dr. Ryan Lively
School of Chemical and Biomolecular Engineering
Georgia Institute of Technology

Dr. Xing Xie
School of Civil and Environmental Engineering
Georgia Institute of Technology

Date Approved: August 9, 2018

“The mind is not a vessel to be filled, but a fire to be kindled.”

— Plutarch

ACKNOWLEDGEMENTS

First, my deepest gratitude to Dr. Yongsheng Chen for his invaluable mentoring and continuous guidance throughout my Ph.D. study. His tremendous advice, support, and encouragement during the years not only steered me on track but also helped to shape my future career path.

I would also like to thank my Ph.D. committee members, Dr. John Crittenden, Dr. Ching-Hua Huang, Dr. Xing Xie and Dr. Ryan Lively for their precious time and comments on my research. My special thanks to Dr. Guangxuan Zhu for his support of lab management and technical assistance.

The Ph.D. study is like rowing upstream, I was fortunate to be surrounded by talented and hard-working collaborators. It was a great journey to work and grow together with the graduate students, postdocs and visiting scholars in my research group.

I would like to express my great thanks to my friends in the Georgia Tech community and in Atlanta, I appreciate their kindness, support, and generosity. My life is so blessed with some of those most amazing people.

The last but not the least, my biggest thanks go to my family for their support and faith in me. Life without you guys wouldn't be the same and neither would I. Last but not the least, I thank my lovely girlfriend, Su, for being the light in the darkest of times of mine.

TABLE OF CONTENTS

LIST OF TABLES

LIST OF FIGURES

LIST OF ABBREVIATIONS

AEM	Anion exchange membrane
AFM	Atomic force microscopy
CD	Fixed charge density
CEM	Cation exchange membrane
CNT	Carbon nanotube
CP	Concentration polarization
DI	Deionized
DMSO	Dimethyl sulfoxide
DS	Degree of sulfonation
ECP	External concentration polarization
ED	Electrodialysis
EDX	Energy dispersive X-ray spectroscopy
FC	Fuel cell
FE-SEM	Field emission scanning electron microscope
FTIR	Fourier transform infrared

GO	Graphene oxide
GOM	Graphene oxide membrane
ICP	Internal concentration polarization
IEC	Ion exchange capacity
IEM	Ion exchange membrane
MFC	Microbial fuel cell
NMP	N-Methyl-2-pyrrolidone
NP	Nanoparticles
OCV	Open circuit voltage
O-WMCNT	Oxidized multi-walled carbon nanotube
PPO	Poly(2,6-dimethyl-1,4-phenyleneoxide)
PRO	Pressure retarded osmosis
RED	Reverse electrodialysis
RFB	Redox flow battery
RO	Reverse osmosis
SD	Swelling degree
SGP	Salinity gradient power

SPPO Sulfonated poly(2,6-dimethyl-1,4-phenyleneoxide)

XRD X-ray diffraction

SUMMARY

Efficient access to clean and renewable energy is a top global challenge in the 21st century. Global warming and population growth make the situation even more challenging and complex. Membrane technology holds great potential to harvest clean energy from untapped or underutilized energy sources. The objective of this research is to design advanced membranes by using nanomaterials and/or polymeric materials for several emerging membrane-based technologies that can harvest clean and renewable energy.

Reverse electrodialysis (RED) is an ion-exchange membrane-based process that can extract useful work from salinity gradients. As key part of the RED system, ion exchange membranes (IEMs) are important factors to the success of future RED energy generation. This work presents the synthesis and characterization of a new kind of nanocomposite cation exchange membrane (CEM) by using multi-walled carbon nanotubes (CNTs) and sulfonated poly(2,6-dimethyl-1,4-phenyleneoxide) (SPPO). The nanocomposite CEMs showed simultaneous improvement of membrane anti-fouling performance and energy generation performance in the RED system.

The origin of nanocomposite IEM property enhancement is far from being fully understood. By combining experimental work and computational modeling analysis, we were able to determine the influence of nanomaterials on the ion transport properties of nanocomposite CEMs. Modeling analysis suggests that the change of membrane properties is related to the change in membrane microstructure. With the addition of silica NPs, membrane porosity (volume fraction of intergel phase) increases so that membranes can absorb more water. Also, the volume fraction of sulfonated polymer segments increases,

which can allow membranes to retain more counterions, leading to the increase of the membrane ion exchange capacity (IEC). By calculating the effective ion diffusion coefficients and membrane tortuosity factors of all the silica-NP-based nanocomposite CEMs synthesized in this study, along with nanocomposite CEMs from previous studies, we determined that membrane ion transport efficiency tends to increase with the incorporation of nanomaterials.

Pressure retarded osmosis (PRO) is also a membrane-based technology used to extract salinity gradient power (SGP). The progress of PRO is largely hindered by the absence of cost-efficient high-performance membranes. This work demonstrates the application of freestanding graphene oxide membranes (GOMs) that can obtain high water flux and high-power density. Due to the elimination of membrane support layer, the effective driving force across the freestanding membrane can increase, thus both the water flux and power density increase. This study represents a step forward towards the large-scale application of PRO for electricity generation.

A membrane-based osmotic heat engine is a hybrid system to harvest low-grade waste heat energy. PRO is integrated into the hybrid system for energy production. This work demonstrates that the freestanding GOM can significantly increase the power density of the osmotic heat engine. Our experimental results and analysis show that the freestanding GOMs are also suitable for the newly emerged application.

This dissertation presents advances for ion exchange and osmotic-driven membrane development. The fundamental study of the nanocomposite IEMs has yielded significant findings that enhance our mechanistic understanding of the type of membranes. The

development of a new generation of membranes can serve to inform the energy potential of the emerging membrane-based technologies. The implications of the dissertation are potentially far-reaching and are anticipated to shape the discussion on membrane-based technology for renewable energy production.

CHAPTER 1. RESEARCH OBJECTIVES

1.1. Motivation

Efficient access to clean and renewable energy to meet the world's increasing energy demand is a top global challenge in the 21st century. The current global energy demand far exceeds the present ability for clean energy production. More importantly, the rapid global population growth and the accompanying rising economic growth, mainly in Asia and Africa, will place additional demand on energy supply [1]. The current excessive reliance on fossil fuels to generate energy is untenable because of greenhouse gas emissions from the combustion of fossil fuels. Since the industrial revolution, the atmospheric concentrations of greenhouse gas have escalated to the point that significant global warming cannot be ignored [2]. Pollution caused by combustion of fossil fuels is another area of major concern. A July 2018 Worldwatch Institute report cited a World Bank study, which projected that "on average 1.8 million people would die prematurely each year between 2001 and 2020 because of air pollution" [3]. The CO_2, sulfuric acid, soot, and other pollutants that hover over our cities worldwide continue to make our air unhealthy and unsafe.

To reduce our dependence on fossil fuel, one promising strategy is to develop sustainable energy technologies. Up to now, many different sustainable energy sources have been investigated, and some have become an important supplement to fossil fuels, which include solar energy, wind energy, biomass energy, etc. However, to achieve a shift towards a more sustainable energy future, more efforts are needed to advance the current sustainable energy technologies, and at the same time, explore the sustainable energy

sources that have previously been overlooked or underutilized. In addition, energy is inextricably intertwined with water, another precious resource necessary to the human society. The principle of water-energy nexus suggests that energy is needed to produce adequate amount of clean water, and water is necessary to ensure a consistent production of energy [4]. In the light of the above, enough clean energy production is also necessary to further secure the supply of enough clean water.

Salinity gradient power (SGP) is a type of sustainable energy that has not been fully explored. When two solutions of different salinities (i.e., salt concentrations) are mixed together, Gibbs free energy is released. Chemical potential difference between salty water and fresh water can be an endless supply of energy. With respect to the natural environment, SGP can be generated when river water and seawater are mixed at the intersection of river estuaries and oceans. An estimation suggests that the total global potential for energy generation from the above source is 2.4–2.6 terawatts (TW) [5], which is more than 80% of the current global electricity demand. SGP can also be generated from an even higher salinity gradient, such as the mixing of desalination brine with wastewater. The natural salinity gradient power represents a huge amount of untapped clean energy which can diversify and strength our energy portfolio. Besides, SGP can be generated from engineered salinity gradients, one such example is the recovery of low-grade waste heat via a membrane-based osmotic heat engine [6]. Low-grade waste heat represents another underutilized energy source. In the U.S., more than 30% of the energy supply is consumed by industrial processes. About 50% of all the consumed energy is released to the environment in the form of waste heat [7]. A large portion of the waste heat has a low temperature and thus is difficult to be recovered via the existing technologies, such as

Organic Rankine cycles. The development of the osmotic heat engine aims to recover the low-grade waste heat (the waste heat with a low temperature, typically < 130 °C).

1.2. Research objectives

The overarching objective of this research is to advance several membrane-based energy generation technologies, including reverse electrodialysis (RED), pressure retarded osmosis (PRO) and osmotic heat engine to ensure efficient energy production (SGP). Although the concept of harvesting SGP from the mixing of two solutions of different salinities was proposed more than half-century ago [8], significant technological progress is needed to realize large-scale application. Membrane, as a key component in the above systems, can determine the effectiveness and efficiency of energy generation. The study focuses on the development of new membranes based on the desired membrane properties that each technology needs. Since nanotechnology has the potential to control and/or improve the transport of molecules or ions at the nanoscale [9], the current study takes advantage of nanotechnology to design and synthesize nano-structured membranes for the application in the above membrane-based technologies. Various nano-materials are used to synthesize either organic-inorganic nanocomposite membranes or inorganic nano-material based membranes. In addition, the theoretical study of the nanoscale structure-property relationship of the nanocomposite membranes is also conducted.

The specific targets of the dissertation are:

1. Fabricate nanocomposite cation exchange membranes (CEMs) capable of simultaneously achieving high power density and anti-fouling in the RED system.

2. Explore the origin of property enhancement of the nanocomposite ion exchange membrane (IEM) by combing experimental work and theoretical modeling.
3. Demonstrate the fabrication of freestanding graphene oxide membranes (GOMs) to minimize membrane internal concentration polarization (ICP) and increase power density in PRO.
4. Investigate the freestanding GOMs in membrane-based osmotic heat engines for low-grade waste heat recovering with enhanced power density.

1.3. Organization of the dissertation

The dissertation begins with an introduction of membrane-based technologies for the salinity gradient power and low-grade waste heat harvesting. In Chapter 2, the working principles of reverse electrodialysis, pressure retarded osmosis and osmotic heat engine are briefly described. The properties of corresponding membranes working in the systems are presents, and the technical challenges of the technologies are discussed.

Chapter 3 focuses on the synthesis and characterization of carbon nanotube-based cation exchange membranes. The transport properties of the membrane are extensively characterized, and the power generation property of the membrane in the RED system is investigated. The study demonstrates that by adding nanomaterials in the cation exchange membrane, the ion transport and power generation performance in the RED system of the membrane becomes more efficient.

Chapter 4 explores the origin of the property enhancement by adding nanomaterials into the ion exchange membranes. A series of nanocomposite cation exchange membranes are synthesized by adding silica nanoparticles into the polymer material. The study shows

that the change of the nanoscale structure of the membrane by adding the nanoparticles is responsible for the increase of membrane transport properties. This study provides valuable guidance for future design and synthesis of nanocomposite ion exchange membranes for various applications.

Chapter 5 turns the focus towards the synthesis and application of freestanding graphene oxide membranes in the PRO system. This study demonstrates that due to the ability to minimize internal concentration polarization in the osmotic-driven process, the graphene oxide membrane can increase the water flux and power density in the PRO system. This study proposes a new way of designing membranes for application of the osmotic-driving membrane process including PRO.

Chapter 6 investigates the application of the freestanding graphene oxide membranes in a membrane-based osmotic heat engine. Like the previous chapter, since the graphene oxide membrane does not have a support layer, the membrane internal concentration polarization can be minimized. As a result, a higher power density can be obtained from the osmotic heat engine.

Lastly, Chapter 7 summarizes the main findings of the dissertation, and offer perspectives on the future research directions.

1.4. Originality and Merit of the Research

The findings of this dissertation are original and provide a better understanding of both the energy generation systems and the membranes. More specifically, the information obtained from this study is dedicated to the development of membranes with better

properties for the salinity gradient power and low-grade waste heat generation from the following aspects:

(1) development of nanocomposite ion exchange membranes to meet the challenges in the RED system, i.e., enhancement of power density and anti-fouling,

(2) exploring the mechanism of transport property enhancement of nanocomposite ion exchange membranes, and

(3) application of graphene oxide to synthesize a new type of osmotic-driven membrane for the application in PRO and osmotic heat engine systems.

CHAPTER 2. INTRODUCTION

When two solutions with different salinities (i.e., salt concentrations) mix together, the Gibbs free energy of mixing is released. The above phenomenon represents an new type of renewable energy that is available worldwide, which is called salinity gradient power (SGP). The SGP can be generated wherever two solutions of different salinities mix, for example where river water flows into the sea, or concentrated brine is discharged into the river. An estimation suggests that the total global potential for energy generation from the mixing of river water with seawater is 2.4-2.6 terawatts (TW), which is more than 80% of the current global electricity demand [5]. In addition to the large total amount of energy available globally, the high energy density of the SGP also makes it an attractive renewable energy candidate. The amount of energy available from the mixing of 1 m^3 of concentrated and 1 m^3 of diluted solutions can be as high as 17 MJ, depending on the concentration difference of the two solutions [10]. Also, during the energy production process, there is no production of greenhouse gas or pollutants.

Membrane-based technologies have been developed to control the process of mixing and harvest the SGP. Different from some conventional membrane-based processes that performing separations, such as microfiltration, ultrafiltration, nanofiltration and reverse osmosis (RO), the emerging membrane-based processes to produce the SGP are controlled mixing processes. The emerging membrane-based processes convert Gibbs free energy released from the mixing of different solutions into useful works via controlling the transport of water molecules or salt ions.

By regulating the ion transport of different charges, osmotic ionic flux can be generated inside the membrane system. The ionic flux can then be converted to electron flow; thus, electricity can be generated. The above membrane technology is call reverse electrodialysis (RED). In the RED system, two different types of membranes are needed. Cation exchange membranes (CEMs) contain negatively charged functional groups inside the membrane matrix, thus only allowing cations to pass through; Anion exchange membranes (AEMs) contain positively charged functional groups and thus have the opposite transport properties. The two types of ion exchange membranes (IEMs) (i.e., CEMs and AEMs) help with the controlled mixing process and generate power. Specifically, the CEMs and AEMs are set alternatively to create water channels in the membrane system. Also, two electrodes are set at the two ends of the membrane system. When salty water and fresh water are pumped into the membrane system, chemical potential difference drives ions to transport from the salty water into the fresh water. The membranes can control the directions of ion transport and create a consistent ionic flux inside the system. The ionic flux can then be converted to electron flow by using two end-electrodes, and thus electricity can be generated (Figure 1). The principle and system configuration of the RED will also be discussed in Chapter 3.

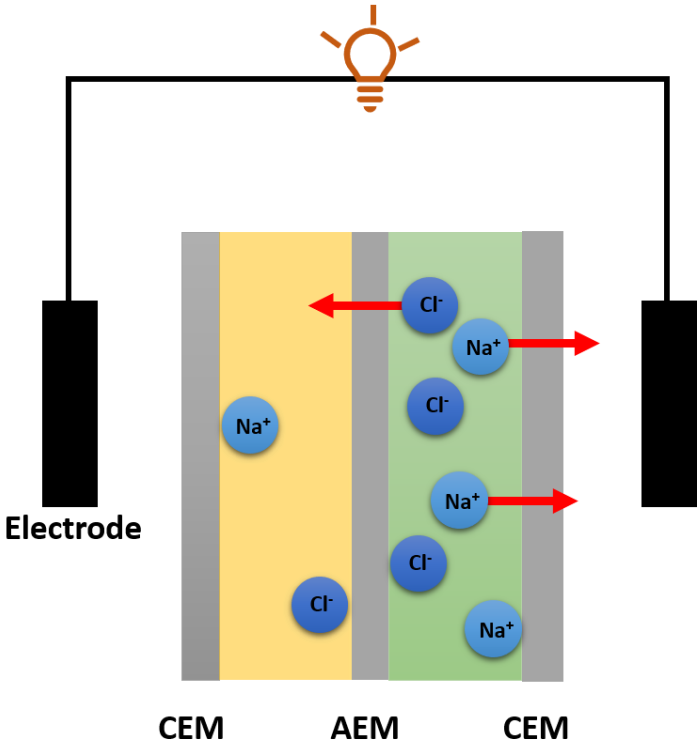

Figure 1 – Simplified scheme of reverse electrodialysis (RED) system.

Alternatively, the Gibbs energy of mixing can be utilized to produce pressurized water flow by selectively concentrating water molecules with the help of a semi-permeable membrane. The kinetic energy from the pressurized water is then converted to electricity by using a mechanical turbine. The above membrane technology is called pressure retarded osmosis (PRO). The PRO is closely related to reverse osmosis (RO) and forward osmosis (FO) (Figure2). In the RO system, a large external hydraulic pressure (ΔP_1) is applied to

push the salty water against a semi-permeable membrane to overcome the osmotic pressure difference. Water molecules can penetrate the membrane and salt ions are rejected by the membrane. At the other side of the membrane, clean water can be produced (Figure 2a). The FO process utilizes osmotic pressure different between the salty water and fresh water as a driving force. Due to the osmotic pressure difference, water molecules transport from the fresh water (feed solution) side to the salty water (draw solution) side (Figure 2b). After separating the clean water with the diluted draw solution, clean water is produced and draw solution with high osmotic pressure is re-generated. Like the FO process, the PRO process also uses osmotic pressure difference as the driving force. However, a small external hydraulic pressure (ΔP_2, smaller than the osmotic pressure difference) is applied at the salty water side to slow down the water transport. When water molecules are "concentrated" at the salty water side, the volume, flow rate and the kinetic energy of the salty water increase. Then, a mechanical turbine is applied in the system to convert the kinetic energy of the salty solution into electricity (Figure 2c). The principle and system configuration of the PRO system will also be discussed in Chapter 5.

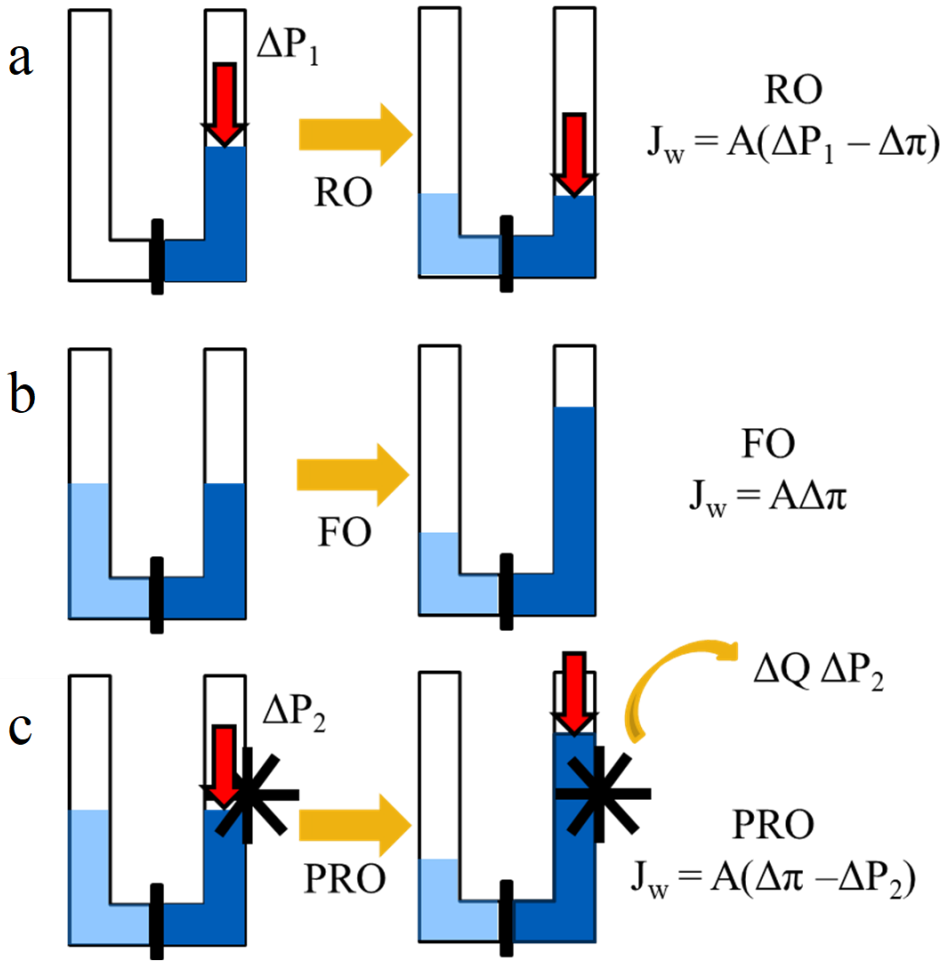

Figure 2 - Scheme of (a) reverse osmosis (RO), (b) forward osmosis (FO) and (c) pressure retarded osmosis (PRO).

Both the above technologies utilize membranes as semi-permeable barriers to realize the controlled mixing; however, significant differences exist between them. The RED uses permselective IEMs to produce osmotic ionic current; while the PRO relies on the production of pressurized water flow. Despite the significant differences in working

principles, the two technologies can both be used to generate electricity from various natural salinity gradients. In addition, the membrane-based technologies can also be incorporated into hybrid systems to harvest other untapped energy forms. Through the design of engineered systems, the so-called membrane-based osmotic heat engine has been invented aiming to recover low-grade heat from various sources (Figure 3) [6].

The osmotic heat engine utilizes engineered salinity gradient, the salinity gradient created by human, as an energy source. In the system, the energy generation component is a PRO setup, converting engineered salinity gradient into electricity. The thermal separation component re-generates the concentrated and diluted solutions by using the low-grade waste heat as an energy source. The hybrid and closed-loop system can thus ensure a continuous generation of electricity.

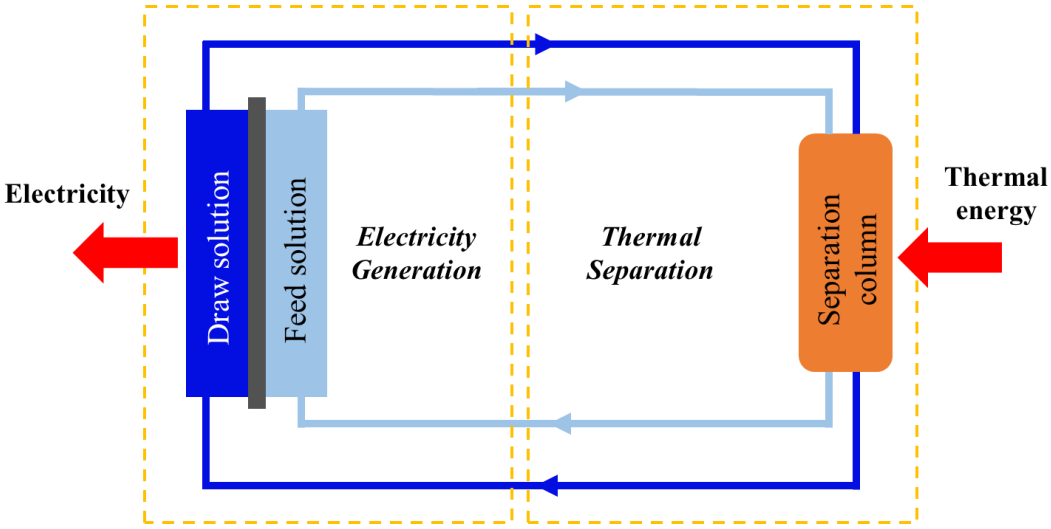

Figure 3 - Schematic illustration of a membrane-based osmotic heat engine for low-grade waste heat harvesting.

Despite the state-of-the-art design of the above membrane-based system, none of the technologies in its current form can be applied in a large scale to harvest energy. Low power generation performance became a concern in those energy generation systems. Adequate membranes are needed to make the energy generation processes more effective. For the RED system, IEMs with lower ionic resistance and higher permselectivity are needed to increase the power density. For the PRO system, the membrane concentration polarizations (internal concentration polarization and external concentration polarization) and reverse salt flux have negative impact on the power generation. To increase the power generation performance in the PRO system, semi-permeable membranes with higher water permeability and lower salt permeability coefficient is needed. In addition, strategies to

reduce the internal concentration polarization is urgently needed, since the internal concentration polarization is the major “self-limiting factor” in the osmotic-driven system. Since the energy generation component of the osmotic heat engine share the same principle with the PRO system, a membrane with low concentration polarization and low salt permeability coefficient is also necessary to enhance the power generation performance of the osmotic heat engine.

CHAPTER 3. FOULING RESISTANT NANOCOMPOSITE CATION EXCHANGE MEMBRANE WITH ENHANCED POWER GENERATION FOR REVERSE ELECTRODIALYSIS

3.1. Abstract

Renewable energy can be generated from the mixing of seawater with river water by reverse electrodialysis (RED). As part of the RED system, ion exchange membranes (IEMs) are key factors to the success of future RED energy generation. This research presents the synthesis and characterization of a new kind of nanocomposite cation exchange membrane (CEM) by using oxidized multi-walled carbon nanotubes (O-MWCNTs) blended with sulfonated poly (2,6-dimethyl-1,4-phenylene oxide) (SPPO). The nanocomposite CEM showed simultaneous improvement of membrane anti-fouling performance and energy generation performance in RED systems. The physicochemical and electrochemical properties of nanocomposite CEMs were enhanced compared to pristine SPPO CEMs. The results indicated that the optimal inorganic loadings were 0.3–0.5 wt %, which showed the best anti-fouling performance and highest power density in RED. The results show that O-MWCNTs are promising materials to improve properties of IEMs, and nanocomposite IEMs are competitive candidates for application in electrochemical systems like RED.

3.2. Introduction

Salinity gradient power, the energy harvested from the mixing of two aqueous solutions with different salt concentrations, is thought to be a clean energy source that can

fulfill the current global electricity demand [8, 10-12]. The free energy that comes from mixing river water with seawater equals what could be released from a 280-meter waterfall [8, 12]. Different technologies have been developed for capturing salinity gradient energy, which includes pressure retarded osmosis (PRO) [13], reverse electrodialysis (RED) [14, 15], electrochemical capacitive method [16] and a few less developed technologies [17-19]. Among those technologies, RED is dedicated to harvesting energy from the mixing of seawater and river water [5, 15], and it has seen tremendous development in recent years. In the RED system, concentrated and diluted water flows are separated by ion exchange membranes (IEMs). Positively and negatively charged ion species transport from concentrated water to diluted water through cation exchange membranes (CEMs) and anion exchange membranes (AEMs), respectively. Using alternating series of CEMs and AEMs separated by spacers, continuous ion flux can be maintained inside the RED stack. The ion flux is then converted to electric current on the surface of electrodes via redox reactions; therefore, a closed circuit could be formed, and power generated.

Low energy efficiency, low power density, and membrane fouling problems are major issues that prevent the commercialization of RED. IEM has an important role to play regarding those issues. As key components, IEMs are required to have low ionic resistance and high permselectivity in RED systems [14, 20]. Ionic resistance and permselectivity of IEMs characterize the tendency to resist ion flux transport, and the ability to transport counter-ions and exclude co-ions, respectively [20]. Despite the importance of IEMs, most previous studies on RED have focused on stack design and system optimization [21-25]. The lack of cost-effective IEMs with low ionic resistance and high permselectivity for high energy generation has become a major challenge towards the implementation of the

technology [21, 26]. Also, IEM fouling has also prevented RED from large-scale applications [27, 28]. It has been reported that without specific anti-fouling strategies, power density could decrease by as much as 60% in the first four hours of operation [29]. In a RED system, AEMs are more prone to organic fouling, whereas CEMs are significantly affected by inorganic fouling and scaling [27]. Fouling-resistant AEMs has been synthesized for different applications, mostly by increasing the hydrophilicity and/or negatively charge density of their membrane surface [30-32]. However, work that attempts to synthesize inorganic fouling-resistant CEMs is extremely scarce, which might be due to the lack of clear, easy, and effective anti-fouling strategies for CEMs. Research focusing on electrodialysis (ED) showed that scaling can become a severe problem especially in the presence of calcium and carbonate species [33, 34]. Although some efforts have been made to develop RED-specific IEMs on a lab scale, for enhancing power generation and/or diminishing the influence of fouling [27, 35-40], much more work needs to be done in order to lower the cost as well as further enhance the properties of IEMs.

Recently, many studies on membrane technology have focused on inorganic and organic nanocomposites [35, 41-44]. Nanocomposite materials have become increasingly important due to their extraordinary properties, which arise from the synergism between the properties of both inorganic and organic components [43-45]. Carbon nanotubes (CNTs) are one type of inorganic nanomaterial that has gained a lot of attention due to their high flexibility, low mass density, large aspect ratio, excellent mechanical property, and good electronic conductivity [46-48]. For the properties of CNT to transfer to CNT-based composites, CNTs should be homogeneously dispersed in the composites [47]. Aggregation of CNTs has become a major obstacle in their application. Research has been

conducted to achieve a homogeneous dispersion of CNT nanocomposites, which is primarily accomplished through the functionalization of CNTs [46-49]. The functionalization of CNTs via covalent or noncovalent attachment of functional groups onto the surface of CNTs [49] can enhance the dispersion property and improve chemical affinity within the polymer matrices [46]. Covalent functionalization of CNTs can be accomplished by attaching carboxyl groups or hydroxyl groups onto the CNTs surface via oxidation reactions, which is commonly referred to as the oxidation of CNTs [48]. The presence of oxygen-containing groups ($-COOH$ and/or $-OH$) has been reported to increase the solubility and dispersion property of CNTs in an organic solvent [47, 50] as well as increase the possibility for further functionalization depending on the specific application [47]. For the use of CNTs as inorganic fillers in nanocomposite polymers, the incorporation of oxygen-containing functional groups is crucial for the enhancement of interfacial adhesion, by which the unique properties of CNTs can be transferred to the composites [47]. As one- dimensional nanomaterials, CNTs have a great advantage over the application of nanocomposite IEMs, compared to zero-dimensional nanomaterials (titanium oxide, iron oxide, silica oxide nanoparticles, etc.). It has been reported that ion pathways exist at the interface of nanomaterials and polymer; hence, long-distance ionic pathways could be formed when elongated nanomaterials (nanotubes or nanofibers) are used [51]. Long-distance ionic pathways largely improve membrane inner structure and facilitate ion transport. In addition, oxidized multi-walled CNTs (O-MWCNTs) were found to effectively improve the anti-fouling properties of pressure-driven membranes due to their ability to change membrane surface morphology, surface charge density and hydrophilicity [52, 53].

In the present work, a new type of nanocomposite CEM for RED applications was prepared via a blending method, in which O-MWCNTs were dispersed in sulfonated poly (2,6-dimethyl-1,4-phenylene oxide) (SPPO) to form polymer nanocomposites. PPO is an attractive and proven candidate with good chemical and thermal stability as well as mechanical properties [35, 54-56]. SPPO, which is produced by introducing sulfonic acid groups into the PPO polymer chains through sulfonation reactions, has been extensively used for synthesizing CEMs [35, 55, 57, 58]. O-MWCNTs were chosen due to their enhanced dispersion property and better chemical compatibility with polymers compared to pristine CNTs. O-MWCNTs were also chosen for their potential to improve membrane ion transport property and anti-fouling performance. The authors initiated the first use of CNTs to make nanocomposite CEMs for simultaneously improving the anti-fouling performance and enhancing the power generation in the RED system. The physicochemical and electrochemical properties of all the nanocomposite CEMs with different O-MWCNT loadings were extensively characterized. The anti-fouling properties of CEMs were also investigated by using an original custom-designed testing process. The effect of O-MWCNT loadings was investigated to optimize the integrated membrane power generation performance in the RED system.

3.3. Materials and Methods

3.3.1. Materials

PPO (Aldrich, analytical standard) was used as received for preparing SPPO. Chloroform (Aldrich, anhydrous, 99%) was used as a solvent, and chlorosulfonic acid (Aldrich, 99%) was used as a sulfonation agent. Dimethyl sulfoxide (DMSO) (VWR, ACS

grade, 99.9%) was used as received. O-MWCNTs (purity > 95 wt %) with an outer diameter of 1020 nm, a length of 10–30 μm, and a carboxyl group content of 2.00 wt % were purchased from Cheap Tubes and had been oxidized by the manufacturer. The O-MWCNTs were also used as received.

3.3.2. Preparation of cation exchange membranes

The PPO was sulfonated by following the process described in a previous work [35]. 6 wt % of PPO was dissolved in chloroform while stirring vigorously for 30 minutes at room temperature. The chlorosulfonic acid solution was used as the sulfonation agent. 8 wt % of the chlorosulfonic acid solution in chloroform was slowly added into the PPO-chloroform solution. Then the precipitated SPPO was filtered and washed with DI water several times until the pH became approximately neutral. The SPPO obtained from the previous step was dissolved into methanol and stirred for one hour to form a homogeneous solution. The polymer solution was then poured into a Pyrex glass plate to form a thin layer with a thickness of no more than 2 mm. The thin layer was allowed to air-dry in a fume hood at room temperature for 48 h. The dried SPPO was then cut into small pieces and stored for future use.

The CEMs were prepared by a blending method. Known amounts of O-MWCNTs (0–1.5 wt %, according to different loadings) were dispersed into 24 grams of DMSO. The mixture was sonicated for 1 h to get a well-dispersed suspension. Six grams of SPPO was dissolved in the suspension and stirred for 48 h to obtain homogeneous blending. The membranes marked as 0.1 wt % O-MWCNT (or SPPO-0.1 O-MWCNT) indicate that the membranes were prepared by blending with an O-MWCNT content of 0.1 wt % with respect to SPPO. The resulting mixture was sonicated for 30 min to remove bubbles and

then cast onto glass plates by using a doctor blade with a desired thickness. To remove any residual solvent, membranes were dried in a vacuum oven at 60 °C for 36 h. The resulting membranes were peeled off the plates by soaking in warm water at 30 °C and then conditioned in 1 M of HCl solution for 24 h. Finally, the membranes were rinsed with DI water and equilibrated in 0.5 M of NaCl solution for future characterization.

3.3.3. Membrane characterizations

A Fourier transform infrared (FTIR) spectrometer (Digilab FTS7000) was used to obtain the FTIR spectra of membrane materials. A resolution of 4 cm^{-1} and a spectra range of 4000–650 cm was applied.

Field emission scanning electron microscopy (FE-SEM) (Hitachi SU8230) was used to characterize the morphology of nanocomposite CEMs. Dried membrane samples were used. For the membrane cross-section characterization, the samples were prepared by soaking membranes into liquid nitrogen and cutting them manually to get sharp cross sections. O-MWCNTs were also characterized by using FE-SEM.

Atomic force microscopy (AFM) (Agilent 5500, Agilent Technologies, Inc., US) was used to further characterize the surface morphology and roughness. Membrane surface morphology images and roughness parameters were obtained. At least three measurements were conducted for each membrane sample.

Ramé-hart Model 250 goniometer (Ramé-hart Instrument Co.) was used to measure the water contact angle. At least three measurements were conducted immediately after the 2 μL droplet was placed onto the dried membrane surface, and at least two different locations were chosen for each sample. The average was reported.

Surface charge measurement was determined by using a titration method that has been reported before [59]. The membrane was treated with 1 M of HCl to replace Na^+ by H^+. Then the membrane surface was rinsed with DI water until the pH of rinsing water was determined to be approximately neutral. The membrane was soaked in 0.01 M NaOH for 1 min to undergo surface ion replacement. The remaining NaOH solution was titrated with 0.1 M of HCl. The surface charge density (meq/ m^2) was calculated by the amount of NaOH used to neutralize H^+ on the membrane surface divided by the membrane surface area. All the membrane dimensions were 4 cm × 9 cm, and the procedures were kept exactly the same for all the membranes that were under investigation.

Swelling degree (SD), ion exchange capacity (IEC), fixed charge density (CD), ionic resistance and permselectivity of all the nanocomposite CEMs were characterized by using previously reported methods [35, 39]. Properties of two commercial CEMs, CSO (SELEMION®, AGC Engineering Co., Ltd., Japan) and FKS (Fumasep®, Fumatech, Germany) were also characterized for comparison. The measured membrane permselectivity is apparent permselectivity, meaning the potential difference across the membranes between two solutions with different NaCl concentrations (0.1 M and 0.5 M). A detailed description of characterization methods is provided in Appendix A.

3.3.4. Membrane anti-fouling property

The anti-fouling testing was carried out by using a RED stack described previously (which was also used for RED power performance measurement in this study) [35, 37], as shown in Figure 4. The RED stack used in the anti-fouling test consists of seven and a half cell pairs, each containing a CEM and an AEM. The CEMs under investigation were set in a specific order as indicated in Figure 4. AEMs (Fumasep® FAS, Fumatech, Germany)

were set in between adjacent CEMs. All the synthesized CEMs were tested at the same time; commercial CSO was also tested for comparison. An extra CSO membrane was placed as a shielding membrane to prevent negatively charged species from entering the stack. The effective area of all the membranes was 9 cm × 4 cm. The intermembrane distance (cell width) was maintained by a woven fabric gasket spacer with a thickness of 500 μm. The porosity of the spacers was 60%. Two endplates equipped with titanium mesh end electrodes (coated with iridium plasma) were used as cathode and anode, respectively. 0.5 M of NaCl solution was used as the rinse solution in the electrode compartments.

Two different groups of model solutions were used for two test runs. The composition of two model solutions is listed in Table 1. The Test 1 model solutions were prepared based on the actual compositions of natural seawater and river water. Solutions used in Test 2 were pure NaCl solutions, which served as the control group. The solutions were delivered into chambers using peristaltic pumps. The total inflow rate was maintained at 0.38 L/ min, for both concentrated and diluted water. The inflow then separated into seven flows (one for each cell pair), each with the same flow rate (theoretically) when it entered the stack (Figure 4). A constant applied voltage of 10.52 V was maintained, to speed up the ion exchange from concentrated water to diluted water. Each group of anti-fouling tests was operated continuously for two hours. Under the applied voltage, the system might be in the electroconvection region [60, 61]. Current changes were monitored during the whole-time ranges. Permselectivity and ionic resistance of all the CEMs in Test 1 were measured after the test. The measured results were compared to those of unused membranes to identify the change of membrane properties as well as assess how well the CEMs can resist inorganic fouling.

Table 1 - Composition and concentration of model solutions used in anti-fouling tests

Test	Concentrated water	Diluted Water
Test 1	NaCl (0.5 M) $CaCl_2$ (0.01 M) $NaHCO_3$ (2.5×10^{-3} M)	NaCl (0.017 M) $CaCl_2$ (3.8×10^{-4} M) $NaHCO_3$ (9.6×10^{-4} M)
Test 2	NaCl (0.5 M)	NaCl (0.017 M)

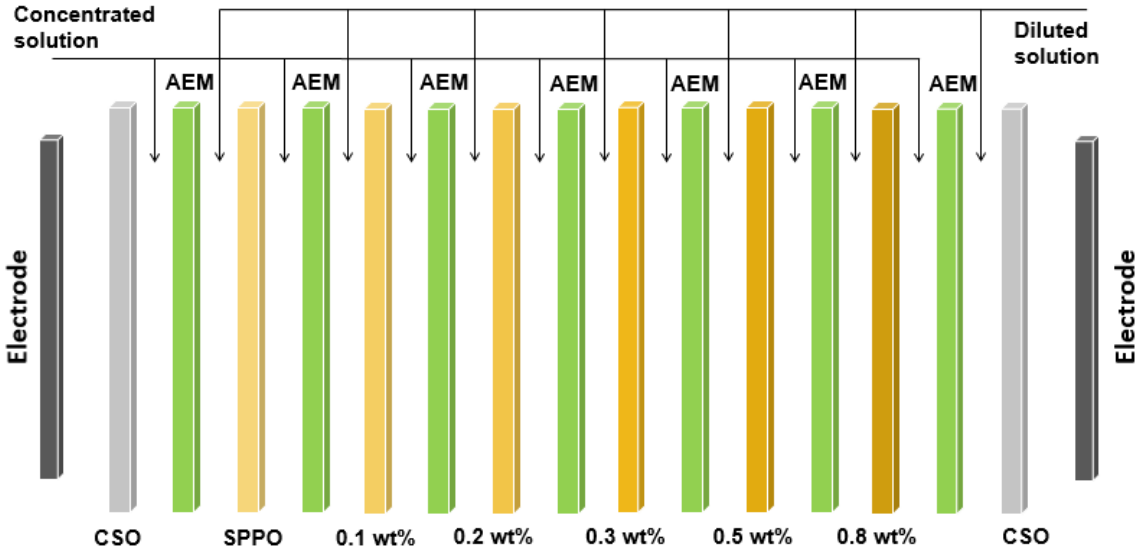

Figure 4 - Scheme of reverse electrodialysis stack (number of cells may vary).

3.3.5. RED membrane performance

The RED power generation performance of the nanocomposite CEMs was investigated by using the same RED stack described in 3.3.4. (Figure 4). Four and a half cell pairs were installed in the stack; each consists of an AEM (Fumasep FAS) (Fumatech, Germany) and a CEM (Fumasep FKS) (Fumatech, Germany). A fifth FKS was placed to prevent the negatively charged species from entering the stack. Two titanium mesh end electrodes (coated with iridium plasma) were used as cathode and anode, respectively. The FKS membranes were later replaced by the synthesized nanocomposite CEMs for comparison. All the membranes have an effective area of 9 cm × 4 cm. The intermembrane distance (cell width) was maintained by the same spacer, as described in Section 3.3.4. A solution consisting of NaCl (0.25 M), $K_4Fe(CN)_6$ (0.05 M) and $K_3Fe(CN)_6$ (0.05 M) was used as the electrode rinse solution. Model concentrated water (0.5 M of NaCl) and diluted water (0.017 M of NaCl) were prepared as feed solutions.

Membrane performance was evaluated by using an Ivium potentiostat/galvanostat analyzer (Ivium Technologies, The Netherlands) in the galvanostatic mode. The total water inflow rate was maintained at 0.38 L/ min (for both concentrated and diluted water), and the change of voltage (E) and current (I) with time was monitored. The gross power generation was calculated by the maximum value of the product of voltage and current in the measured voltage (E)-current (I) curve. The corrected gross power generation was calculated by subtracting the power generation by the blank run, which was obtained by setting only one CEM in the stack. The gross power density was then calculated by dividing the corrected gross power generation by the total membrane effective area.

3.4. Results and discussion

3.4.1. FTIR, SEM, AFM, contact angle and surface charge density

FTIR spectra were obtained from membrane material as well as synthesized nanocomposite membranes. Figure 5 presents the spectra of PPO material, SPPO membrane, and SPPO-0.5 O-MWCNT membrane. SPPO and SPPO-0.5 O-MWCNT showed obvious peaks at 1060–1030 cm^{-1} and 650 cm^{-1}, corresponding to the strong absorption of the sulfonic acid group, implying the successful sulfonation of PPO. It seems that there was no detectable difference in the intensity of absorption bands between SPPO and SPPO-0.5 O-MWCNT, which might be because the new bonds formed by the incorporation of O-MWCNTs could not be identified. The SEM and AFM images, along with the change of membrane electrochemical properties would confirm the successful incorporation of O-MWCNTs into the membranes.

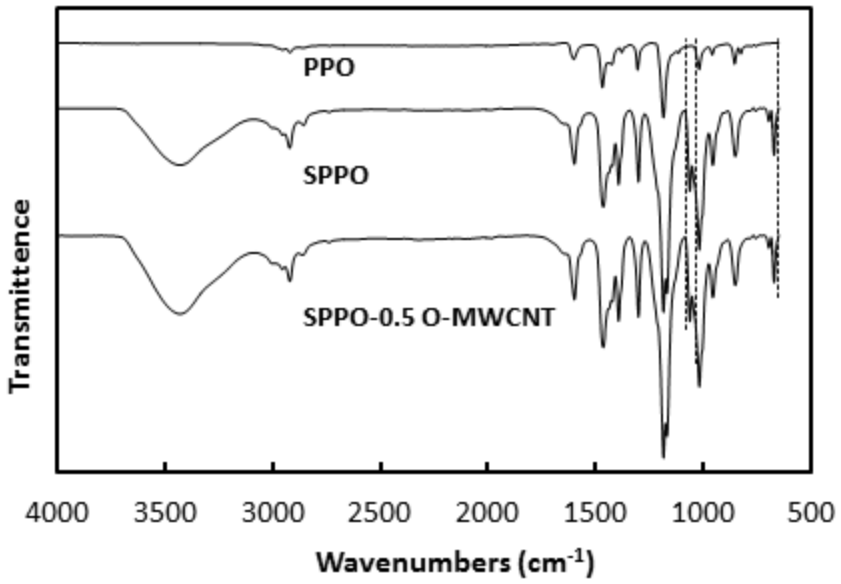

Figure 5 - FTIR spectra of PPO, SPPO and SPPO-0.5 O-MWCNT membranes.

SEM images of O-MWCNTs and chosen nanocomposite CEM surfaces are shown in Figure 6. The incorporation of inorganic fillers made the change of membrane surface morphology possible. The membrane surface became rougher with the increase of O-MWCNT loadings (Figure 6b-c). Higher magnification membrane surface SEM images (Figure 6d-f) reveals the information of membrane surface in sub-micro scale. Pristine SPPO membrane had a smooth surface; with the incorporation of O-MWCNTs, membrane surface became rougher. 1.5 wt % O-MWCNT membrane (Figure 6f) even showed a ravined surface morphology. It has been reported that membranes with rougher surfaces are easier to trap ions, and thus have lower ion rejection [62]. Figure 7 shows the SEM

images of membrane cross sections. All the SEM images show that membranes have dense inner structures without identified pore formation. The thickness of membranes was not the same but ranged from 47 to 70 µm, which might be due to a change occurring in the polymer blends' physical properties when O-MWCNTs were added.

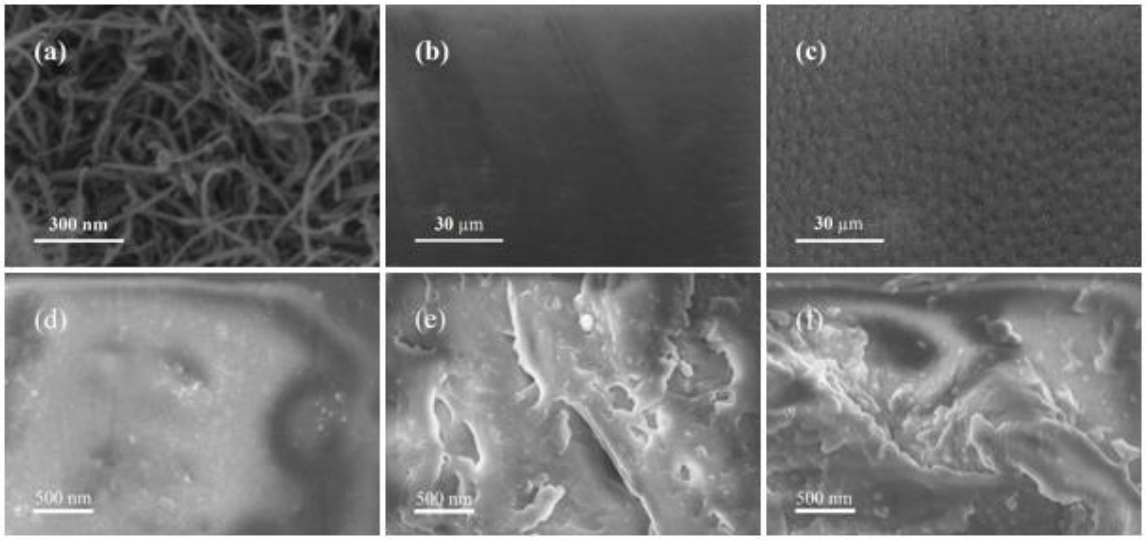

Figure 6 - SEM images of O-MWCNTs and nanocomposite cation exchange membranes: (a) oxidized multi-walled carbon nanotubes; (b) surface morphology of pristine SPPO membrane; and (c) surface morphology of composite 0.5 wt % O-MWCNT membrane; (d) surface morphology of pristine SPPO membrane (higher magnification); (e) surface morphology of composite 0.5 wt % O-MWCNT membrane (higher magnification); and (f) surface morphology of composite 1.5 wt % O-MWCNT membrane (higher magnification).

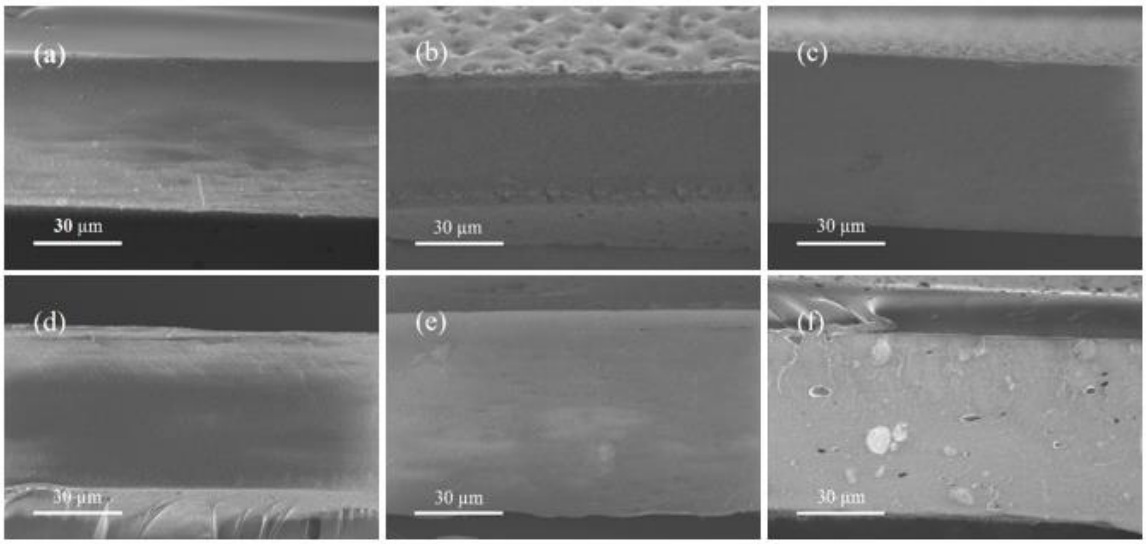

Figure 7 - Cross section of nanocomposite membranes: (a) pristine SPPO membrane; (b) composite 0.1 wt % O-MWCNT membrane; (c) composite 0.2 wt % O-MWCNT membrane; (d) composite 0.3 wt % O-MWCNT membrane; (e) composite 0.5 wt % O-MWCNT membrane; (f) composite 0.8 wt % O-MWCNT membrane.

The complementary information on the membrane surface morphology was obtained through AFM images (Figure 30). Membrane surface mean roughness (S_a) parameters are listed in Table 2 [52]. More surface roughness parameters are presented in Appendix A (Table 8). The AFM images and parameters indicate that the surface morphology continues to change as the O-MWCNT loadings increase. Table 2 also lists the water contact angles and measured surface charge densities of synthesized nanocomposite CEMs (0–0.8 wt % O-MWCNT membranes were characterized). The contact angle decreased as the loading increased and reached the optimal value at a loading

of 0.5 wt %; then, underwent a sharp increase for the 0.8 wt% O-MWCNT membrane; the measured surface charge density increased with the increase of loading up to 0.5 wt% of loading, then decreased as loading continued to increase.

Obviously, the adding of O-MWCNTs effectively changed the surface roughness, surface hydrophilicity and surface charge density of membranes. During the membrane phase inversion process, the O-MWCNTs migrate spontaneously to the membrane surface [52, 53], which changes the surface morphology and roughness of the membranes. The formation of ravined structures on the membrane surface was probably due to the migration of O-MWCNTs onto the membrane surface. As the inorganic loading increases, more O-MWCNTs migrate to the membrane surface, and surface roughness increases. Also, when the O-MWCNT loading is high (0.8 wt % or higher), the electrostatic interactions and steric hindrance among O-MWCNTs cause aggregation of O-MWCNTs during phase inversion [52]. When large O-MWCNT clusters migrate onto the membrane surface, surface roughness further increases due to the formation of larger peaks and valleys. Since there are negatively charged carboxyl groups on the surface of O-MWCNTs, membrane hydrophilicity and surface charge density increase. However, with a loading of 0.8 wt %, both membrane surface hydrophilicity and surface charge density decrease. The above phenomenon could be explained by the aggregation of O-MWCNTs reducing the density of hydrophilic functional groups on the membrane surface. The sharp increase of contact angle in the SPPO-0.8 wt % O-MWCNT membrane was probably due to the remarkable decrease of surface functional group density caused by the aggregation of O-MWCNTs.

Table 2 - Water contact angle, surface mean roughness and surface charge density of nanocomposite CEMs.

Membranes	Contact angle [°]	S_a [nm]	Surface charge density [meq /m^2]
SPPO	81.5	3.5	2.6
SPPO-0.1 O-MWCNT	75.9	7.0	2.9
SPPO-0.2 O-MWCNT	67.1	10.0	3.0
SPPO-0.3 O-MWCNT	64.1	14.6	3.0
SPPO-0.5 O-MWCNT	50.8	26.5	3.1
SPPO-0.8 O-MWCNT	73.9	36.7	2.8

3.4.2. Electrochemical properties of membranes

Ion exchange capacity (IEC), swelling degree (SD), fixed-charge degree (CD), permselectivity and ionic resistance of all the synthesized CEMs were evaluated and are listed in Appendix A (Table 9). All the measurements were carried out at least three times, and the average values were reported. To avoid confusion, standard deviations were not included in the table. Thicknesses of the membranes were measured by using FE-SEM and listed in Table 9. The properties of CSO and FKS were also evaluated and listed for comparison. Properties of 1.5 wt % O-MWCNT membrane were not shown in Figure 8–10, since the membrane properties started to decrease from loading of 0.8 wt %.

The ion exchange capacity (IEC) of membranes increased with the increase of O-MWCNT loading up to 0.5 wt % and then decreased as the loading continued to increase (Figure 8). The increase of IEC might be due to the reconstruction of the membrane micro and nanoscale structure, which increased the number of ion exchangeable functional

groups for titration [63]. The decrease of IEC, which was observed in the 0.8 wt % O-MWCNT membrane, might be due to the aggregation of the O-MWCNTs inside the membrane matrices. The aggregation of O-MWCNTs could decrease the membrane IEC by disrupting the ion exchange functional groups. Specifically, when the inorganic fillers aggregate, the density of effective functional groups reduces, and thus, the IEC decreases [35].

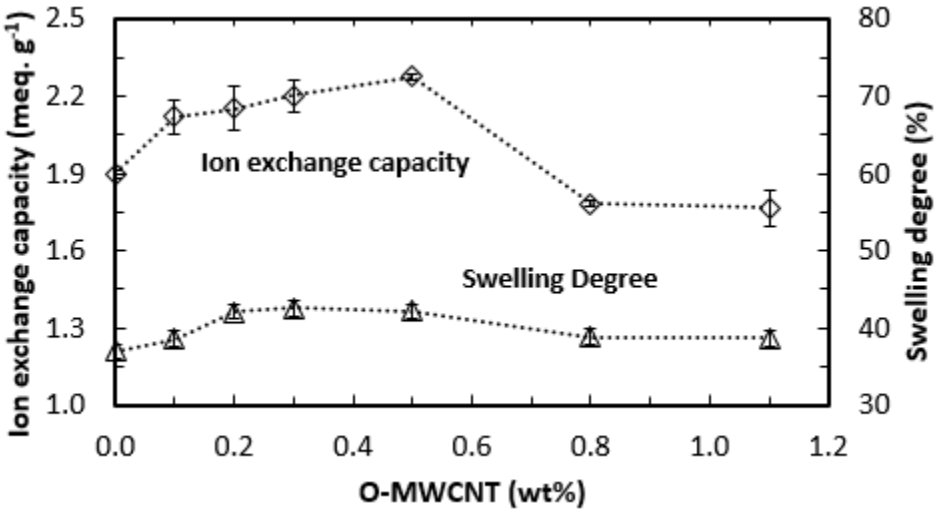

Figure 8 - Ion exchange capacity (IEC) and swelling degree (SD) of SPPO nanocomposite membranes as a function of O-MWCNT loading.

Swelling degree (SD) is a key parameter that affects fixed charge density, ionic resistance, permselectivity and mechanical properties. Generally, SD increases as the membrane IEC increases and as the cross-linking degree decreases. However, other factors, such as ion exchange functional group species and types of polymer materials, may cause fluctuation of SD [35, 64]. Figure 8 shows the increase of SD with the increase of CNT loading. However, a further increase of O-MWCNT loading (> 0.3 wt %) resulted in a decrease of membrane SD. The increase of SD up to 0.3 wt % loading is attributed to the enhancement of water absorption of membranes by the increase of IEC. In addition, the embedding of water molecules inside O-MWCNTs increased the water content [65]. The inner diameter of O-MWCNTs is large enough to accommodate water molecules [65, 66]. As the O-MWCNT loading continues to increase, the O-MWCNTs tend to aggregate (≥ 0.5 wt %), and the number of effective functional groups in the membrane reduces; thus, SD decreases. In general, the cross-linking reactions lead to a decrease of membrane SD [67]. Because it is possible for the O-MWCNTs to cross-link with the sulfonate groups in the SPPO matrices [64], the SD of nanocomposite membranes is expected to decrease. At low O-MWCNT loadings, the cross-linking effect had a negligible influence on the membrane SD. However, as the loading increased, more cross-linking reactions happened, which also may lead to a decrease of SD at higher loading. The cross-linking reaction effect might explain why the 0.5 wt % nanocomposite CEM has the highest IEC, but its SD was slightly lower than the 0.3 wt % nanocomposite CEM.

Figure 9 shows the O-MWCNT loading variation on the permselectivity and ionic resistance of nanocomposite CEMs. Permselectivity of synthesized CEMs increased with the increase of O-MWCNT loading, achieved an optimal value at 0.5 wt %, and then

exhibited a decrease. 0.5 wt % O-MWCNT SPPO membrane was the one with the highest permselectivity, probably because it simultaneously had the highest IEC and high CD. The ionic resistance of membranes decreased with the increase of O-MWCNT loading up to 0.5 wt %; however, the membrane ionic resistance abruptly increased with the further addition of nanomaterials. As the IEC increased, more functional groups were presented in the membrane matrices acting as ion exchange sites, which facilitated the ion transport; thus, the ionic resistance decreased [63]. Also, the addition of a proper amount of O-MWCNTs (≤ 0.5 wt % in this case) favors the formation of continuous inner networks or connected ionic channels inside the nanocomposite CEM matrices [68], which made it easier for ion transport. However, further addition of nanomaterials might block the ionic channels, leading to a deterioration of the membrane inner structures. In addition, the excess amount of O-MWCNTs inside the membrane led to the aggregation of nanomaterials, which decreased the number of effective ion exchange sites, as discussed above. Both effects caused the increase of ionic resistance at higher loadings. Generally, membranes with a higher fixed charge density show higher permselectivity and lower ionic resistance [39, 69]. The 0.1 wt % O-MWCNT SPPO membrane had the highest CD; however, it did not show the highest permselectivity or lowest ionic resistance. This might be attributed to the further improvement of membrane micro and nanoscale structure when higher O-MWCNT loadings were applied.

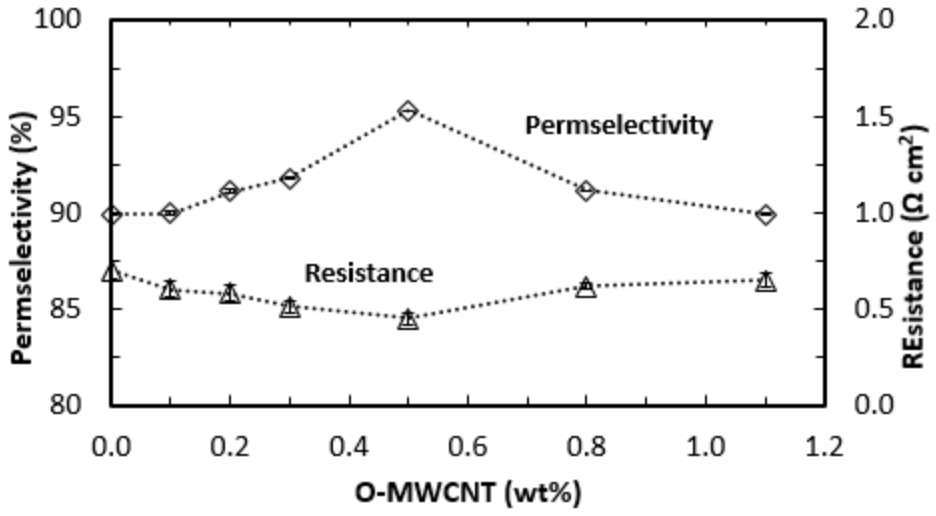

Figure 9 - Permselectivity and ionic resistance of SPPO nanocomposite membranes as a function of O-MWCNT loading.

Previous studies indicated that membrane properties such as permselectivity, SD, IEC, and CD do not differ between IEMs with different thicknesses as long as the membranes have the same chemical composition [37, 39]. However, membrane ionic resistance is a parameter that is highly related to membrane thickness, i.e., reduction of the IEM thickness results in the decrease of ionic (area) resistance [39, 70]. Intrinsic ionic resistance was introduced to exclude the membrane thickness effect and directly compare the intrinsic membrane properties with different thicknesses. Intrinsic ionic resistance is a membrane intrinsic property that is obtained by dividing the ionic resistance by the membrane thickness [70]. The change of membrane intrinsic resistance with O-MWCNT loading is shown in Figure 10. The intrinsic resistance decreased with the increase of O-

MWCNT loading up to 0.5 wt %. An increase of intrinsic resistance for 0.8 wt % O-MWCNT membrane might have been caused by the combined effect of nanomaterial aggregation and deterioration of membrane structures. As indicated in previous studies [37, 39], permselectivity does not depend on membrane thickness. In this study, when the membrane permselectivity increased, and intrinsic resistance decreased, the membranes became more effective in both the transportation of counter-ions and exclusion of co-ions. The 0.5 wt % O-MWCNT nanocomposite membrane had the most improved inner structure due to the increase of effective ion exchange sites and the formation of continuous and interconnected ionic channels, which facilitate ion transport. Consequently, the 0.5 wt % O-MWCNT was superior overall in membrane properties.

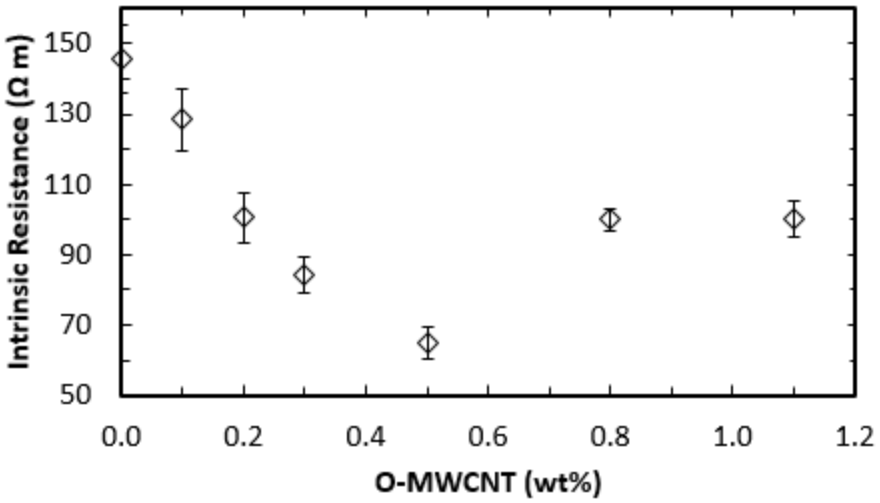

Figure 10 - Intrinsic ionic resistance of SPPO nanocomposite membranes as a function of O-MWCNT loading.

3.4.3. Anti-fouling property of membranes

The anti-fouling property of chosen synthesized CEMs was tested by using the RED stack, as described above (1.1 wt % and 1.5 wt % O-MWCNTs membranes were not included in the tests, because those two membranes showed obvious property decreases; 0.8 wt % O-MWCNT membrane was included). The current changes in the two tests are shown in Figure 11. Current in Test 1 dropped from 100 mA to 28 mA gradually during the 2 hours of operation; whereas current in Test 2 did not change obviously, and the value kept between 97.28 mA and 99 mA. Therefore, the total resistance increased in Test 1 but remained the same in Test 2.

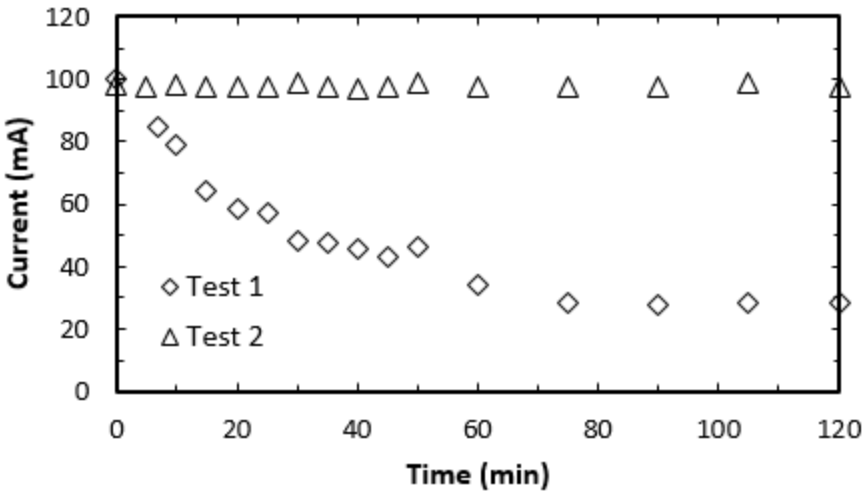

Figure 11 - Current change with time for Test 1 and Test 2.

To determine whether the properties of CEMs in Test 1 changed or not, the permselectivity and ionic resistance of all the CEMs in Test 1 were characterized. The AEMs might have also been influenced by inorganic fouling during the tests, but only the properties of CEMs were characterized. Figure 12 shows the changes of permselectivity and ionic resistance of all the CEMs, presented in the form of tested and unused ratios. The permselectivity ratios were distributed in the range between 83% and 93%. The ratio increased with the O-MWCNT loading up to 0.3 wt % and then decreased. The 0.3 wt % O-MWCNT membrane showed the highest ratio of 93%. In comparison, the CSO commercial membrane obtained a ratio of only 83%, which was the lowest among all the tested CEMs. Regarding the change of ionic resistance, the ratios ranged from 117% to

149% for all the CEMs. The CSO CEM had the lowest ratio of 117%, and the 0.3 wt % O-MWCNT membrane maintained a value of 138%, which was the lowest among all the synthesized nanocomposite CEMs. The 0.3 wt % O-MWCNT membrane had the best anti-fouling property among all the tested nanocomposite CEMs because both the permselectivity and the ionic resistance changed the least. When compared with commercial CSO, the 0.3 wt % O-MWCNT membrane showed a smaller decrease in permselectivity, and a larger increase in ionic resistance. To further evaluate the properties of CEMs before and after the anti-fouling test, and better assess membrane anti-fouling performance, membrane performance potential (α^2/R) [35] was applied. According to the Nernst equation, permselectivity largely influences the voltage (open circuit voltage, OCV) of the RED system; the ionic resistance of membranes affects the total resistance of RED stack, and thus influences the RED power generation [69, 71, 72]. Permselectivity and ionic resistance together influence the overall performance of the RED system. Since the membrane performance potential (α^2/R) could be used to compare the power generation of different CEMs (Appendix A), it was applied here to represent the overall membrane performance in RED system (the larger the potential of the CEM, the better it performs in a RED system; the less potential drop after the anti-fouling test, the better the CEM can resist the fouling). Table 3 lists the membrane potentials of all CEMs both before and after the test as well as the membrane potential changes.

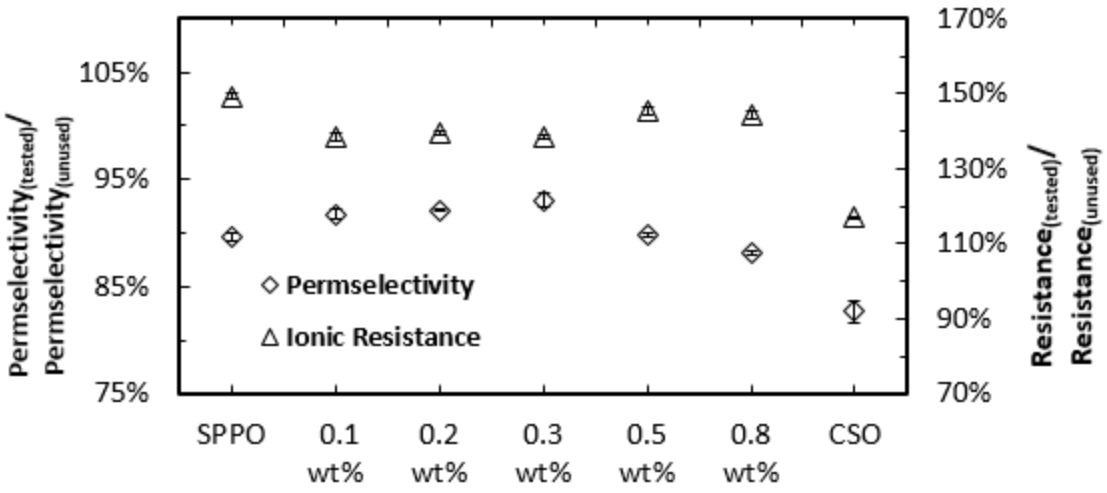

Figure 12 - Ratio of permselectivity and ionic resistance of CEMs after anti-fouling Test 2.

Table 3 - Potentials (α^2/ R) of CEMs before and after the anti-fouling test (Test 1) (The FKS membrane was not included in the anti-fouling test, and only the original potential is listed).

Membranes	Potential Before Test	Potential After Test	Percentage (used/ unused)
SPPO	11367	6125	53.9%
SPPO-0.1 O-MWCNT	13425	8167	60.8%
SPPO-0.2 O-MWCNT	14227	8658	60.9%
SPPO-0.3 O-MWCNT	16416	10274	62.6%
SPPO-0.5 O-MWCNT	20034	11107	55.4%
SPPO-0.8 O-MWCNT	13415	7217	53.8%
CSO	3968	2319	58.4%
FKS	5280	--	--

From Table 3, the 0.3 wt % O-MWCNT membrane had the least potential drop among all CEMs; the commercial CSO membrane maintained 58.4% of the potential after the test, which was lower than the 0.1 wt %, 0.2 wt %, and 0.3 wt % O-MWCNT membranes, but higher than the pristine membrane, 0.5 wt % and 0.8 wt % O-MWCNT membranes. However, 0.5 wt % O-MWCNT membrane had the highest potential both before and after testing. As a result, 0.3 wt % O-MWCNT membrane had the best anti-fouling performance, which maintained 62.6% of the potential after testing; 0.5 wt % O-MWCNT membrane maintained the highest absolute value of membrane potential after the anti-fouling test.

Generally, membranes with lower surface roughness, higher surface charge density, and larger surface hydrophilicity have better antifouling properties [52]. Regarding AEMs coating, a thin negatively charged layer can effectively enhance the anti-fouling performance, since organic fouling is dominated in AEMs and most organic foulants are negatively charged [27]. However, it is more complicated for CEMs. In a natural environment, negatively charged species, like hydroxide or carbonate species, adsorb onto CEMs surface. When divalent cations like Ca^{2+} or Mg^{2+} transport through the membranes, they react with negatively charged species to form insoluble scaling and sorb on the surface or inside membranes. It is obvious that the methods for AEMs are not applicable to CEMs since applying a positively charged coating layer onto CEMs would only make the fouling problem worse. In this study, nanocomposite CEMs were found to be effective for reducing fouling problem, because both negatively charged surface density and hydrophilicity increased simultaneously by incorporating functionalized inorganic fillers. Increasing surface charge density results in the increase of electrostatic repulsion between the

membrane surface and negatively charged species, which reduces the chance for anion adsorption. Increasing membrane hydrophilicity also enhances membrane anti-fouling properties because most of the foulants are hydrophobic. However, there is a trade-off between surface charge density and surface roughness in nanocomposites; both parameters change because of the migration of nanomaterials onto the membrane surface. As surface charge density increases, surface roughness also increases. Rougher surfaces are more prone to ion and molecule adsorption and attachment. Optimal loading exists in nanocomposite membranes. In this study, the optimal loading is between 0.3 wt % and 0.5 wt %.

3.4.4. Performance of membranes in RED

Power generation of all the synthesized nanocomposite CEMs (except for 1.1 wt % and 1.5 wt % O-MWCNT nanocomposite membranes), as well as commercial FKS membranes, were tested in a RED stack by using FAS membranes as the AEMs. The complete results are shown in Appendix A.6. At least three measurements were conducted for each CEM, and the average values were reported. Power generation of CSO membranes was also tested but not listed, since the gross power density of CSO was lower than that of FKS membranes. The changes in membrane RED performance were consistent with the changes in electrochemical properties discussed in Section 3.2: Gross power density increased with the increase of O-MWCNT loadings; 0.5 wt % O-MWCNT membrane had the best overall electrochemical properties and gained the highest gross power density (0.48 W/m^2) among all the membranes; the 0.8 wt % O-MWCNT membrane showed a decrease in gross power density. The gross power density of supreme commercial FKS CEM was 0.42 W/m^2. It should be noticed that the power output of the RED system is influenced by

other factors besides membrane properties. Factors that could influence the system power density include the number of cells [22], composition and concentration of feed waters [23, 24, 71, 73], flow rate [35, 38], temperature [71], and the thickness of spacers [72]. In the literature, different gross power densities were obtained and even the same IEMs were used [26, 71], so it is difficult to compare different RED systems when the same IEMs are used. However, when keeping other factors the same (including AEMs), by changing only the CEMs, power generation properties of different CEMs can be obtained and compared. In this study, the gross power density of 0.5 wt % O-MWCNT membranes was about 14% higher than the commercial FKS membranes, which shows that 0.5 wt % O-MWCNT membranes perform better than FKS membranes in terms of power generation.

Membrane power generation could also be related to the membrane potential (α^2/R) (Table 3). Generally, membranes with higher potential also show better power generation properties, which is consistent with the theoretical prediction (Appendix A.5). The 0.8 wt % O-MWCNT was the only exception, which might be because the O-MWCNT agglomeration influenced the membrane micro and nanoscale structure and made the membrane performance more difficult to predict. The FKS membrane had the lowest membrane potential, but the power generation property was better than half of the tested nanocomposite CEMs. This might be explained by the fact that membrane material and membrane structure highly influence membrane power generation. Membranes of different materials perform quite differently in a RED system, and the performance cannot be simply predicted according to membrane intrinsic properties. Also, since it is difficult to compare the structures of nanocomposite CEMs and FKS directly, how the micro and nanoscale structure influence the properties and power generation remains unknown. Further research

is necessary for studying the correlation among membrane micro and nanoscale structures, membrane materials and the membrane properties.

3.5. Conclusion

In this study, oxidized multi-walled carbon nanotube (O-MWCNT) nanocomposite CEMs were synthesized with different O-MWCNT loadings. The properties of all the synthesized membranes were characterized. The 0.5 wt % O-MWCNT CEM performed the best in terms of membrane IEC, CD, permselectivity, and resistance. The property deterioration started at 0.8 wt % O-MWCNT CEM, which might be due to the aggregation of inorganic fillers. The SD of the 0.3 wt % O-MWCNT CEM was larger than that of the 0.5 wt % O-MWCNT CEM, which might be explained by the cross-linking of inorganic fillers with the functional groups of the polymer. Anti-fouling tests showed that the nanocomposite CEMs had better fouling resistant properties than the commercial CSO membrane. The 0.3 wt % O-MWCNT CEM had the least membrane potential (α^2/R) drop after testing; the 0.5 wt % O-MWCNT CEM maintained the highest absolute value of membrane potential. By incorporating O-MWCNTs, both membrane surface hydrophilicity and surface charge density increased. The enhancement of these surface properties might explain the enhancement of membrane anti-fouling properties. For energy generation in the RED system, the CEM was optimized at 0.5 wt % of O-MWCNT, which had a power output that was about 14% higher than the commercial FKS membrane. Nanocomposite membranes were found to be attractive candidates for application in electrochemical systems like RED. By incorporating nanomaterials into polymer membranes, anti-fouling properties and energy generation in RED could be improved simultaneously. As diverse nanomaterials and more innovative synthesizing methods are

developed, the nanocomposite membranes are expected to play more important roles in enhancing the performance of systems like RED and further diminish the membrane fouling problem.

CHAPTER 4. MECHANISM EXPLORATION OF ION TRANSPORT IN NANOCOMPOSITE CATION EXCHANGE MEMBRANES

4.1. Abstract

The origin of property enhancement of nanocomposite ion exchange membranes (IEMs) is far from being fully understood. By combining experimental work and computational modeling analysis, we could determine the influence of nanomaterials on the ion transport properties of nanocomposite cation exchange membranes (CEMs). We synthesized and characterized a series of nanocomposite CEMs by using SPPO as polymer materials and silica nanoparticles (NPs) (unsulfonated or sulfonated) as nanomaterials. We found that with the increase of NP loading, measured CEM permselectivity and swelling degree first increased and then decreased. We also found the ion exchange capacity (IEC) and ionic resistance of nanocomposite CEMs tend to be the same, regardless of what type of NPs are incorporated into the membrane. Modeling analysis suggests that the change of membrane properties is related to the change in membrane micro-structure. With the addition of silica NPs, membrane porosity (volume fraction of inter gel phase) increases, so that membranes can absorb more water. Also, the volume fraction of sulfonated polymer segments increases, which can allow membranes to retain more counter-ions, causing membrane IEC to increase. By calculating the effective ion diffusion coefficients and membrane tortuosity factors of all the silica-NP-based CEMs synthesized in this study, along with nanocomposite CEMs from previous studies, we conclude that membrane ion transport efficiency tends to increase with the incorporation of nanomaterials. In addition,

this paper presents a simulation model, which explains how the membrane property changes upon nanomaterial aggregation; the simulation results are in good agreement with the experimental data. Simulation results indicate that membrane properties are related to nanomaterial number concentration in the membrane matrices; thus, a plateau is reached for membrane ion diffusion coefficients due to the severe influence of aggregation on the increase of nanomaterial real number concentration. The results of this study can provide insight into membrane structure-property relation and contribute to the value of future designs of new nanocomposite IEMs.

4.2. Introduction

Ion exchange membranes (IEMs) have been extensively used in electrochemical systems to produce clean water and renewable energy [12, 44, 74, 75]. Electrochemical systems that traditionally utilize IEMs include fuel cells (FCs) [76, 77], electrodialysis (ED) [78-80], reverse electrodialysis (RED) [15, 69, 81] , redox flow batteries (RFBs) [82, 83], and microbial fuel cells (MFCs) [84, 85]. As key components, IEMs largely influence the effectiveness and efficiency of those systems. Plenty of research has been conducted to optimize electrochemical system performance, but little research has focused on the desired properties IEMs and the important roles they can play in optimizing those systems. IEMs are ion containing polymer electrolytes, which can be classified as part of both cation exchange membranes (CEMs) and anion exchange membranes (AEMs). CEMs contain negatively charged functional groups, which allow the transport of cations but repel anions. Meanwhile, AEMs contain positively charged functional groups and have the inverse ability regrading ion permeation.

In order to get IEMs with the desired performance, the nanoscale design of ion exchange channels has been extensively studied in recent years [86]. A nanocomposite IEM is one type of nanostructured membrane, which incorporates inorganic nanomaterials into polymer materials [41, 43, 45, 86-88]. It has been reported that many nanocomposite IEMs have enhanced physicochemical and electrochemical properties compared to their pristine counterparts [35, 68, 89-93]. On the one hand, nanocomposite IEMs have superior overall electrochemical properties compared to the pristine polymeric membranes; on the other hand, they are also excellent candidates for solving problems in specific electrochemical systems. For instance, methanol crossover can be significantly reduced in direct methanol fuel cells (DMFCs) by applying nanocomposite IEMs [94, 95]; nanocomposite IEMs can also effectively prevent the cross-mixing of electrolytes while maintaining high ion conductivity in vanadium redox flow batteries (VRFBs) [83, 96]. Regarding the synthesis of nanocomposite CEMs, different synthesizing methods have been developed, among which the physical blending method and sol-gel method are most commonly used [88]. The physical blending is a method wherein the nanomaterials are prepared prior to the membrane synthesis, and then mixed with the polymer material; however, for the sol-gel method, filler precursors are first dispersed into the polymer solution, and then functionalized nanomaterial fillers are synthesized during the membrane fabrication process [87, 88].

Different hypotheses have been proposed to explain the origin of the property enhancement for nanocomposite IEMs. Many researchers think that the functionalized nanomaterials can introduce extra ion exchange functional groups, which act as additional ion exchange sites. With more active ion exchange sites present in membrane matrices, ion

transport could be facilitated. Consequently, both the ion exchange capacity (IEC) and ionic (proton) conductivity increase, which means the ionic resistance decreases [35, 91, 97]. Other researchers claim that the nanomaterials will change the structure of the ion exchange membranes [41]; the addition of nanomaterials favors the formation of both continuous ion channel networks inside the membrane matrices and the interconnection of channels inside nanocomposite membranes [68]. Ion channels could also be formed at the interfaces of nanomaterials and polymer materials as a result of the interaction of those two [86]. The second hypothesis was tested by detecting membrane structures at the nanoscale level using electron microscopy techniques [51, 98]. Many unanswered (or only partially answered) questions remain, which prevent more detailed understanding of ion transport in nanocomposite CEMs. Our hypotheses are that the interactions among nanomaterials and polymers change the membrane micro scale structure upon the addition of nanomaterials; thus, the transport of ions could potentially be influenced by the membrane structure change.

Although it is widely recognized that membrane properties would be affected by the chosen materials as well as the selected fabrication method, we have found that a certain mechanism is followed regarding membrane property change when nanomaterials are added. A physical blending method was chosen to ensure the nanoparticle (NP) properties remain unchanged during the whole membrane fabrication process. Also, the physical blending method allowed analysis of the NPs before mixing with the polymer solution. The physicochemical and electrochemical properties of the nanocomposite membranes were extensively characterized, and comparisons were made noting differences between membranes containing unsulfonated and sulfonated silica NPs. The influence of NP

loadings and additional functional groups introduced by NPs on the properties (IEC, permselectivity, swelling degree, and ionic resistance) of the CEMs was comprehensively investigated. In addition, the numerical model analysis was conducted to quantify the membrane structure change and the influence on ion transport. The origin of membrane property enhancement was discussed and related to the change in membrane structure. Furthermore, a numerical simulation was used to quantify the influence of nanomaterial aggregation on the real number concentration of nanomaterial in the membrane matrices. The tendency of membrane ion transport efficiency to change after nanomaterial aggregation was also discussed.

4.3. Experimental Section

4.3.1. Materials

Poly (2, 6-dimethyl-1, 4-phenyleneoxide) (PPO) (Aldrich, Mw 30000, Mn 20000) was used as the polymer material. Chloroform (Aldrich, anhydrous, 99%) was chosen for dissolving PPO. Silica (SiO_2, silicon dioxide) (US Research Nanomaterials, 99.5%) NPs with diameters of 15–20 nm were used as nanomaterial fillers. Chlorosulfuric acid (Aldrich, 98%) was applied for the sulfonation reactions. Tin(II) chloride ($SnCl_2$, 98%) was used as a catalyst for the sulfonation of silica NPs. Glycidyl phenyl ether (GPE) and dimethyl sulfoxide (DMSO) (ACS grade, 99.9%) were obtained from Sigma-Aldrich and VWR, respectively.

4.3.2. Sulfonation of silica NPs and PPO

The sulfonation of silica NPs was conducted using a previously reported method [99]. Silica NPs and GPE were mixed and then stirred at 140 °C for 3 hours with the presence of $SnCl_2$ as a catalyst. The solvent was then evaporated, and the remaining mixture was centrifuged to obtain the condensed product. Then the condensed product was treated with fuming sulfuric acid for 18 hours at room temperature. The precipitate was collected after cooling and centrifuging. The collected product (sulfonated silica NPs) was then dried and kept for future characterization. A scheme of sulfonation reaction of silica NPs is shown in Appendix B (Figure 32).

PPO of 9.6 grams was dissolved into 100 mL of chloroform, and the solution was stirred for 1 hour. Further, 4.4 mL of chlorosulfonic acid dissolved in 50 mL of chloroform was slowly added into the PPO solution while stirring. The precipitate was filtered and then washed several times with deionized (DI) water, until the pH became approximately neutral. The resulting SPPO was dissolved again into methanol, and the solution was then poured into a Pyrex glass tray to form a thin 1-2 mm layer. The layer was then air dried under a fume hood at room temperature for 48 hours. At last, the dried SPPO was cut into small pieces and kept for future use.

4.3.3. Fabrication of nanocomposite membranes

Table 4 - List of materials used for synthesizing a series of nanocomposite CEMs.

Name	Feeding NP loadings (wt %)		SPPO (g)	DMSO (g)
	Unsulfonated silica	Sulfonated silica		
Membrane 1	−	−	5	20
Membrane 2a	0.2	−	5	20
Membrane 2b	−	0.2	5	20
Membrane 3a	0.5	−	5	20
Membrane 3b	−	0.5	5	20
Membrane 4a	0.8	−	5	20
Membrane 4b	−	0.8	5	20
Membrane 5a	1.0	−	5	20
Membrane 5b	−	1.0	5	20

In this study, we synthesized and characterized nanocomposite CEMs by using either unsulfonated or sulfonated silica (NPs). Sulfonated poly (2, 6-dimethyl-1, 4-phenyleneoxide) (SPPO), a well-studied sulfonic-acid-based polymer [56, 100, 101], was used as the model polymer material for the membrane fabrication. Solution casting and phase inversion methods were used for the preparation of nanocomposite CEMs. Each

batch of the polymer solution was prepared by first dispersing silica NPs into 20 grams of DMSO, then dissolving 5 grams of SPPO into the suspension. Ultrasonic bath (B3500 A-MT, 50/ 60 Hz, VWR) was applied for obtaining well dispersed NP suspension. After SPPO was added, the solution was stirred for 48 hours at room temperature. The resulting polymer solution was cast on a glass plate by using a doctor blade. Then the membrane together with glass plate was vacuumed in an oven at 50°C for 36 hours. The membrane was then peeled off from the glass plate. The peeled membrane was first soaked into 1 M of HCl solution for one day, and then stored in 0.5 M of NaCl solution for future characterization.

All the synthesized membranes are listed in Table 4. To fairly compare membranes synthesized with different (sulfonated or unsulfonated) NPs, for each membrane pair (e.g., membranes 2a and 2b), the same moles of NPs were added. However, to be experimentally operable, the molar number was converted to weight percentage (as of SPPO). The calculation of the molecular weight of different silica NPs is shown in Appendix B.2. Table 4 lists the added NPs as weight percentage.

4.3.4. Characterization of silica NPs and IEMs

Fourier transform infrared (FTIR) spectra of silica NPs and membrane samples were obtained by using an FTIR spectrometer (Digilab FTS 7000). SEM images were taken by a field emission scanning electron microscopy (FE-SEM, Hitachi SU8230). Energy dispersive X-ray spectroscopy (EDX, Hitachi SU8230) was applied to get information about cross-sectional elemental information for chosen membrane samples. Atomic force microscopy (AFM) (Agilent 5500, Agilent Technologies, Inc., US) was used to obtain the

tapping mode phase images of wet membrane (in Na^+ form) surfaces. The membrane thickness was obtained by using a micrometer, and at least three measurements were conducted for each sample. For all these tests (except for those implemented to obtain AFM phase images), the membrane samples were dried in a vacuum oven at 50 °C for 24 hours.

The IEC of NPs and membrane samples was measured by a back titration method [37, 102]. Membrane swelling degree (SD), membrane porosity, apparent permselectivity, and membrane ionic resistance were also measured. All the measurements were conducted at least three times. A detailed description of membrane properties measurement procedures is listed in the Appendix B.3.

4.3.5. Three-phase model and effective diffusion coefficient calculation

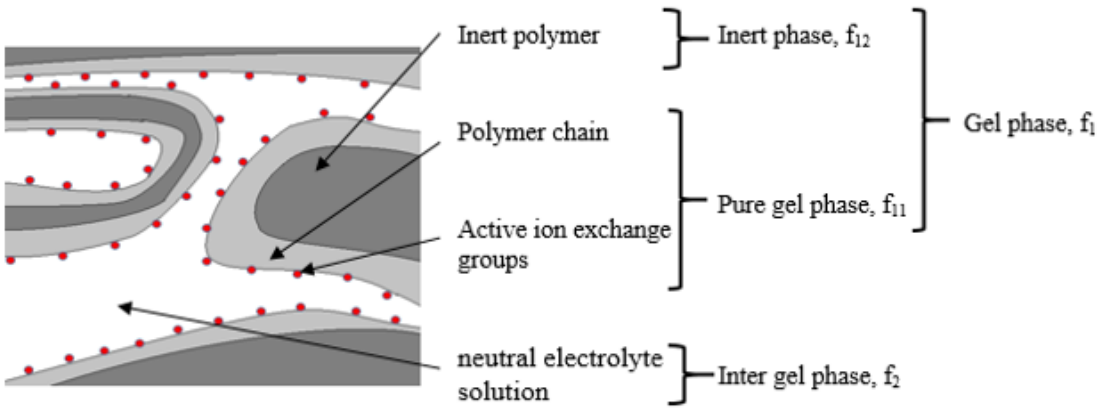

Figure 13 - Schematic illustration of micro phases of ion exchange membrane and grouping of membrane phases based on the three-phase model.

In the sulfonic acid group-containing CEMs, the sulfonated polymer segments aggregate into ionic clusters, and randomly distribute inside the bulk inert polymer matrices. Counter-ions transport through the sulfonated hydrophilic ionic clusters in hydrated membranes and co-ions are repelled. From a three-phase model point of view, a membrane can be treated as heterogeneous at the microscale [57, 103]. A total of four different membrane micro phases are considered: the inert polymer phase (non-sulfonated polymer segments), the polymer chain phase (sulfonated polymer segments), the active hydrated functional groups' phase, and the inter-gel (neutral electrolyte solution) phase [57, 104]. Also, Figure 13 shows a way of grouping different membrane phases based on the model [57]. Both the pure gel phase and neutral electrolyte solution (inter gel phase) are considered ionic conductive, but with different conductivities [57]. When dealing with nanocomposite membranes, the volume of nanomaterials is neglected, since it is extremely small compared with that of polymer materials. According to the micro-heterogeneous theory, the total membrane conductivity could be deduced as [57, 103]:

$$k_m = {k_{11}}^{f_{11}} {k_2}^{f_2} \quad (1)$$

where k_m is the membrane conductivity, f_{11} and f_2 are volume fractions of the pure gel phase and the electrolyte solution phase, respectively, and k_{11} and k_2 are conductivities of the pure gel phase and the electrolyte solution phase, respectively.

Further, to get insight into the ion transport process inside membranes, the Nernst-Einstein equation was applied to calculate the (effective) ionic diffusion coefficient by using membrane ionic conductivity data [105]:

$$D = \frac{\Lambda RT}{z^2F^2} \quad (2)$$

where D is the ionic diffusion coefficient (in solution or in the membrane), Λ is the molar conductivity, R is the ideal gas constant, T is the temperature, z is the ion charge, and F is the Faraday constant. We employed D_{eff} to represent the effective ionic diffusion coefficient in the membrane (and D the effective ionic diffusion coefficient in bulk solution). In addition, to account for how the change of volume and the arrangement of different membrane phases influence ion transport, we introduced the tortuosity factor (τ) [106]:

$$\tau = \frac{D_{eff}}{D} f_2 \quad (3)$$

where τ is a parameter that influences the transport path of ions. The value of τ should always be equal to or larger than 1, where the value 1 represents ions diffuse in bulk solution. As the value increases, ions diffuse through longer and more tortuous pathways, and ion transport efficiency decreases.

4.4. Results and Discussion

4.4.1. NP and membrane properties characterization

FTIR spectra were collected for PPO powders, different silica NPs and selected CEMs (Figure 14). All the CEMs contain absorbance with peaks 1060–1030 cm^{-1} and 650 cm^{-1}, indicating the existence of sulfonic acid groups [107]. Sulfonated silica NPs also show obvious peaks at 1060–1030 cm^{-1}, implying the successful sulfonation of NPs. Both silica NPs contain absorption peaks of alcohols at 1120–1100 cm^{-1}. The sulfonated silica NPs contain a broad absorbance with peaks between 3676 cm^{-1} and 1580 cm^{-1}, due to the

numerous functional groups (including alcohol, alkane, ether, and aromatic homocyclic groups) attached to the surface upon sulfonation reaction (Appendix B.1) [107].

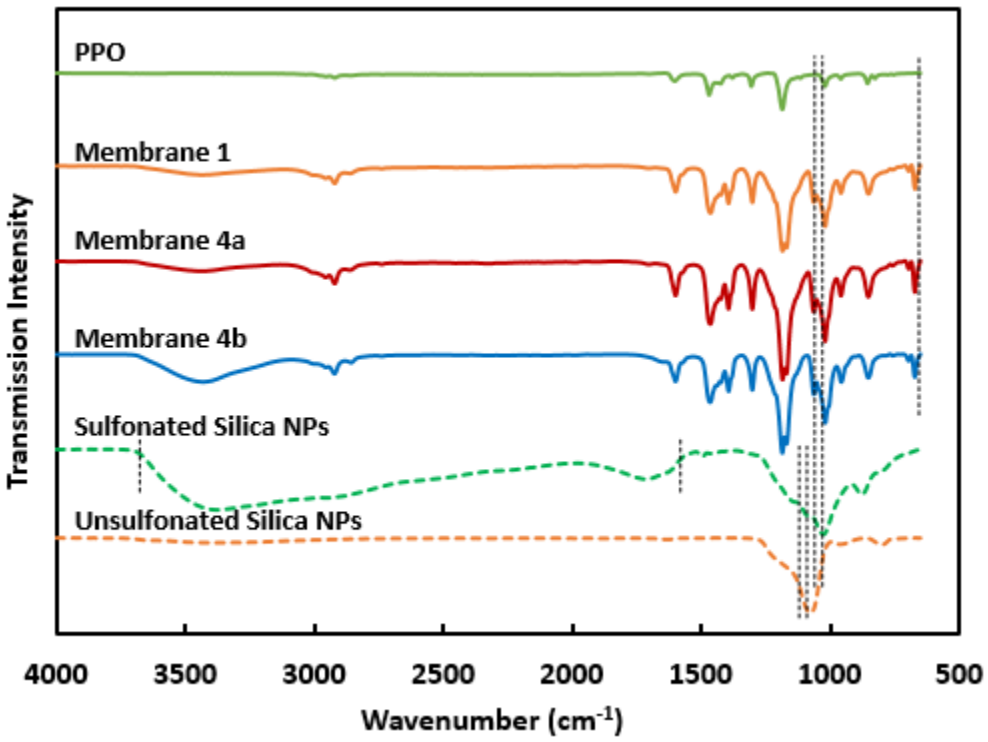

Figure 14 - FTIR transmission spectroscopy.

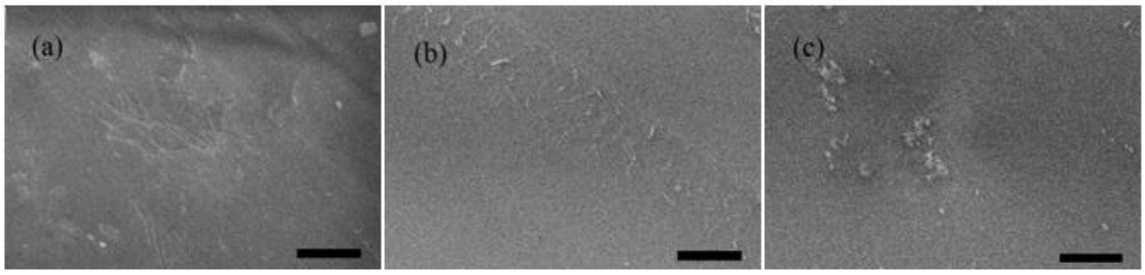

Figure 15 - Surface SEM images of (a) membrane 1, (b) membrane 3a, and (c) membrane 3b. The black scale bars at the bottom right are equal to 10 µm.

Surface SEM images of selected IEMs are shown in Figure 15. The pristine SPPO membrane (Figure 15 (a)) has a smooth surface. The surface morphologies of nanocomposite membranes (Figure 15 (b) and (c)) are quite similar with that of the pristine SPPO membranes; however, obvious nanomaterial aggregations could be identified in membranes 3a and 3b. The diameters of the largest aggregated particles exceed 1 µm. Membrane surface AFM phase images (Figure 33 and Figure 34) were also obtained. With the addition of silica NPs, both the ratio of hydrophilic domains and membrane surface mean hydrophilicity increased (Appendix B.4) [106, 108-111]. The SEM image of silica NPs and selected membrane cross-sectional EDX are shown in Appendix B.5.

The IEC of both unsulfonated and sulfonated silica NPs was measured by the titration method. As shown in Table 5, the IEC of silica NPs had a remarkable increase (from 0.11 to 0.82 meq/g) after sulfonation, which indicates the successful addition of

sulfonic acid containing functional groups onto the NP surfaces. The IEC of unsulfonated silica NPs was 0.11 meq/g, which might be caused by the adsorption of protons onto the NP surfaces. Standard derivation in Table 5 is from three different measurements. The molecular weights of different NPs are also listed in Table 5. Detailed calculation is in Appendix B.2. Different NPs have the same molecular weight, which means the sulfonic acid-containing functional groups do not influence the molecular weight of silica NPs.

Table 5 - IEC and the molecular weight of silica nanoparticles.

	IEC [meq/g dry]	Molecular Weight [g/mol]
Unfunctionalized Silica NP	0.11±0.01	60
Sulfonated Silica NP	0.82±0.03	60

Table 6 - Properties of synthesized CEMs.

Membranes	Thickness (μm)	IEC [meq /g dry]	SD [%]	Permselectivity [%]	Resistance [Ω cm^2]
Membrane 1	78±6	1.76±0.07	34.4±8.9	87.4±0.8	1.38±0.09
Membrane 2a	93±4	1.95±0.03	36.3±0.9	92.4±0.9	0.81±0.08
Membrane 2b	94±1	1.95±0.02	41.5±0.7	91.6±1.7	0.82±0.01
Membrane 3a	98±2	1.93±0.05	42.0±1.4	92.3±0.8	0.84±0.04
Membrane 3b	98±1	1.97±0.06	46.9±1.4	92.9±1.1	0.85±0.03
Membrane 4a	91±3	2.20±0.06	43.3±2.5	88.1±0.1	0.75±0.02
Membrane 4b	89±7	2.17±0.02	44.5±4.9	87.6±2.1	0.74±0.09
Membrane 5a	88±4	1.85±0.01	49.3±1.3	80.0±1.8	0.81±0.16
Membrane 5b	97±6	1.87±0.07	46.6±5.9	82.8±1.1	0.85±0.15

Membrane thickness, IEC, SD, permselectivity and ionic resistance of all synthesized membranes are listed in Table 6. All the measurements were carried out at least three times, and the average values were recorded.

Table 6 presents the IEC of all the synthesized membranes. The IEC of membranes first increases and then decreases with the incorporation of NPs. As the NP loadings increase, the IEC of membranes increases and reaches maximum values in Membranes 4a and 4b (2.20 meq /g and 2.17 meq /g, respectively); then, decreases as NP loadings continue

to increase. The IEC of nanocomposite CEMs (e.g., IECs of membrane 2a and 2b) are almost the same when they have the same NP loadings regardless of whether the NPs are functionalized or not, which indicates that the ion exchange functional groups onto the NPs do not influence the membrane IEC. Otherwise, the influence could be neglected. The SD of synthesized membranes increases with the increase of NP loading. When NPs are first added, the SD has a sharp increase; as the loading becomes relatively high (above 0.5 wt%), there is only a small increment of SD with further adding of NPs. Compared with other membrane properties, the relatively large uncertainty (standard derivation) of the measurement might explain the weaker regularity of the SD data. The incorporation of NPs also affects membrane permselectivity with an optimal loading of 0.5 wt% for both types of NPs. By incorporating NPs, membrane ionic resistance sharply decreases, as shown in Figure 16. It seems that the type of NPs has no influence on the membrane ionic resistance. Thus, membranes with the same NP loadings but with different NP types (unsulfonated or sulfonated) have similar ionic resistance. When considering the membrane intrinsic resistance (Figure 16 (C) and (D)), which is the membrane ionic resistance over membrane thickness [70, 81], membranes have the same value with the same NP loading.

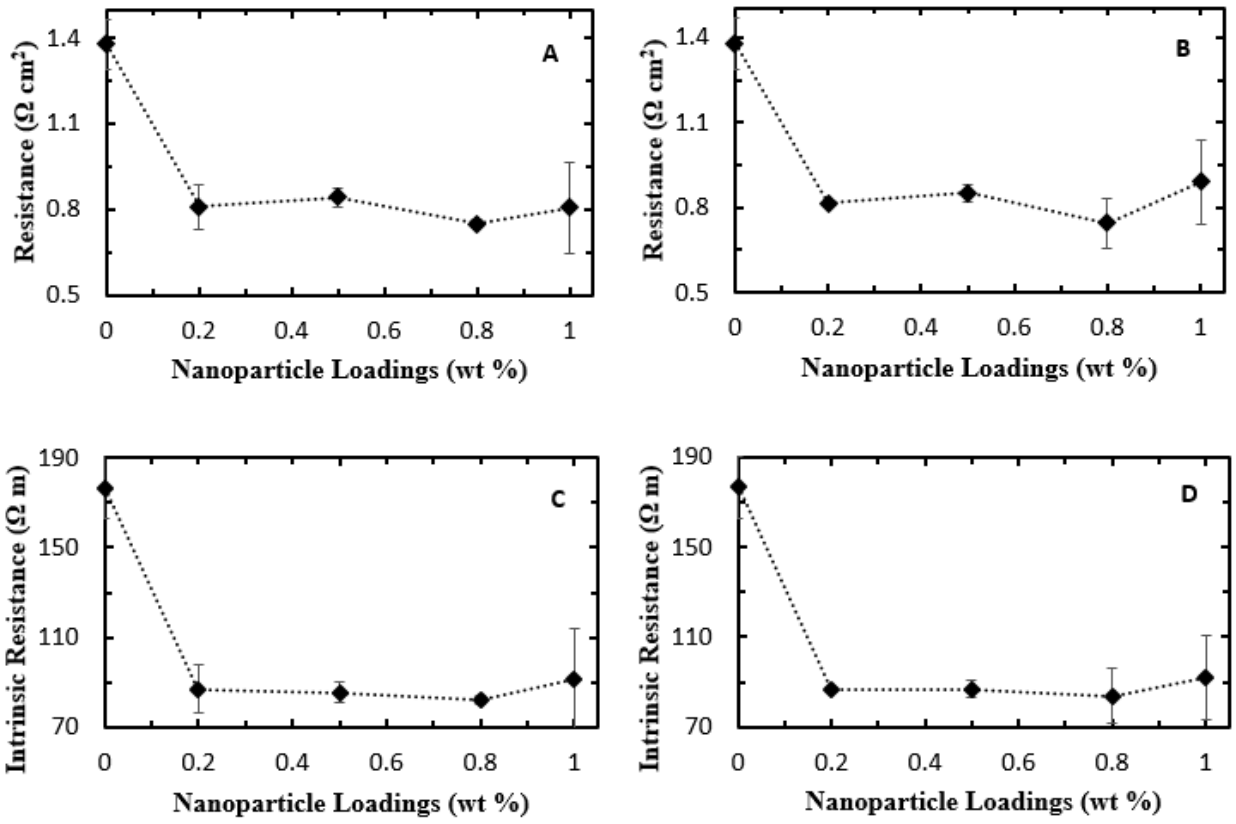

Figure 16 - Ionic resistance of nanocomposite CEMs with (A) unsulfonated silica NPs and (B) sulfonated silica NPs; The next two figures show the intrinsic resistance of nanocomposite CEMs with (C) unsulfonated silica NPs and (D) sulfonated silica NPs (error bars are +/-1 standard deviations).

Intuitively, IEC of nanocomposite CEMs equals the total ion exchange functional groups of polymer material and nanomaterial over the membrane dry weight. Accordingly, the ion exchange functional groups on the NPs might help to increase the density of total ion exchange sites (i.e., IEC) in the membrane matrices. In literature, the increase of IEC

of nanocomposite IEMs is often attributed to the introduction of ion exchange functional groups by the functionalized nanomaterials [64, 91, 97, 102, 112, 113]. To verify the above hypothesis, it was important to obtain information about the density of functional groups in nanomaterials. A few previous studies have measured the IEC of nanomaterials by using the titration method [102, 113, 114]. When the nanomaterial content (loading, wt %) in the membrane was relatively high, for example up to 10 wt %, the above hypothesis seems to well explain the trending of IEC [112, 113], because the nanomaterials introduced a large sum of functional groups. However, when the nanomaterial content is low (e.g., $\leq$ 1−2 wt %) [102, 114], the number of functional groups introduced by the nanomaterials is negligible when compared with that of the polymer materials. In this study, the membrane IEC increased by more than 20% with the incorporation of only 0.8 wt % silica NPs. Considering that the IEC is relatively low even for the sulfonated silica NPs (0.82 meq /g), it is impossible that the increase of IEC was caused by the introduction of additional functional groups. The conclusion was further confirmed when adding unsulfonated silica NPs also led to significant IEC increase.

4.4.2. Computational model analysis

One possibility is that upon the addition of silica NPs, the membrane microscale structure becomes different from the pristine polymeric membrane; thus, the structure change influences the ion transport inside the membrane. To get information about the structural properties of membranes, a three-phase model has been utilized [57, 104, 115]. First, membrane ionic resistance under different NaCl solution concentrations (from 0.01M to 0.1 M) was measured, then the measured ionic resistance was converted to ionic conductivity by:

$$k_m = \frac{d}{R} \tag{4}$$

where k_m is the membrane conductivity, d is the membrane thickness, and R is the membrane ionic resistance. The ionic resistance and conductivity values of all the synthesized membranes are listed in Appendix B (Tables 11 and 12). In order to get volume fractions of different phases, we established a simple linear regression model between ln k_m and ln k_2 [57], based on the relation in Eq. (1):

$$ln\, k_m = f_2\, lnk_2 + f_{11} lnk_{11} \tag{5}$$

Figure 17 presents an ln-ln plot of the relation between the conductivities of the electrolyte solution and membrane 1. According to Eq. (5), the slope of the fitted curve is the volume fraction of inter gel phase (f_2); the volume fraction of the total gel phase (f_1) could also be obtained (f_1=1−f_2). Since the sulfonated polymer segments and unsulfonated polymer segments are distinct in terms of ion conduction, the polymer gel phase (f_1) could be further divided into two different phases: pure gel phase (f_{11}) and inert polymer phase (f_{12}). By calculating the degree of sulfonation (DS) of the polymer, the volume fractions of both phases can be obtained (Appendix B.7). Phase volume fractions of the other synthesized membranes can also be calculated by repeating the procedure. From cross-sectional EDX results (Table 10), weight percentages of silicon are very low even for membranes with the highest silica NP loadings. Considering that the size of silica NPs is small (15 – 20 nm, Figure 35), our assumption that the volume of NPs could be neglected is reasonable. Theoretically, membrane pores are the space in membrane matrices that are not occupied by polymer chains (and nanomaterials); thus, they equal the volume fraction of neutral electrolyte solution upon hydration. The porosity of all the synthesized

membranes (wet state) was measured (Appendix B.8). The measured porosity values were quite close to the calculated volume fractions of the electrolyte solution phase (f_2), which testified the validity of the applied numerical model. Furthermore, by substituting membrane conductivity data into Eqn. (2) and (3), we could get insight into ion transport in membranes. The obtained effective ionic diffusion coefficient (presented as D_{eff}/D) and tortuosity factor (τ) reveal how effective the membranes can transport ions and how tortuous the membrane ion channels are, respectively. Since the molar conductivity of ions (sodium ions in this case) in a membrane changes with the concentration [105], ionic conduction of 0.5 M sodium chloride was chosen to calculate the molar conductivity. All the calculated parameters are listed in Table 7.

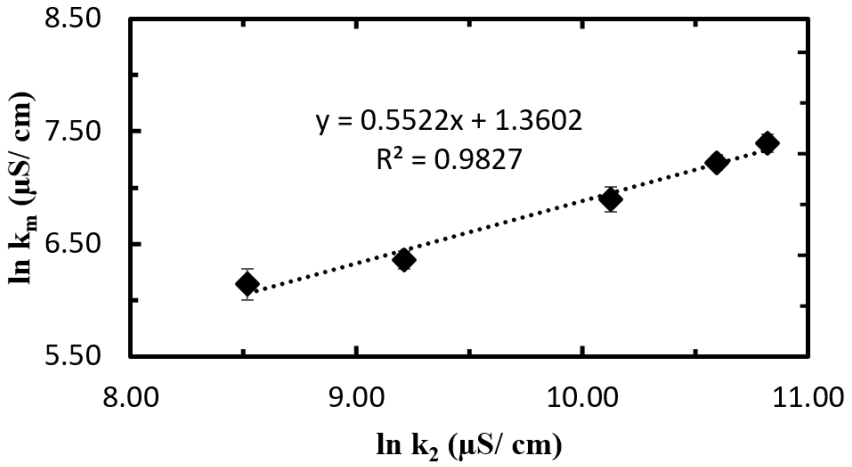

Figure 17 - Plot of ln – ln relation between conductivities of the electrolyte solution and membrane 1 (error bars are +/-1 standard deviations).

Table 7 - Membrane structural and ion transport parameters.

Membranes	f_1 [%]	f_2 [%]	f_{11} [%]	f_{12} [%]	D_{eff}/D	τ
Membrane 1	44.8	55.2	13.8	31.0	0.023±0.001	2.44±0.28
Membrane 2a	40.1	59.9	13.5	26.6	0.046±0.004	1.30±0.21
Membrane 2b	41.6	58.4	14.0	27.6	0.046±0.001	1.27±0.30
Membrane 3a	41.2	58.8	13.8	27.4	0.047±0.002	1.26±0.11
Membrane 3b	41.2	58.8	14.0	27.2	0.046±0.002	1.28±0.08
Membrane 4a	36.8	63.2	13.8	23.0	0.049±0.001	1.30±0.07
Membrane 4b	36.4	63.6	13.5	22.9	0.048±0.005	1.32±0.26
Membrane 5a	41.5	58.5	13.4	28.1	0.043±0.007	1.35±0.38
Membrane 5b	41.6	58.4	13.5	28.1	0.046±0.007	1.28±0.33

4.4.3. Membrane micro-structure and ion transport

Regarding different membrane phases, the change of volume fraction of membrane inter gel phase (f_2) has the same tendency as that of membrane IEC; Membranes 4a and 4b, two membranes with the highest IEC, also have the highest f_2 values. Inversely, as membrane IEC increases, the volume fraction of gel phase (f_1) decreases. From the previous analysis, ion exchange functional groups on silica NPs do not help with the increase of membrane IEC, since the density of those functional groups is negligible compared with that in the polymer. As the membrane SD increases with the increase of NP

loading, it turns out that NPs help to increase the membrane total volume by absorbing more water. As the total volume of water increases in the membrane, the volume fraction of the inter-gel phase (f_2) also increases. When adding NPs, the volume fraction of the membrane gel phase (f_1) decreases, which can be explained by the NP-polymer interaction leading to a compression of the polymer chain. However, NPs can affect different types of polymer chain segments in different ways: 1) sulfonated polymer chains can undergo swelling since the volume fraction of pure gel phase (f_{11}) remains almost unchanged for all the membranes, and membrane total volume increases by absorbing more water and 2) the unsulfonated polymer chains, which are the inert part of the polymer (f_{12}), can show a decrease in volume. Furthermore, the swelling of sulfonated polymer segments might explain the increase of membrane IEC: as the volume of hydrophilic polymer segments increases, ions (Na^+) could have more chances to interact with those segments and thus are easier to retain in the membrane matrices. The increase of membrane surface mean hydrophilicity (as indicated by AFM phase images) might also attribute to the swelling of sulfonated polymer segments; thus, the volume increase of sulfonated part also affects the membrane surface hydrophilicity, since the density of the more hydrophilic sulfonated part also increases on or near the membrane surface.

As a net effect of the membrane micro-structure change upon the addition of silica NPs, the effective ionic diffusion coefficient (represented as D_{eff}/D) increased and the tortuosity factor (τ) decreased. Both parameters refer to ion transport efficiency in membranes by taking bulk solution as a reference. To expand our discussion, we included one more series of PPO based nanocomposite CEMs. The CEMs were synthesized by using functionalized iron oxide [37]. The calculated effective ion diffusion coefficients and

tortuosity factors of those membranes are shown in Appendix B.9. The change of D_{eff}/D and τ with the loading of nanomaterials of all the CEMs is shown in Figure 37. For all the membranes, with the incorporation of nanomaterials, the value of D_{eff}/D increases and the value of τ decreases, which indicates the ion transport efficiency in membranes increases. An optimal loading exists for each type of membrane; however, when the loading of nanomaterials goes beyond the optimal point, a less effective effect appeared, and the increase of ion transport efficiency is hindered (for membranes containing a functionalized iron oxide, the highest loading is the optimal loading [37]). At a loading of zero in each graph, the membranes are all pristine SPPO CEMs, but they all have different IECs; therefore, they all have different D_{eff}/D and τ values. For silica nanocomposite CEMs, membranes with the same NP loadings tend to have similar D_{eff}/D and τ values (Figure 18), indicating that the ion exchange functional groups on the silica NP surfaces have limited influence on the membrane ion transport.

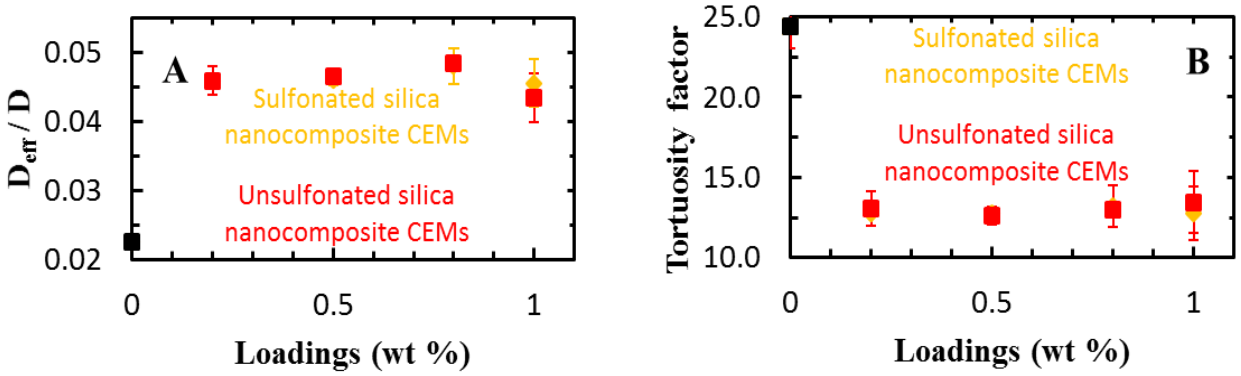

Figure 18 - (A) D_{eff}/D of nanocomposite CEMs and (B) tortuosity factor of nanocomposite CEMs (black dots represent pristine SPPO CEMs, error bars are +/- 1 standard deviations).

Nanomaterials of different shapes and/or different surface functionalization would certainly undergo nanomaterial-nanomaterial and nanomaterial-polymer chain interactions differently, thereby affecting the membrane micro-structure distinctly. As a net effect of membrane micro-structure change, all the nanomaterials help to increase the efficiency of ion transport inside membrane matrices (an increase of D_{eff}/D and a decrease of τ). The volume increase of the membrane pure gel phase (f_{11}) upon the addition of nanomaterials could be attributed to the membrane's increased ion transport efficiency. However, more work needs to be done to determine how the nanomaterial-nanomaterial and nanomaterial-polymer interactions affect the properties of IEMs on a molecular level.

4.4.4. Membrane ion transport properties upon nanomaterial aggregation

As discussed, optimal nanoparticle loadings exist for nanocomposite CEMs, beyond which no further increase of ion transport efficiency occurs. In this study, Membranes 5a and 5b show decreased IEC and increased intrinsic resistance compared with Membranes 4a and 4b, which indicates that Membranes 5a and 5b contain silica NPs that have exceeded or gone past the optimal loading point. As pointed out in previous studies [35, 81, 102], the existence of optimal loadings is related to the aggregation of NPs; hence, aggregation of nanomaterials severely influences the membrane micro-structure, and may even deteriorate membrane ion transport properties. The existence of an optimal loading implies a relationship between the intensity of nanomaterial aggregation and nanomaterial-polymer interaction. An explanation of the phenomenon can be established assuming:

1. Membrane ionic conductivity is linearly related to the number concentration of nanomaterials;

2. Aggregation of nanomaterials in the casting solution is irreversible during the process of membrane forming, and the aggregation driving force has a form similar to the van der Waals force of nanoparticles in aquatic environment [116].

Considering that when aggregation happens, the real number concentration of nanomaterials in the membrane is smaller than that added; thus, the nanomaterial aggregation diminishes the membrane ionic conductivity by decreasing the nanomaterial real number concentration. A simulation of membrane transport efficiency (as D_{eff}/D) against nanomaterial loading successfully reproduces the trend of observed membrane

diffusion coefficient ratios in the experiments using silica nanoparticles. In Figure 19, all the experimental data are within two standard deviations of the model results. In the simulation, as the added nanomaterial concentration increases, nanomaterials have a higher chance to undergo aggregation (Appendix B.9). According to the simulation results, the plateau of D_{eff}/D is attributed to the aggregation of silica NPs. Although the added number concentration of silica NPs increases as the loading increases, the real number concentration does not increase proportionally because of aggregation at higher loadings. Iron oxide (100 μm) based nanocomposite CEMs [37] and silica (30 nm and 420 nm) [41, 113] based nanocomposite CEMs also show good accordance between experimental data and simulation results (Figure 38 (A), (B) and (C)). In addition, the conclusion could also be extended to AEMs; a series of silica-based AEMs [117] yielded similar results (Figure 38 (D)). Model development and simulation algorithm are provided in detail in Appendix B.10.

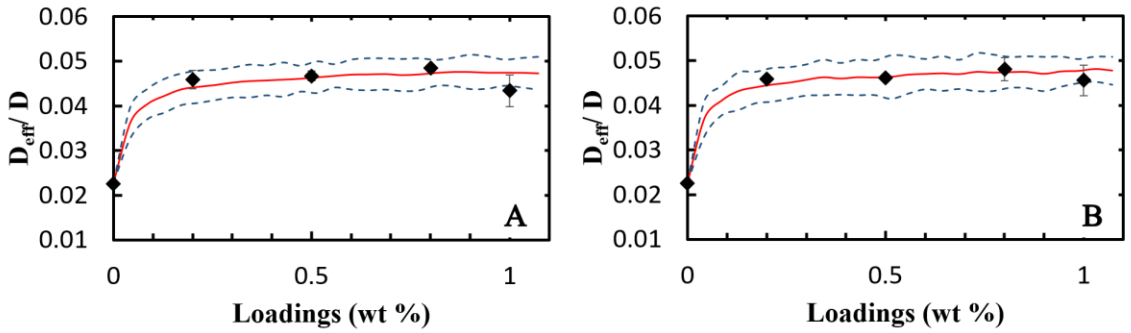

Figure 19 - (A) D_{eff}/D of (A) unsulfonated silica based and (B) sulfonated silica-based nano-composite CEMs as a function of loadings (black dots are the experimental results, red lines are the average values of simulation, and blue dash lines are two standard deviations ($\mu \pm 2\sigma$)).

4.5. Conclusions

Membrane micro-structure change and the influence on ion transport was explored for nanocomposite CEMs. A series of nanocomposite CEMs were synthesized by using SPPO as polymer material and silica NP (unsulfonated or sulfonated) as a nanomaterial. SEM images indicated that the membrane surface morphology did not change much by adding silica NPs; however, membrane surface mean hydrophilicity measured by AFM phase images showed an increase. Both membrane permselectivity and swelling degree (SD) first increased upon addition of silica NPs, then decreased when loading went beyond the optimal value. Membrane IEC and ionic resistance measurements indicated that the enhancement of membrane properties is not related to the type of silica NPs: The functional

groups on the surface of silica NPs did not help increase the density of ion exchange groups. As long as CEMs have the same number (or loading) of NPs, regardless of type, they tend to have the same IEC as well as ionic resistance.

By analyzing the measured data with a computational model, we found that the membrane property change is closely related to the change of membrane micro-structure. With the adding of silica NPs, the interaction between an NP and the polymer chain leads to an increase of the membrane free volume (inter gel phase), allowing the membrane to absorb more water upon hydration. Also, in the presence of NPs, the sulfonated polymer segments tend to expand, while the unsulfonated segments tend to depress. The increase of sulfonated polymer segments (pure gel phase) volume might explain the increase of membrane IEC: Counter-ions have more opportunities to be trapped inside the membranes. The computational model revealed that for both the nanocomposite CEMs synthesized in this study, and nanocomposite CEMs from previous studies [37, 81], the effective ion diffusion coefficient increased and the membrane tortuosity factor decreased after adding nanomaterials. Generally, by the incorporation of nanomaterials, ion transport inside CEMs becomes more efficient. Nanomaterials with different shapes and/ or surface functionality have different nanomaterial and polymer interactions, and influence membrane structure and properties differently, but they all increase membrane ion transport efficiency. The developed simulation model can explain membrane property change upon nanomaterial aggregation. Based on the simulation results, we determined that membrane ion transport property increases with the increase of nanomaterial number concentration, and the membrane ion transport performance reaches a plateau since the increase of nanomaterial real number concentration is influenced by aggregation. The

results of this study can contribute to the value of future designs of new nanocomposite IEMs.

CHAPTER 5. A FREESTANDING GRAPHENE OXIDE MEMBRANE FOR EFFICIENTLY HARVESTING SALINITY GRADIENT POWER

5.1. Abstract

Salinity gradient power (SGP) holds great potential for electricity generation. However, the technology scale-up is hindered by the lack of high-performance membranes. Here we initiate the application of freestanding graphene oxide membranes (GOMs) in pressure retarded osmosis (PRO) to generate SGP. The freestanding GOMs have moderate water permeability coefficient and excellent mechanical strength. Due to their ability to minimize internal concentration polarization (ICP), the freestanding GOMs can achieve high water flux in the osmosis systems, especially when the draw solution concentration is high. By combining experimental work and theoretical calculation, we found that the GOMs can have high power density in the PRO system: a power density of 24.62 W/m^2 is obtained at a hydraulic pressure of 6.90 bar using 3 M and 0.017 M of NaCl as a draw and a feed solution, respectively. This study provides a new way of designing membranes for PRO system, the results show great potential for application of GOMs in PRO to generate SGP.

5.2. Introduction

Providing adequate energy to the human society has become an urgent challenge in the 21st century [1]. Different sustainable energy sources have been explored and some are becoming important supplements to fossil fuels [118]. Salinity gradient power (SGP) is a

type of sustainable energy that has not been fully explored. The SGP is released when two solutions of different salinities are mixed together [10]. Various sources can be utilized to harvest the SGP, ranging from the mixing of seawater with river water to the mixing of artificial solutions with different salt concentrations to harvest waste heat from power plants [6, 12, 81]. SPG represents a huge amount of untapped sustainable energy [18, 119]. The global potential for energy output from estuaries was estimated to be around 2.6 TW, which is about 20% of current energy demand worldwide [5, 120].

The most investigated technology is called pressure retarded osmosis (PRO) [10, 121]. PRO, sharing the same principle with forward osmosis (FO), an emerging technology for water reclamation and desalination [122], is used to harvest renewable energy via the controlled water transport in the energy harvesting system [121]. In the PRO system, Gibbs free energy of mixing is utilized to produce pressurized water flow by allowing water to transport from a freshwater (called feed solution) side into a salty water (called draw solution) side. The mechanical energy from the pressurized salty water is then converted to electricity by using a mechanical turbine [123]. A steady-state, constant-pressure process is the most widely applied to describe the PRO system (Figure 20) [124, 125]. The draw solution first passes through a pressure exchanger, which increases the hydraulic pressure of the draw solution to a constant value, ΔP, and then enters the membrane module. The feed solution enters the membrane module at ambient pressure. The osmotic pressure difference between the draw and feed solutions, which is larger than the hydraulic pressure difference, drives water molecules to transport from the feed solution to the draw solution. The volume of the draw solution then increases, and the salt concentration decreases; the volume of the feed solution decreases, and the salt concentration increases. The pressurized

draw solution then bifurcates into two streams after leaving the membrane module. One stream flows through the turbine to generate electricity, and the other stream flows through the pressure exchanger and transfer pressure to the new draw solution. The hydraulic pressure of the draw solution maintains the constant value ΔP throughout the process until it re-enters the pressure exchanger again. The generated power equals the applied hydraulic pressure difference, ΔP, multiplied by the volume through the turbine [126]. The pressure exchanger requires the same volume on either side, so the water volume through the turbine equals the volume across the membrane, ΔQ. The energy generated from the system is then $\Delta Q \, \Delta P$ [125].

Despite the great potential for energy generation and the state-of-the-art system design, a suitable membrane for PRO is needed before the technology can be scaled up [127]. The use of reverse osmosis (RO) membranes in PRO system resulted in a much lower energy outputs than expected [128-130]. It was concluded that the RO membranes with thick and tortuous support layer designed for desalination were not suitable for PRO application, due to the severe internal concentration polarization (ICP) [128, 131]. When the water transport through the membrane active layer, salt ions get trapped inside the tortuous support layer. The salt concentration inside the support layer increases, leading to a decrease of effective driving force across the membrane active layer. Thus, membranes with lower ICP are urgently needed to increase the energy generation in PRO system. In addition, semipermeable membranes with higher water permeability coefficient were found to be beneficial for power generation in the PRO system [127]. Although many works have been done on the synthesis of new membranes for PRO in recent years [127,

132-134], better approaches for membrane design are needed to further enhance the performance of the PRO system.

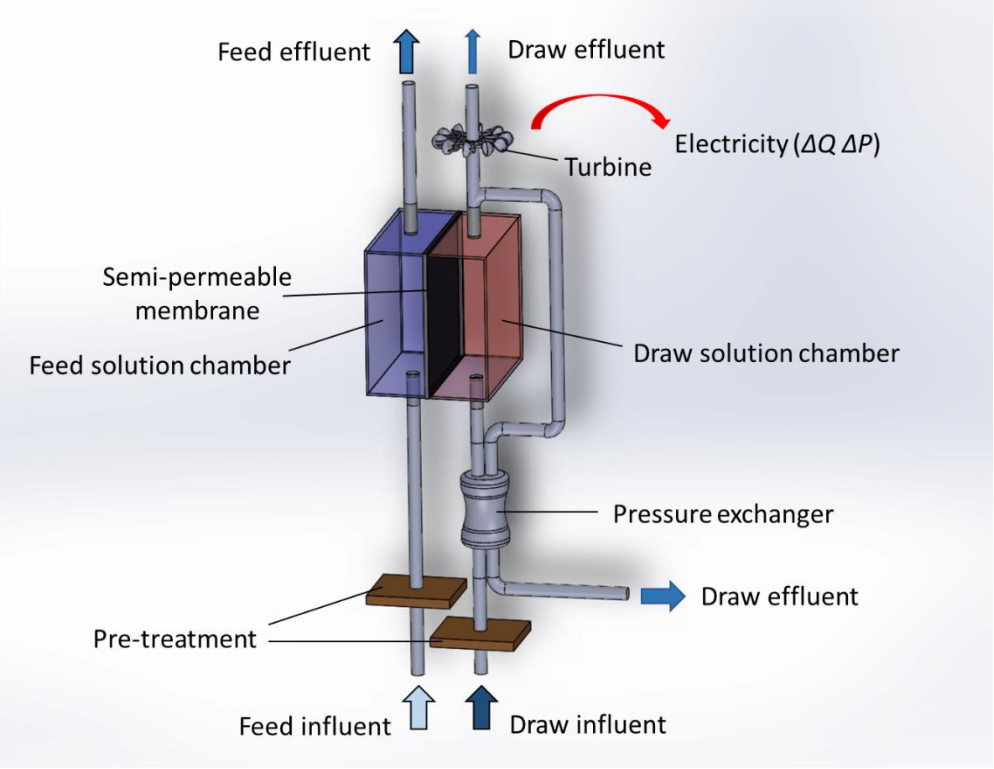

Figure 20 - Schematic representation of a pressure retarded osmosis (PRO) system.

Recently, graphene oxide (GO) has been widely used for the synthesis of separation membranes, due to its good mechanical stability and fast water permeation rate [135, 136]. A capillary model has been proposed to explain the water transport inside the GO membrane (GOM) [137]. According to this model, the pristine regions of the GO form graphene-like capillary networks, and the capillaries allow a low-friction flow of water. Meanwhile, the oxidized regions (containing hydroxyl, carboxyl, and epoxy) are responsible for keeping the interlayer distance. Recent simulations suggest the slow water transport through the oxidized regions inside the GOMs might suppress the nanoconfinement-induced fast water flow [138-141]. Even though more research is needed to fully understand the water transport mechanism, GOMs have already been successfully applied in ultrafiltration and nanofiltration [142-146]. The sharp cut-off for molecules and ions induced by size exclusion makes GOMs perfect for molecular sieving [147]. Interestingly, the attempts to applying the GOMs in osmosis systems (PRO and FO) remain vacant. In this study, we investigate the performance of a freestanding GOM in a PRO system. The current work, by combining experimental and theoretical work, provides a new way of designing customized PRO membranes for salinity gradient power generation.

5.3. Experimental Section

5.3.1. Preparation of GO suspension

Graphene oxide (GO) sheets were synthesized by using a modified Hummer's method [148, 149]. Sodium nitrate ($NaNO_3$, 1 g) was dissolved in 48 mL of concentrated sulfuric acid (H_2SO_4, 98%) in an ice bath. Flake graphite (1 g) was then added to the above mixture while stirring. After 15 min, potassium manganate ($KMnO_4$, 3 g) was slowly added

to the mixture. The mixture was stirred for 30 min while the temperature was maintained below 20 °C, and then the mixture was kept for another 30 min with the temperature set at 35 ± 3 °C. After that, 180 mL of deionized (DI) water was gradually added to the mixture, and then the mixture was kept for 2 h with temperature controlled at 50 ± 3 °C. Finally, 12 mL of H_2O_2 (30 %) and 400 mL of DI water were slowly added to the above mixture to terminate the oxidation reaction. The resulting mixture was centrifuged, and the precipitate was washed one time with diluted hydrochloric acid (HCl, 5%) and four times with DI water. Finally, the precipitate was re-suspended to form GO suspension with a concentration of 1 mg mL^{-1}.

5.3.2. Synthesis and characterization of graphene oxide membranes

GOMs were synthesized by using a vacuum filtration method [150, 151]. An inorganic porous AAO filter (Anodisc, 47 mm in diameter, 200 nm in pore size, Whatman) was chosen as the substrate for the synthesis of freestanding GOMs. GOMs of different thicknesses were obtained by controlling the volume of GO suspension (1 mg mL^{-1}) that was filtered. After the volume of GO suspension was determined (a few milliliters depending on the desired membrane thickness), the GO suspension was further diluted to around 200 mL in volume. As the GO nano-sheets block the pores of the substrate, it took 2 to 5 days to filtrate the 200 mL of GO suspension. The GOM can be easily peeled off the AAO substrate after it is totally dried. The as-prepared GOMs were stored for further characterization. Totally four freestanding GOMs with different thicknesses were synthesized, the membranes were entitled GOM-1 to GOM-4 with the increase of membrane thickness.

SEM images were obtained using a Hitachi SU8010 field-emission SEM (FE-SEM) system. The thickness of the freestanding GOMs was measured using the cross-sectional SEM images. XPS measurements were carried out on a Thermo Scientific K-alpha XPS spectrometer (Thermo Fisher Scientific, USA). XRD patterns were collected using an X'Pert PRO Alpha-1 diffraction system (40 kV, 40 mA). GOM samples were soaked in DI water and sodium chloride (NaCl, 0.5 M) for 24 hours before the wet state XRD patterns were collected. Tensile tests for GOM-1 were carried out on a DMA tester (model Q800, TA Instruments, New Castle, DE, USA) in control force mode at room temperature. The samples were prepared by cutting the GOM-1 into strips with length and width of about 30 mm and 4 mm, respectively (Figure 39a). The sample was mounted on the grips, the gauge length was 5 mm (Figure 39b). During the tests, the force ramping rate was 2N/min. Three samples were tested to obtain the average results.

5.3.3. Determination of membrane transport properties for PRO

Water permeability coefficient (*A*) of the synthesized freestanding GOMs was first measured by using a dead-end stirred cell (Amicon Model 8010, Millipore) with an effective filtration area of 4.1 cm^2 (Figure 40a). The GOMs were cut to fit the size of the filtration stirred cell. DI water was used as the influent to determine the membrane water permeability coefficient (*A*). The setup was driven by nitrogen gas, the external hydraulic pressure during the measurement was set to be 2.07 bars (30 psi). The water permeability coefficient was determined by dividing the pure water flux with the applied hydraulic pressure. At least three samples were tested, and the average values with standard deviations were reported.

In real PRO, the membrane operates in a cross-flow filtration system instead of the dead-end filtration system. Thus, to better investigate the transport properties of the membranes in PRO, the water and salt permeability coefficients of the GOMs were also measured using a modified reverse osmosis (RO) setup (Figure 40b). The feed and permeate channels of the RO cell were used as the draw and feed solutions channels of the PRO cell. In addition, the porous frit in the permeate channel of the RO cell was replaced by a porous spacer (Sterlitech, SEPA CF medium foulant spacer) (Figure 40c) to simulate the PRO conditions [152]. The spacer was cut to fit the RO cell. The cross-flow RO cell has an effective filtration area of 4.1 cm^2. The cross-flow rate was maintained at 0.4 L/min. The influent was circulated and pressurized, and the permeate was collected. The weight change of the permeate was monitored to obtain the water flux. The water permeability coefficient was tested under various applied hydraulic pressures (from 2.07 to 13.79 bar). DI water was used as the influent for the water permeability coefficient measurement. For each hydraulic pressure, the membrane was tested for at least 1 hour to reach a stable water flux, and the average water flux was calculated. The water permeability coefficient was calculated by dividing the pure water flux with the applied hydraulic pressure. The membrane salt permeability coefficient was determined under an applied hydraulic pressure of 5.52 bar (80 psi). 50 mM of sodium chloride (NaCl) solution was used as the influent. The conductivity of the permeate was measured by using a conductivity meter to determine the salt concentration. A commercial thin-film composite (TFC) FO membrane (Hydration Technology Innovations, LLC)) was also investigated for comparison. Salt rejection is defined as:

$$R = 1 - \frac{C_P}{C_F} \quad (6)$$

Where R is the membrane salt rejection, C_P is the salt concentration of the permeate and C_F is the salt concentration of the influent. The salt permeability coefficient (obtained from RO test) is then given by [13, 131]:

$$B = \frac{A(1-R)(\Delta P - \Delta\pi)}{R} \quad (7)$$

where B is the salt permeability coefficient, ΔP is the applied hydraulic pressure, and $\Delta\pi$ is the osmotic pressure (difference).

Alternatively, the membrane salt permeability coefficient can be determined by a forward osmosis (FO) test [127]. A lab-scale cross-flow FO system was used (Figure 41); the customized FO testing cell is 80 mm in length and 40 mm in width. The feed and draw solutions were DI water and 0.5 M NaCl solution, respectively. For the membranes with the support layer (the commercial TFC FO membrane, etc.), the tests were conducted in FO configuration (the active layer facing feed solution and porous support layer facing draw solution) [127]. A silicone gel pad with a hole in the center was set inside the cell, and two spacers were set on both sides of the membrane. The effective area for testing was maintained at 1 cm^2. Feed and draw solutions were pumped into the testing cell, and a counter-current crossflow velocity of 27.8 cm s^{-1} was maintained throughout the tests. The feed solution weight change was recorded every minute by a digital balance to calculate the water flux. The electrical conductivity of the feed solution was measured every ten minutes to determine the (reverse) salt flux. At least 1 hour was logged for each measurement. Membrane salt permeability coefficient and structure parameter can be

calculated by using the measured water flux and reverse solute flux. Based on the mass balance equation on the salt ions in the whole system:

$$C_{F,Bt}(V_0 - J_W A_m t) = C_{F,B0}V_0 + J_S A_m t \quad (8)$$

where $C_{F,Bt}$ is the bulk concentration of the feed solution at time t, V_0 is the initial volume of the feed solution, J_w is the water flux, A_m is the effective membrane filtration area, $C_{F,B0}$ is the initial bulk concentration of the feed solution. $C_{F,Bt}$ and J_w can be calculated from the measured electrical conductivity and the weight change [153]. The reverse salt flux (J_S) can also be derived from [154]:

$$J_S = BC_{D,b}\exp(-\frac{J_W S}{D}) \quad (9)$$

where B is the membrane salt permeability coefficient, $C_{D,b}$ is the bulk concentration of the draw solution, S is the membrane structure parameter, and D is the diffusion coefficient of the draw solution. Membrane structure parameter (S) can be expressed as [155]:

$$S = \left(\frac{D}{J_W}\right)\ln(\frac{B+A\pi_{D,b}}{B+J_W}) \quad (10)$$

where $\pi_{D,b}$ is the osmotic pressure of the bulk draw solution [156]. By combining Equ (3)-(5), J_S, B, and S can then be calculated. The membrane salt permeability coefficient values obtained from the two different approaches were compared and discussed.

5.3.4. Determination of water flux and power density in PRO

The membrane transport performance was further evaluated by using the above crossflow FO setup. Draw solutions were synthetic NaCl solutions with concentrations of

0.5-3 M, and feed solution was DI water. External applied hydraulic pressure was zero for the water flux tests. The membranes with support layers were tested in the PRO configuration (the support layer facing the feed solution) [127]. Water flux and reverse solute flux were obtained by monitoring the change in weight and electric conductivity of the feed solutions. At least three samples were tested and average values with standard deviations were reported.

Meanwhile, since the membrane intrinsic parameters (A, B and S) were already known, water flux (at any applied hydraulic pressure) across the membrane can be calculated [127]:

$$J_W = A\left\{\frac{\pi_{D,b}\exp\left(-\frac{J_W}{k}\right)-\pi_{F,b}\exp\left(\frac{J_W S}{D}\right)}{1+\frac{B}{J_W}\left[\exp\left(\frac{J_W S}{D}\right)-\exp\left(-\frac{J_W}{k}\right)\right]}-\Delta P\right\} \quad (11)$$

where k is the boundary layer mass transfer coefficient, $\pi_{F,b}$ is the osmotic pressure of the bulk feed solution and ΔP is the applied hydraulic pressure. Eqn (6) takes internal concentration polarization (ICP), external concentration polarization (ECP) and reverse solute flux into account. The derivation of Eqn (6) is shown in Appendix C.1. The osmotic pressures of the NaCl solutions were calculated by using the van't Hoff equation [157]. The calculation of the boundary layer mass transfer coefficient (k) is shown in Appendix C.2. The determined value of k for the crossflow FO cell is 26.8 μm/s.

The PRO power density, W, is a function of water flux across the membrane and external applied hydraulic pressure on the draw solution side [123]:

$$W = J_W \Delta P \quad (12)$$

By combining Eqn (6) with Eqn (7), PRO power density (with changing solution concentrations and applied hydraulic pressures) can be calculated.

5.4. Results and discussion

5.4.1. Characterization of materials and membranes

GO sheets were synthesized by a modified Hummer's method [148]. A vacuum filtration method was applied to prepare the freestanding GOMs. XPS spectra of GO sheets (Figure 21a) clearly shows both non-oxygenated carbon (C-C, 285.61 eV) and oxygenated functional groups (C-O, 287.68 eV, and C=O, 288.68 eV). GO sheets dispersed on a silicon wafer were characterized by using SEM, the lateral dimension of the GO sheets is around 1-2 μm (Figure 21b). XRD patterns (Figure 21c) reveals that the dried and wet GOMs have interlayer distances of 0.83 nm and 1.54 nm, respectively. It's worthy mention that the XRD patterns of the GOMs soaked in DI water and NaCl solution (0.5 M) are the same, indicating that the salt ions have negligible influence on the GO interlayer distance. The GO membrane thickness was found to have no influence on the interlayer distance. Generally, the synthesized freestanding GOMs (Figure 21e) have a smooth surface with GO sheets uniformly deposited on the substrate, as can be seen from the surface SEM images (Figure 21f and g).

The freestanding GOMs were found to have good mechanical strength. GOM-1 (the thinnest freestanding GOM synthesized) has much better rigidity and stretch resistance than the tailored TFC membranes [132, 156, 158], as indicated by the measured tensile stress (at break) and Young's modulus (Table 20). Figure 21d listed stress-strain curves of three GOM-1 samples. The average tensile strength (at break) of the GOM-1 is determined

to be 174.5±3.7 MPa, which is much higher than that of tailored thin-film composite (TFC) membranes (about 3-20 MPa) [132, 156, 158]. Also, determined Young's modulus of the GOM-1 (37.3±5.0 GPa) is more than two orders of magnitude higher than that of the typical tailored TFC membranes (80-250 MPa). The good mechanical strength of the GOMs ensures that it can easily resist the osmotic pressure difference in osmosis systems [132, 158]. The burst pressure of the GOM samples was measured by using the modified RO setup and will be discussed later.

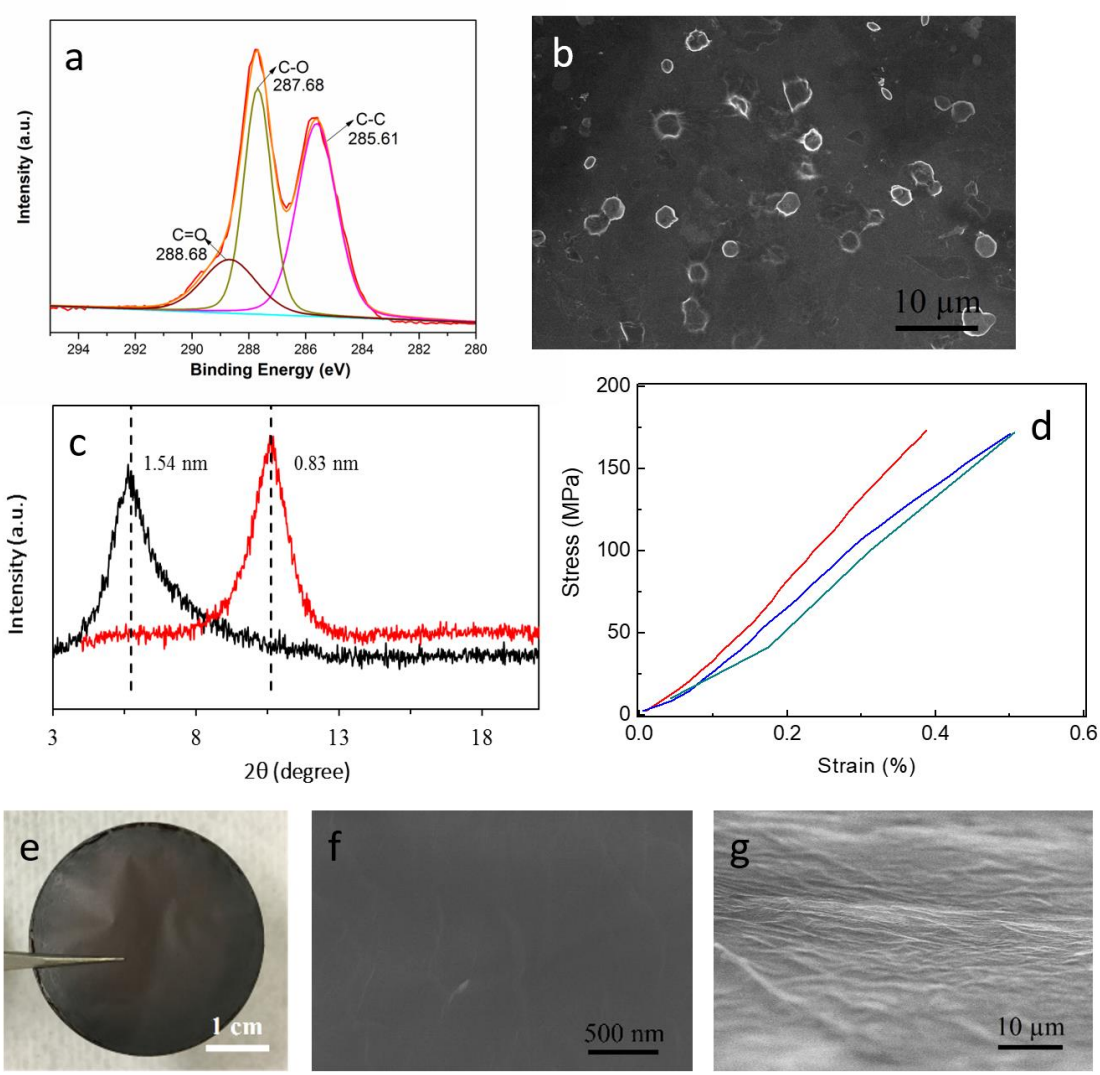

Figure 21 - Characterization of as-prepared GO sheets and freestanding GOMs. (a) C1s XPS spectra of the as-prepared GO sheets. (b) Surface SEM image of GO sheets dispersed on a silicon wafer. (c) XRD patterns of dry (red) and wet (black) GOMs. (d) Stress-strain curve of GOM-1 samples. (e) Digital photograph of the as-prepared freestanding GOM. (f) SEM image of the surface of the as-prepared freestanding GOM. (g) SEM image of the surface of the GOM from a different angle.

5.4.2. Water permeability coefficient of freestanding GO membranes

Figure 22a shows the measured water permeability coefficient as a function of GOM thickness (by using a dead-end filtration setup). The water permeability coefficient decreases significantly with the increase of the GOM thickness. GOM-1 has the highest water permeability coefficient of 4.27 L m^{-2} h^{-1} bar^{-1} (LMH-bar) due to the smallest thickness (1.73 µm). As the thickness increases from 1.73 µm (GOM-1) to 4.12 µm (GOM-4), the water permeability coefficient decreases by almost 40 times. Since the membranes operate in a cross-flow system during PRO process, the water permeability coefficient values measured by a cross-flow system can better represent the membrane performance. Therefore, the water permeability coefficient of the GOM-1 was also determined by using the modified cross-flow RO setup. The commercial TFC membrane was also characterized for comparison. Figure 22b shows the water permeability coefficient of GOM-1 under different hydraulic pressures. The water permeability coefficients of the membranes remain nearly constant across the measured applied hydraulic pressure range. The GOM-1 has a determined average water permeability of 4.40 LMH-bar, which is comparable with the value obtained from the dead-end filtration test. The TFC membrane has an average water permeability coefficient of 1.20 LMH-bar throughout the tested hydraulic pressure range. During the testing, when the hydraulic pressure increased from 6.90 bar (100 psi) to 8.97 bar (130 psi), the water flux of the GOM-1 had an abruptly increase. Which indicates that the burst pressure of the GOM-1 is between 6.90 and 8.97 bar [132]. The membrane cannot maintain the structural integrity beyond the burst pressure. In comparison, the TFC membrane can withstand hydraulic pressure within the tested pressure range up to 14.81 bar (180 psi).

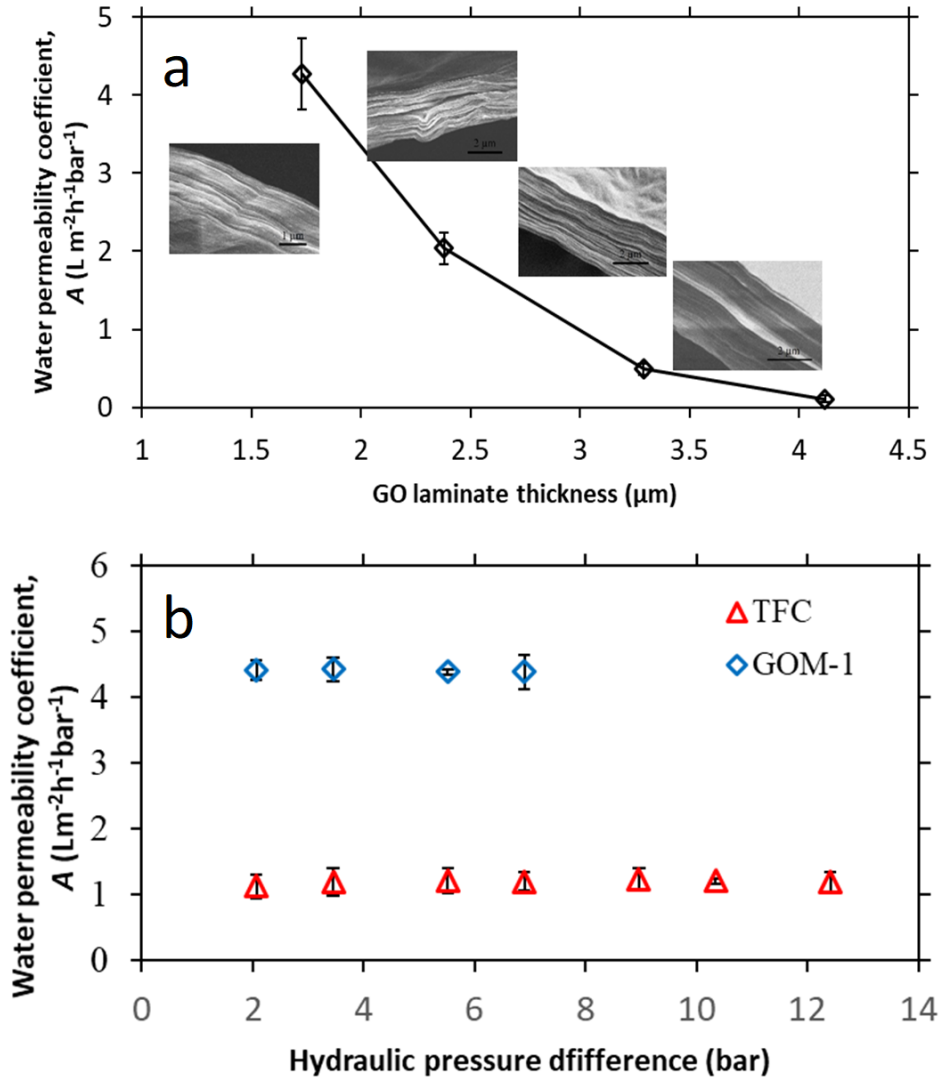

Figure 22 - (a) Water permeability coefficient of GOMs with different thicknesses (measured by using a dead-end filtration system). Inset: corresponding GOMs cross-sectional SEM images. Error bars are ±1 standard deviations. (b) Water permeability coefficient of GOM-1 and commercial TFC membrane under different hydraulic pressure differences (measured by using a modified cross-flow reverse osmosis setup). Error bars are ±1 standard deviations.

5.4.3. Water and salt transport properties of freestanding GO membranes

To characterize the membrane transport properties in osmotic-driven processes, water and salt flux of the GOM-1 was measured in the FO system. As shown in Figure 23a, water flux of the GOM-1 increases almost linearly with the increase of draw solution concentration, reaching a value of 217 LMH when the draw solution concentration is 3 M. The water flux of the GOM-1 is much higher than the TFC membrane (Figure 23b). Water permeability coefficient of the GOM-1 is higher than that of the TFC membrane, so the water flux of the GOM-1 can increase more rapidly with the increase of draw solution concentration. More importantly, due to the elimination of membrane porous support layer, the ICP of the GOM-1 is largely minimized [159, 160], thus the water flux can increase significantly even when the feed solution contains a high concentration of solute (Figure 42).

The reverse salt flux of the GOM-1 increases with the increase of draw solution concentration. With the draw solution concentration increases, the osmotic pressure difference between the feed solution and the draw solution also increases. The increase in the osmotic pressure difference, thus the driving force for salt ion transport, is responsible for the increase in reverse salt flux.

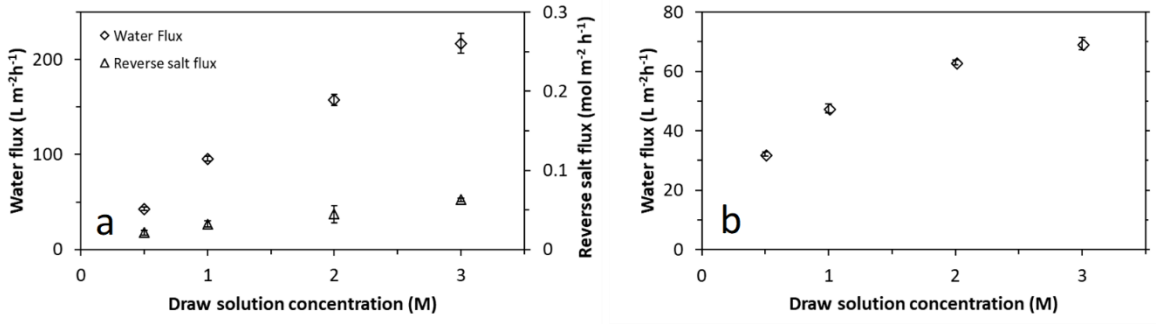

Figure 23 - Measured water flux and reverse salt flux of (a) the GOM-1 and (b) the commercial TFC membrane as a function of draw solution concentration. All the draw solutions used were sodium chloride (NaCl) solutions, and feed solutions were DI water. Error bars are ±1 standard deviation.

As mentioned in the experimental section, the membrane salt permeability coefficient can be determined using two different approaches. The membrane salt permeability coefficient can be obtained from either RO test results (by using Eqn (2)) or FO test results (by combining Eqn (3), (4) and (5)). Since in PRO system, a hydraulic pressure is applied to the draw solution side, the value determined from RO test might better reflect the real situation in PRO. Figure 24a lists the salt permeability coefficient of the GOM-1 and TFC membrane from both FO and RO test. For the TFC membrane, the values determined from the two approaches are quite similar (around 1.3 LMH), indicating the membrane salt transport performance is consistent regardless of whether the hydraulic pressure is applied or not. However, the GOM-1 has distinct salt permeability coefficient in the two systems (0.03 LMH for FO and 11.13 LMH for RO). The inconsistency of salt

permeability coefficient might be explained by the unique transport mechanism of the GOMs. Unlike the polymeric TFC membrane, for which the transport of water and salt ions is governed by a solution-diffusion model [161, 162], the transport inside the freestanding GOMs is likely to be governed by a pore-flow model. During the FO process, the water flux causes convection of the salt ions, which can influence the diffusion process. The convection and diffusion are in the opposite directions, such that when the water flux is high enough, the reverse salt flux can be very low. However, when hydraulic pressure is applied to the draw solution (or permeate) side in PRO (or RO), the salt ions are "pressurized". Since the interlayer distance of the freestanding GOMs is larger than the salt ions (according to the XRD results), the salt ion can readily transport across the GO interlayers under the applied hydraulic pressure, resulting in a large salt permeability coefficient.

The membrane structure parameter (S) was calculated by using the FO results. The structure parameter is related to the ion transport properties of the membrane support layer (substrate) [163]. The GOM-1 and the TFC membrane have a membrane structure parameter of 113 μm and 426 μm, respectively. Due to the elimination of the support layer for the GOM-1, the structure parameter is much lower than the conventional TFC membrane. The small structure parameter of the GOM-1 can potentially reduce the ICP during the osmosis process (Figure 42). The ICP is a major limiting factor that reducing the membrane performance in PRO (and FO) [123], and the minimizing of membrane ICP largely increases the driving force and thus the water flux across the GOM-1. Figure 24b and c list the intrinsic transport parameters of the GOM-1 and the TFC membrane (during PRO), respectively. It should be noted that the salt permeability coefficients obtained from

the modified RO tests were chosen to represent the membrane salt transport properties in PRO. In general, the GOM-1 has higher water permeability coefficient and much lower structure parameter than the commercial TFC membrane, which is beneficial for power generation in PRO; however, the GOM-1 has much higher salt permeability coefficient than the TFC membrane, which might potentially minimize the power generation in PRO system.

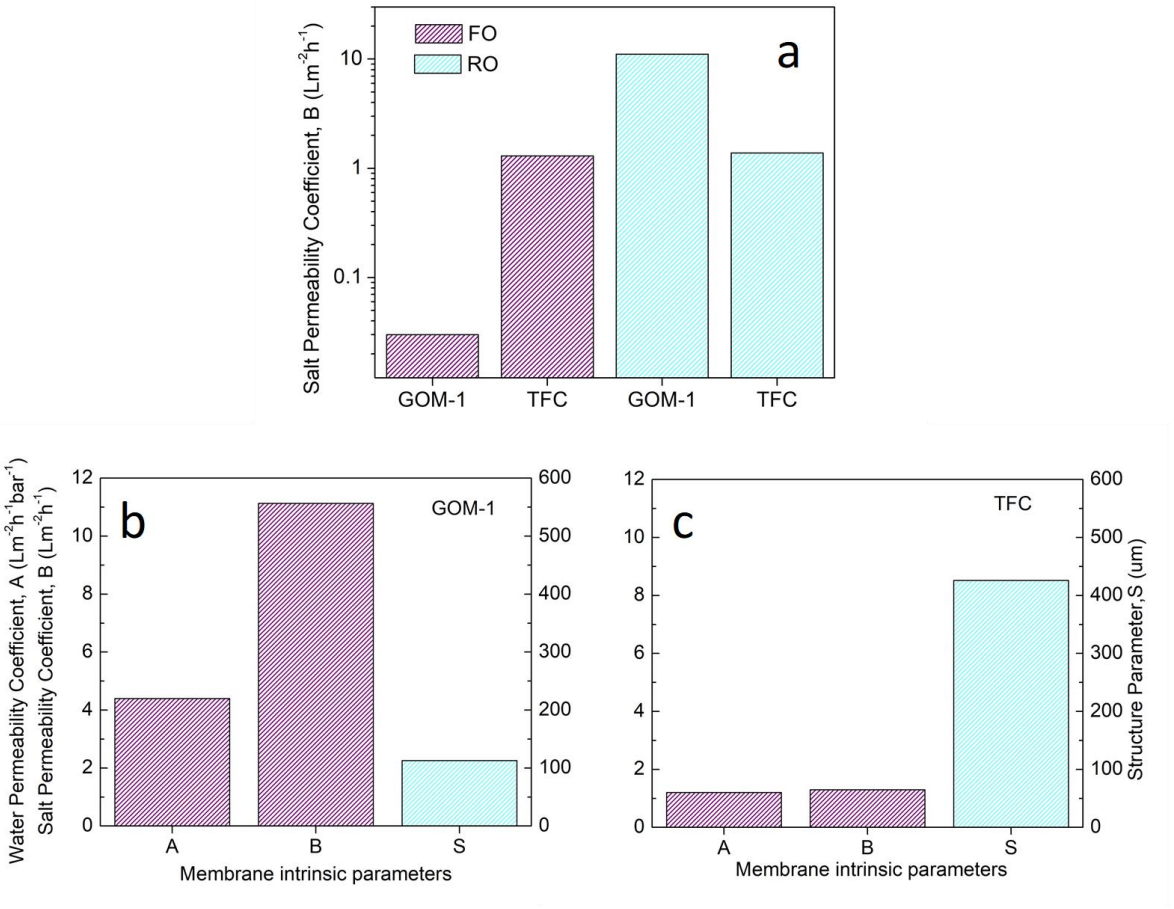

Figure 24 - Membrane intrinsic transport parameters. (a) Salt permeability coefficient of the GOM-1 and TFC membrane from both FO test and modified RO test. (b) GOM-1 and (c) TFC membrane intrinsic transport parameters (water permeability coefficient (A), salt permeability coefficient (B) and structure parameter (S)) in PRO system.

5.4.4. Power generation of freestanding GO membranes in PRO

In a PRO system, power density increases with the increase of applied hydraulic pressure (ΔP) at the draw solution side, and a peak value is reached when the hydraulic

pressure is about half of the osmotic pressure difference across the membrane [127, 131]. Figure 25 shows the calculated power density of the GOM-1 with the change of hydraulic pressure by using various concentrations of draw solutions. River water (0.017 M of NaCl) was chosen as a feed solution in all the cases. Water permeability coefficient measured at each hydraulic pressure (in the modified RO system) was used to calculate the power density under the corresponding hydraulic pressure. Since the burst pressure of the GOM-1 was determined to be between 6.90 and 8.97 bar, the power density was calculated up to a hydraulic pressure of 6.90 bar. As shown in Figure 25, the membrane power density increases significantly with the increase of the hydraulic pressure. When the hydraulic pressure is 6.90 bar, the GOM-1 power density reaches 6.75 W/m^2, 12.81 W/m^2, 19.99 W/m^2 and 24.62 W/m^2 with a draw solution concentration of 0.5 M, 1 M, 2 M and 3 M, respectively. For all the draw solutions, the power densities are lower than the theoretical peak values (Figure 43), since the hydraulic pressure is lower than half the osmotic pressure difference.

The GOM-1 has a water permeability coefficient of 4.40 LMH-bar, which is comparable with that of low-pressure RO membranes [164]. However, the GOM-1 can have a higher power density than that of the polymeric TFC membranes (both commercial and tailor-made) [132, 165]. Previous studies suggest that the membranes with a thinner support layer tend to achieve higher water flux due to the minimizing of membrane ICP [128]. Membrane ICP can even induce a water flux "self-limiting" effect, meaning that for a conventional TFC membrane with a support layer, the water flux stops to increase at high draw solution concentration. In this study, we employ a freestanding GOM for which membrane support layer is not needed. The GOM can significantly minimize membrane

ICP in PRO system, as can be affirmed from the linear increase of water flux with the change of draw solution concentration (Figure 23). As a result, a relatively large effective driving force across the GOM can be maintained, so high water flux and power density can also be achieved. The power density of the GOM-1 is higher than that of the commercial TFC membrane used in this study (under the same hydraulic pressure) (Figure 44), even though the salt permeability coefficient of the TFC membrane is much lower than that of the GOM-1. The high salt permeability coefficient of the GOM-1 increases the reverse salt flux. The increase in reverse salt flux can exacerbate concentrative ECP in this case. The detrimental effect of reverse salt flux works against the benefit of the freestanding GOM to decrease the effective driving force. However, as a net effect, high water flux and power density have still been achieved by using the freestanding GOM. In general, the freestanding GOMs are promising for the application in PRO system for energy generation.

A previous investigation indicates that to make the PRO process commercially viable (for energy generation from the mixing of seawater (0.5 M of NaCl) and river water (0.017 M of NaCl)), the gross power density should be no less than 5 W/m^2. In this study, the GOM-1 needs to operate at a hydraulic pressure of about 4 bars to achieve this goal (Figure 25). According to the experimental results, the TFC membrane cannot achieve this goal (Figure 44), since when the draw solution concentration is 0.5 M, the power density is lower than 5 W/m^2. In the light of the above, another advantage of the freestanding GOM emerges: although some other tailored membranes can also achieve the goal [166], the GOM-1 can operate at a much lower hydraulic pressure, which can largely reduce the pumping energy and increase the net energy gained for PRO system [125]. Due to the small thickness of the freestanding GOMs, much less material is needed to synthesize the same

area of GOMs when comparing with polymeric TFC membranes. For example, by assuming the thickness of the GOM is about 2 μm, more than 200 m^2 of the GOM can be made by using only 1 kg of GO. Since GO can be synthesized by using graphite, an earth-abundant material, the process and application of the GOMs is environmentally sustainable. Although the synthesis of the freestanding GOMs by using vacuum filtration in this study might be energy and time consuming, other synthesis methods such as spray, spin-coating, and casting have been successfully used to synthesis GOMs [137, 167], and can potentially be applied for large-scale synthesis. Those methods are more scalable and less energy intensive, which might ensure large application of freestanding GOMs.

The GOM-1 can achieve even higher power densities theoretically. For example, the peak power density of the GOM-1 is 7.60 W/m^2, 22.30 W/m^2, 58.56 W/m^2 and 98.61 W/m^2 when the draw solution concentration is 0.5 M, 1 M, 2 M and 3 M respectively (assuming the feed solution concentration is 0.017 M) (Figure 43). However, the burst pressure became the limiting factor for the freestanding GOM in its current state to achieve higher gross power density. In addition, previous studies show that the poor stability in water prevents the large-scale application of GOMs to produce clean water and energy [168]. The low burst pressure of the GOM in this study might be caused by its poor stability in water. Although the GOM has high tensile strength, it becomes susceptible to external pressures once exposed to water. The oxidized groups can form hydrogen with water molecules [149], and the carboxyl groups become negatively charged upon hydration [151]. Both effects would create repulsive force among GO sheets and thus decrease the stability of the GOM in water. In this study, at least 1 hour was logged for the modified RO and FO tests, and the structure and transport properties of the freestanding GOM were

found to be stable during the tests. The GOM also maintained structural integrity after soaking into the water for 24 hours before the XRD measurement. The AAO filter used during the GOM synthesis is thought to be responsible for the increased stability of GOM in water [151]. Despite the positive results regarding the GOM stability in this study, experiments with longer testing time are needed to further explore the long-term stability of GOM. It remains challenging to increase the stability of GOM in water while maintaining the unique layered structure and outstanding transport properties. Fortunately, previous studies show that GOMs with even better mechanical properties can be synthesized [135, 169, 170], and different ways of increasing the GOM stability in water have been proposed [171-173]. Also, by carefully designing and controlling the fabrication process, the water permeability coefficient of the GOMs can be further enhanced [167, 174, 175]. The above efforts can be readily applied to PRO system for salinity gradient power generation, and membranes with better power generation performance can be expected.

The current work initiates a method for designing freestanding membranes for osmosis processes by using the GO material. By combining experimental work and theoretical calculation, we show that freestanding GOMs can achieve high power density in the PRO system. The results from this study indicate that the elimination of the membrane support layer can significantly increase water flux and power density. Despite the promising results from this study, further study is needed to investigate the power generation property of the GOMs in real PRO systems. Also, the investigation of alternative fabrication methods to synthesize GOMs and the applications of the resulted GOMs for power generation will be beneficial to further increase the power density.

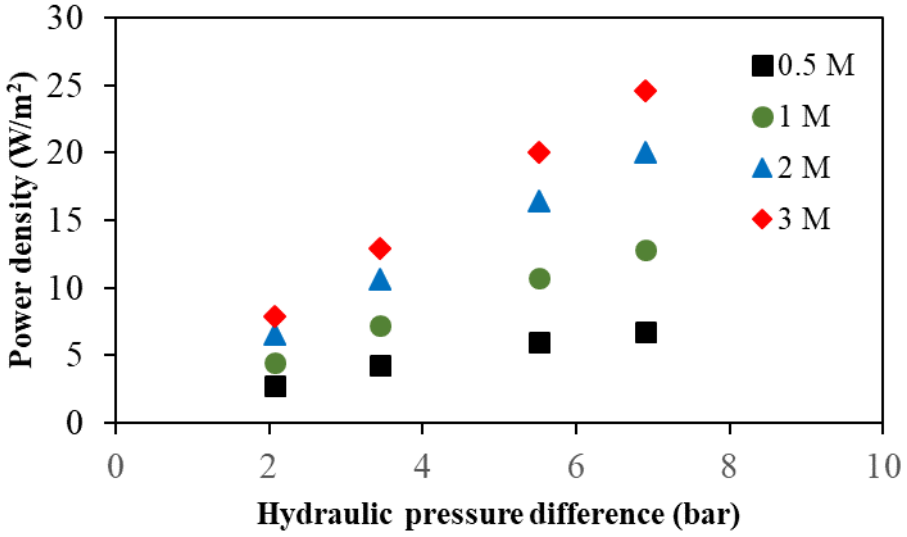

Figure 25 - Plots of GOM-1 power density as a function of hydraulic pressure in PRO system, with solutions of different NaCl concentrations acting as working solutions. The concentration of feed solution is 0.017 M of NaCl. (The solutions with concentrations of 0.017 M, 0.5 M, 1 M and 3 M represent river water, seawater, seawater brine (50% recovery) and hyper brine, respectively. The concentration of hyper brine is in the salinity range of the Great Salt Lake.)

5.5. Conclusions

In summary, ultrathin freestanding GOMs was synthesized and the performance in the PRO system was first evaluated. The freestanding GOMs showed moderate water permeability coefficient and excellent mechanical strength. Due to the elimination of the membrane support layer, the freestanding GOMs can mitigate internal concentration polarization during the PRO process. Although the GOMs showed high salt permeability

coefficient when hydraulic pressure is applied to the draw solution side, high water flux and high power density were obtained. Under a hydraulic pressure of 6.90 bar, the GOM-1 (thinnest synthesized freestanding GOM) achieved a power density of 6.75 W/m^2, 12.81 W/m^2, 19.99 W/m^2 and 24.62 W/m^2 with a draw solution concentration of 0.5 M, 1 M, 2 M and 3 M, respectively (0.017 M solution acting as feed solution). Furthermore, higher power density can be achieved by designing GOMs with better mechanical strength and higher water flux. In general, the current study initiates a new way of designing PRO membranes and represents a step forward towards the application of the PRO for sustainable energy generation.

CHAPTER 6. LOW-GRADE WASTE HEAT RECOVERY VIA OSMOTIC HEAT ENGINE BY USING A GRAPHENE OXIDE MEMBRANE

6.1. Abstract

An osmotic heat engine is a brand-new and promising technology for the harvesting of low-grade waste heat from various sources. However, the lack of an adequate semi-permeable membrane hinders the advancing of the technology. In this study, we investigated the application of a freestanding graphene oxide membrane (GOM) in the osmotic heat engine for energy generation. The synthesized GOM has a water permeability coefficient of 4.4 L m^{-2} h^{-1} bar^{-1} (LMH-bar). The internal concentration polarization (ICP) in the osmosis filtration system can be minimized since no membrane support layer is needed for the freestanding GOM. As a result, high water flux and high-power density are obtained. For example, under an applied hydraulic pressure of 6.90 bar, with a 2M draw solution of ammonium bicarbonate solution, a power density of 20.0 W/m^2 is achieved. This study shows that the freestanding GOM is promising for application in the osmotic heat engine. Future research regarding improving the mechanical properties and water stability of the GOM is beneficial for further advancing the technology.

6.2. Introduction

Current excessive reliance on nonrenewable, carbon-emitting fossil fuels to generate energy creates severe problems such as climate change and environmental pollution[176, 177]. Developing sustainable energy technologies and enhancing the energy

utilization efficiency of existing industrial processes are two effective methods to reduce the negative effects of fossil fuels[7, 178, 179]. More than 30% of the energy supply is consumed by industrial processes in the U.S., and 20–50% of the consumed energy is lost in the form of waste heat[7]. Utilizing this waste heat can increase the energy efficiency of those processes and also prevent thermal pollution,[180] thereby transforming an environmentally harmful process to an environmentally benign process. In addition, a significant amount of untapped heat energy is also available from geothermal and solar-based processes[1].

The most efficient way of using the untapped waste heat is directly utilizing it for heat pumps and space heating. However, the direct onsite uses are largely confined to the locality of the waste heat sources[181]. Hence, when matching needs for direct utilization are absent near the sources, converting the waste heat into electricity becomes the only option available. However, less than 10% of the waste heat from industrial processes has the high quality needed for electricity generation via existing technologies.[182] The remaining 90% is in the form of low-grade waste heat with a temperature below 130 °C[183]. Besides, a large amount of thermal energy exists in the Earth's crust. To convert geothermal energy into electricity, access to a high-temperature heat source by drilling is necessary, since the more easily accessible low-grade heat cannot be utilized to generate electricity with existing methods[181, 184]. The development of new technologies that can efficiently convert low-grade heat into electricity is, thus, beneficial towards utilizing waste heat as a sustainable energy source.

The membrane-based heat engine is a promising technology that can convert low-grade heat into electricity[6, 185]. The closed-loop power system is composed of two parts:

electricity generation and thermal separation. The electricity generation part converts the energy released from the controlled mixing of two solutions with different salinity gradients (salt concentrations) into electricity[6]. The principle of pressure retarded osmosis (PRO) is utilized in the heat engine to produce pressurized water flow. With the help of a semi-permeable membrane, water molecules can transport from the low salt concentrated solution (feed solution) to the high salt concentrated solution (draw solution). The kinetic energy from the pressurized draw solution is then converted to electricity by using a mechanical turbine[123]. Since osmotic pressure acts as the driving force in the electricity generation part, the technology is best represented by the osmotic heat engine. The osmotic heat engine is the most widely studied membrane-based technology for low-grade heat harvesting; however, other membrane-based systems have also been proposed and evaluated[186]. Alternatively, by regulating the ion transport of different charges, osmotic ion flux can be generated inside the system. The ion flux can then be converted to an electron flow by using electrodes, whereby electricity can be generated.[15, 81] Different from the osmotic heat engine, the above technology uses permselective ion exchange membranes (IEMs)[44, 187] to produce an osmotic ionic current known as reverse electrodialysis (RED) to power the heat engine[188, 189].

The thermal separation part of the osmotic heat engine regenerates the draw solution and feed solution by using waste heat as an energy source[6]. Different working electrolyte solutions have been evaluated to maximize energy production[190]. Generally, the salts that form the electrolyte solutions should pose high solubility in water (or other solvents), which provides a large driving force that is easy to regenerate[6, 189].Inorganic ionic salts, such as sodium chloride, were investigated in previous studies[191, 192]. In

those cases, the waste heat was used to reconcentrate the draw solutions by vaporizing part of the water. However, the energy-intensive vaporization process leads to a low thermal efficiency[6]. Alternatively, solute extraction was applied to regenerate the draw and feed solutions[189]. The salt ions transferred from the draw solution into the feed solutions can be extracted during the thermal separation step. Compared to conventional ionic salts, the thermolytic salts (ammonium bicarbonate) were found to have a higher conversion efficiency of the low-temperature heat sources to power. The thermolytic salts in the aqueous phase can be converted to gaseous species (ammonia and carbon dioxide) upon heating, and the releasing and resolubilization of the gas molecules can lead to the regeneration of the feed and draw solutions, respectively (Figure 26).

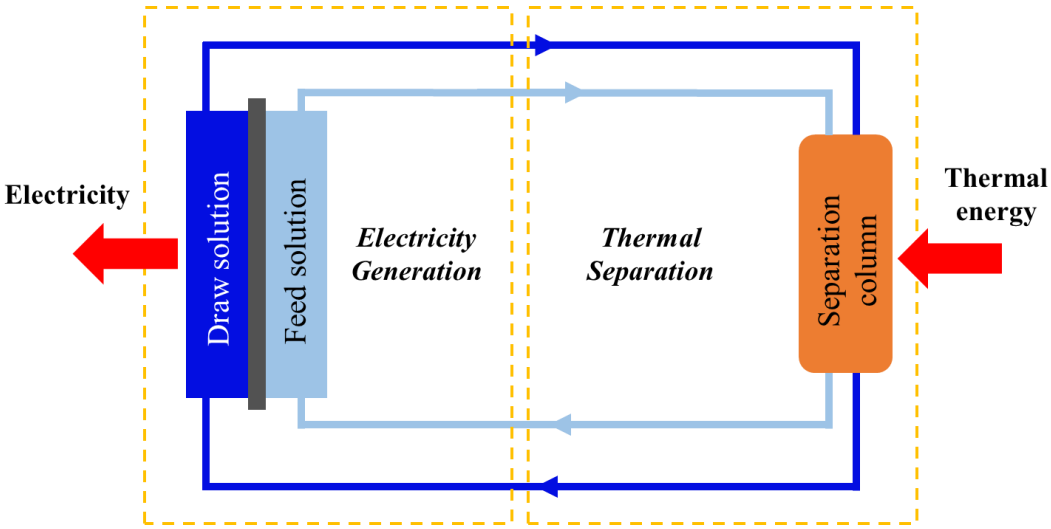

Figure 26 - Schematic illustration of a membrane-based osmotic heat engine for low-grade waste heat harvesting.

Despite the great progress that has been made in thermodynamic analysis,[6, 181, 193] techno-economic assessment[7] and alternative solute and solvent investigation,[190, 194, 195] research on the development of membranes for the osmotic heat engine is scarce. The semi-permeable membrane plays an important role in the osmotic heat engine; however, the major obstacle to improving the technology is the lack of an adequate membrane. The transport properties of the membrane determine water flux and, thus, the power generation of the entire system. Conventionally, a thin-film composite (TFC) membrane is applied in the system to generate permeate water flux[6]. However, the existence of the membrane porous support layer results in an internal concentration polarization (ICP), which decreases the effective driving force across the membrane and adversely affects the performance of the system[159, 196].

In this study, we investigate the application of a freestanding graphene oxide membrane (GOM) in the osmotic heat engine. GOM has been applied in many separation practices due to its excellent transport properties and sharp molecular cut off[137, 147, 167, 197]. By using a freestanding GOM, we aim to minimize the effect of ICP, increase water flux, and eventually enhance the energy generation of the osmotic heat engine system. The water and ion transport properties of the GOM have been extensively studied. By combining experimental work and theoretical modeling, the feasibility of the freestanding GOM for application in the osmotic heat engine was explored and the results are discussed herein.

6.3. Materials and Methods

6.3.1. Synthesis of GO membranes

GO dispersions were synthesized via a modified Hummer's method for which graphite was oxidized using a combination of sodium nitrate, concentrated sulfuric acid and potassium permanganate under controlled reaction temperature[148, 149]. Then, hydrogen peroxide was added to terminate the oxidation reaction. The mixture was then washed several times with deionized water. Finally, the precipitate was re-dispersed in deionized water to form GO dispersion with a concentration of 1 g/L.

The freestanding GOMs were synthesized by using a vacuum filtration method[151, 198]. The as-prepared GO dispersion was first diluted with deionized water and then filtrated through an inorganic Whatman anodisc AAO 47-mm diameter filter with a 0.2 μm pore size (Whatman, Inc., Clifton, NJ, USA). The AAO filter was proven successful when used to synthesize freestanding GOMs with good stability[151]. The GOM can be easily peeled off the AAO filter, forming a freestanding membrane after the filtration process is complete. According to previous studies, the water permeability coefficient of the GOM decreases with the increase of membrane thickness[143, 199]; therefore, in this study, we tried to synthesize freestanding GOMs as thin as possible to ensure a high water permeability coefficient but, at the same time, we kept enough thickness to ensure reasonable mechanical strength.

6.3.2. Characterization of GO membrane

GO chemistry was analyzed by a Thermo Scientific K-Alpha X-ray photoelectron spectrometer (XPS) system (Thermo Fisher Scientific, USA). SEM images were obtained on a Hitachi SU8010 field emission SEM (FE-SEM) system. The thickness of the GOMs was measured by using a micrometer. X-ray diffractometry (XRD) was carried out on an

X'Pert PRO Alpha-1 diffractometer (40 kV, 40 mA) for both dry and wet GOM samples. The wet sample was prepared by soaking the GOM in DI water for 24 h before characterization.

6.3.3. Measurements of GO membrane transport properties

Membrane water permeability coefficient (*A*) and salt permeability coefficient (*B*) were measured via a modified reverse osmosis (RO) test cell by using deionized (DI) water and salt solutions, respectively. A previous study pointed out that in a conventional RO experiment, the membrane does not deform since the permeate channel is supported by a porous frit. Hence, the measured membrane *A* and *B* values in the RO testing cell would be different from that of a deformed membrane in a PRO testing cell[152]. In this study, the porous frit in the RO testing cell was replaced by a porous mesh-type SEPA CF medium foulant spacer (Sterlitech, Corp., Kent, WA, USA) (Figure 45) to determine the A and B values suitable for PRO. The modified RO testing cell has an effective area of 4.1 cm^2. During the experiment, the feed and permeate channels of the modified RO testing cell acted as draw and feed solution channels of the PRO cell, respectively (Figure 45). The influent feed solution was pressurized and circulated in the feed channel with a flow rate of 400 mL/min, and the permeate was weighted on a minute basis using a digital balance. DI water was used as the permeate for the determination of the water permeability coefficient. The weight change of the permeate was used to calculate the water flux and water permeability coefficient. The membrane was tested for one hour under each applied hydraulic pressure (from 2.07 to 8.97 bar), and the water permeability coefficient (*A*) was determined by dividing the water flux by the hydraulic pressure ($A = J_W/\Delta P$)[127, 131].

The membrane was tested under a hydraulic pressure of 3.45 bar (50 psi) for 1 hour to determine the salt permeability coefficient (*B*). The membrane salt rejection (*R*) was tested in the modified RO cell by using both sodium chloride solution (NaCl, 50 mM) and ammonium bicarbonate solution (NH_4HCO_3, 50 mM). A conductivity meter was used to measure the conductivity of the feed and permeate solutions to calculate the membrane salt rejection[185]. The salt permeability coefficient (*B*) is then calculated by[13, 131]:

$$B = \frac{A(1-R)(\Delta P-\Delta\pi)}{R} \quad (13)$$

where ΔP is the hydraulic pressure, and $\Delta\pi$ is the osmotic pressure of the feed solution in the modified RO test.

6.3.4. Determination of water flux and projected power density in PRO system

A customized counter-current cross-flow forward-osmosis (FO) test cell (8 cm in length and 4 cm in width) was used to measure the GOM water flux. A silicon pad with a hole (1 cm × 1 cm) in the center was inserted into the test cell to create an effective testing area of 1 cm^2. A mesh-type spacer was used inside both the feed and draw solution chambers. During the experiment, the feed and draw solutions were pumped into the chambers with a cross-flow velocity of 27.8 cm/s. The weight and concentration change of the feed solution were monitored by digital balance and a conductivity meter to calculate the water flux and (reverse) salt flux, respectively. The test was run for at least one hour for each measurement and the average value was calculated.

The water flux was first measured with 1 M NaCl as a draw solution and then a DI water as a feed solution. To investigate the influence of solution pH on the water and salt

transport across the GOM, the pH of the feed and draw solutions was adjusted by adding HCl or NaOH. Next, the water flux was measured by using NH_4HCO_3 solutions (0.5 M, 1 M, 1.5 M and 2 M) as draw solutions, and DI water as feed solution. To evaluate how well the GOM can mitigate the ICP during the PRO, NaCl and NH_4HCO_3 solutions (0.1 M) was used as the feed solution. The corresponding water flux for each draw and feed solution was calculated.

Additionally, the water flux and projected power density for PRO when a hydraulic pressure is applied was calculated using equations from previous studies[127, 200] .Specifically, by considering the effects of ICP, ECP and (reverse) salt permeation[127]:

$$J_W = A\left\{\frac{\pi_{D,b}\exp\left(-\frac{J_W}{k}\right)-\pi_{F,b}\exp\left(\frac{J_W S}{D}\right)}{1+\frac{B}{J_W}\left[\exp\left(\frac{J_W S}{D}\right)-\exp\left(-\frac{J_W}{k}\right)\right]}-\Delta P\right\} \quad (14)$$

where J_w is the water flux, $\pi_{F,b}$ is the osmotic pressure of the bulk feed solution, $\pi_{D,b}$ is the osmotic pressure of the bulk draw solution, D is the bulk diffusion coefficient, S is the membrane structural parameter, k is the boundary layer mass transfer coefficient, and ΔP is the applied hydraulic pressure. The van't Hoff equation was used to calculate the osmotic pressure of the solutions by assuming that the osmotic pressure is linearly proportional to the salt ion concentration[127]. The value of k was determined by using a previously reported procedure[159]; the value was determined to be 26.8 μm/s. In the PRO system, the power density (W) is the product of the water flux across the membrane and the applied hydraulic pressure on the draw solution side:

$$W = J_W \Delta P \quad (15)$$

6.3.5. Estimation of system energy efficiency

The osmotic heat engine consumes thermal energy to separate the solute from the mixed solution and to generate power by mixing the diluted solution and pressurized concentrated solution[181]. The energy efficiency of the overall system can be expressed as:

$$\eta = \frac{P}{q_H} \tag{16}$$

where η is the energy efficiency of the osmotic heat engine, P is the energy generated from the electricity generation stage, and q_H is the thermal energy consumed to (re)generate the draw and feed solutions. By analysis of the osmotic heat engine process in this study (Figure 46), the energy efficiency can be calculated by:

$$\eta = \frac{W}{\beta J_W (c_d - c_f)} \tag{17}$$

where β is the specific heat duty of ammonium bicarbonate, c_d is the concentration of the draw solution, and c_f is the concentration of the feed solution. Eq. (5) indicates that the energy efficiency is independent of membrane area and operation time. More detailed calculation of the system energy efficiency is shown in the Appendix D.1.

6.4. Results and Discussion

6.4.1. Material characterization

According to the C1s XPS spectra (Figure 27a), both non-oxygenated carbon (C-C, 285.60 eV) and oxygenated carbon (C-O, 287.72 eV and C=O, 288.50 eV) can be

identified from the synthesized GO. The GO sheets were dispersed on a silicon wafer and then characterized by SEM. The SEM image (Figure 27b) indicates that the GO sheet has an average dimension of 2–3 μm. The photograph (Figure 47) of the synthesized freestanding GOM indicates it is circular with a uniform thickness. The surface morphology of the freestanding GOM synthesized with the AAO filter was determined by the SEM, and a smooth surface was observed (Figure 27c), which is similar to previous studies[151, 201]. The thickness of the freestanding GOM was measured by using a micrometer. To ensure the synthesized GOM has a high water permeability coefficient, we have made the GOM as thin as possible. The thinnest GOM we were able to synthesize has a thickness of 1.73 μm. GOMs with a smaller thickness do not have enough mechanical stability; they tend to break easily or are difficult to peel off the AAO filter. The GOM cross-sectional SEM image (Figure 27d) reveals a well-packed layered structure throughout the GOM sample. The layered structure of the GOM was evidenced via its X-ray diffraction (XRD) pattern (Figure 47). The dry and wet GOMs have an interlayer spacing of 0.83 nm and 1.54 nm, respectively. The GOM with a thickness of 1.73 μm was extensively characterized in terms of transport properties and power generation performance in the osmotic heat engine.

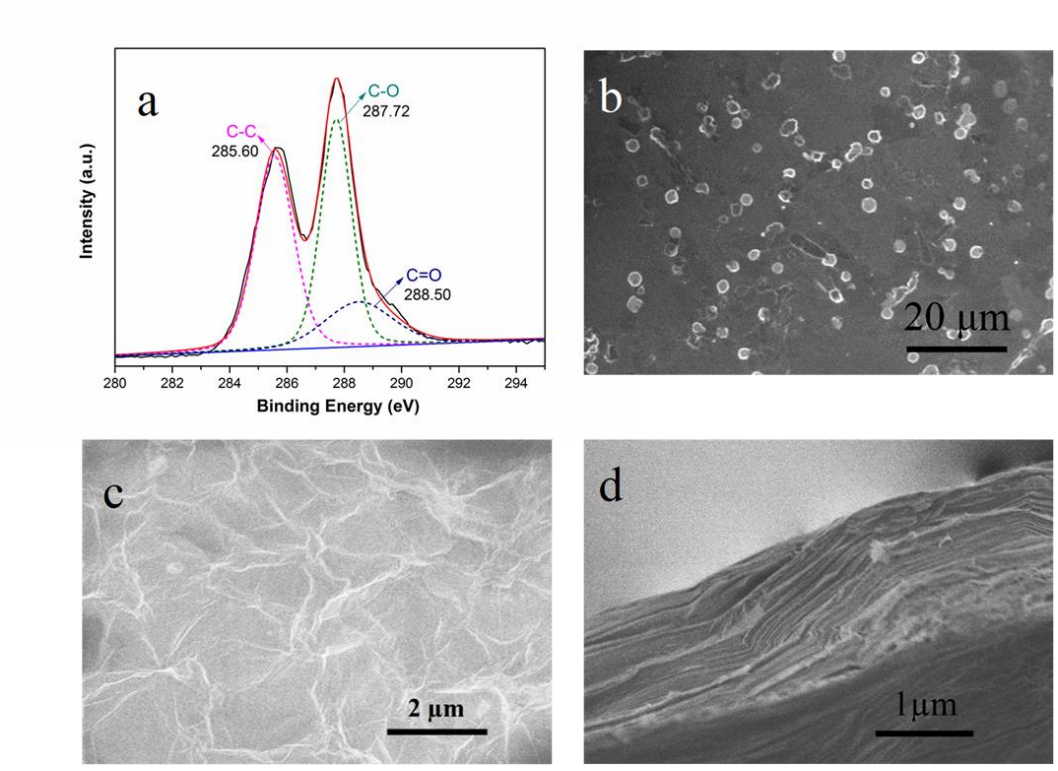

Figure 27 - Characterization of GO and freestanding GOM. (a) Fitting results of C1s XPS spectra of the GO material, (b) SEM image of GO sheets dispersed on a silicon wafer, (c) surface SEM image of the freestanding GOM, and (d) a cross-sectional SEM image of the freestanding GOM.

6.4.2. GO membrane water and ion transport properties

Water permeability coefficient (*A*) of the freestanding GOM was determined by using the modified RO testing cell. Figure 28a lists the water permeability coefficient of the GOM under the different hydraulic pressures. The water permeability coefficient is consistent across all the measured hydraulic pressure range (from 2.07 bar to 6.90 bar),

indicating negligible membrane compaction. A water permeability coefficient of 4.4 L m^{-2} h^{-1} bar^{-1} (LMH-bar) was determined for the GOM by averaging the water permeability coefficients obtained from different hydraulic pressure values. The burst pressure of the GOM was determined to be between 6.90 bar and 8.97 bar. During the experiment, when the hydraulic pressure increased from 6.90 bar to 8.97 bar, there was a sharp increase in water flowrate across the membrane[202, 203], indicating that under the hydraulic pressure of 8.97 bar, the membrane could not maintain structural integrity. The membrane salt permeability coefficient was calculated based on the results from the modified RO tests. With a transmembrane hydraulic pressure of 3.45 bar, 50 mM of NaCl and NH_4HCO_3 solutions were used as the feed solutions, respectively. For the NaCl solution, a rejection of 32.64 % yields a salt permeability coefficient (*B*) of 11.13 LMH. For the NH_4HCO_3 solution, a slightly higher rejection of 34.58 % results in a salt permeability coefficient of 10.20 LMH.

The GOM was also tested under a lab-scale FO system, to further characterize the transport properties as well as estimate the PRO power generation preformation. First, 1 M of NaCl solution and DI water were chosen as draw and feed solutions, respectively. To investigate the influence of solution pH on the transport of the GOM, the draw and feed solutions with different pH values were used. Figure 28b shows the water and (reverse) salt flux under various pH values. The water and salt flux remain almost unchanged across the entire investigated pH range, suggesting that solution pH has a negligible influence on the GOM water and salt transport in the osmosis process. The carboxyl group, existing at the edge of the GO sheets[204], has been reported to play an important role in ion exchange and adsorption[205, 206]. As a weak acid, carboxyl has a pKa value of about 4.8. When

the solution pH increases, carboxyl groups become deprotonated, which could increase the charge density of the GOM. As a result, the transport of the charged species, such as ions, can be potentially influenced. However, the ion transport of GOMs during osmosis was unaffected. A possible explanation is that the density of the carboxyl group is not high enough, so the influence of the carboxyl on the ion transport during osmosis can be neglected.

Then, the membrane water flux was measured by varying the concentration of the draw solution. Figure 28c shows the water flux changing with the increase of the NaCl draw solution concentration. When DI water acts as the feed solution, the water flux increases almost linearly with the increase of the draw solution concentration. The water flux increases from 42.5 LMH for 0.5 M draw solution to 157.5 LMH for 2 M draw solution. The change of water flux shares the same trend with 0.1 M of NaCl solution acting as the feed solution. However, due to the slightly decreased concentration gradient, the GOM experiences a reduced effective driving force, and the water flux is lower than that when DI water is used as the feed solution. The linear increase of water flux with the increase of the draw solution concentration indicates the weakening of internal concentration polarization (ICP). ICP is a major limiting factor hindering the performance of the FO and PRO membranes[123]. For a conventional thin-film composite (TFC) membrane, when salt ions get trapped inside the membrane support layer, the effective driving force across the membrane can decrease significantly, leading to a much lower water flux than expected[159]. However, by using the freestanding GOM, the ICP can be reduced due to the elimination of the membrane support layer. As a result, a larger driving force can be maintained, and a higher water flux can be achieved. Similar water flux results

were obtained when replacing NaCl solution with NH_4HCO_3 solution, as shown in Figure 28d. The application of the freestanding GOM results in a significant reduction of the membrane ICP, which is beneficial for power generation in the PRO and osmotic heat engine systems.

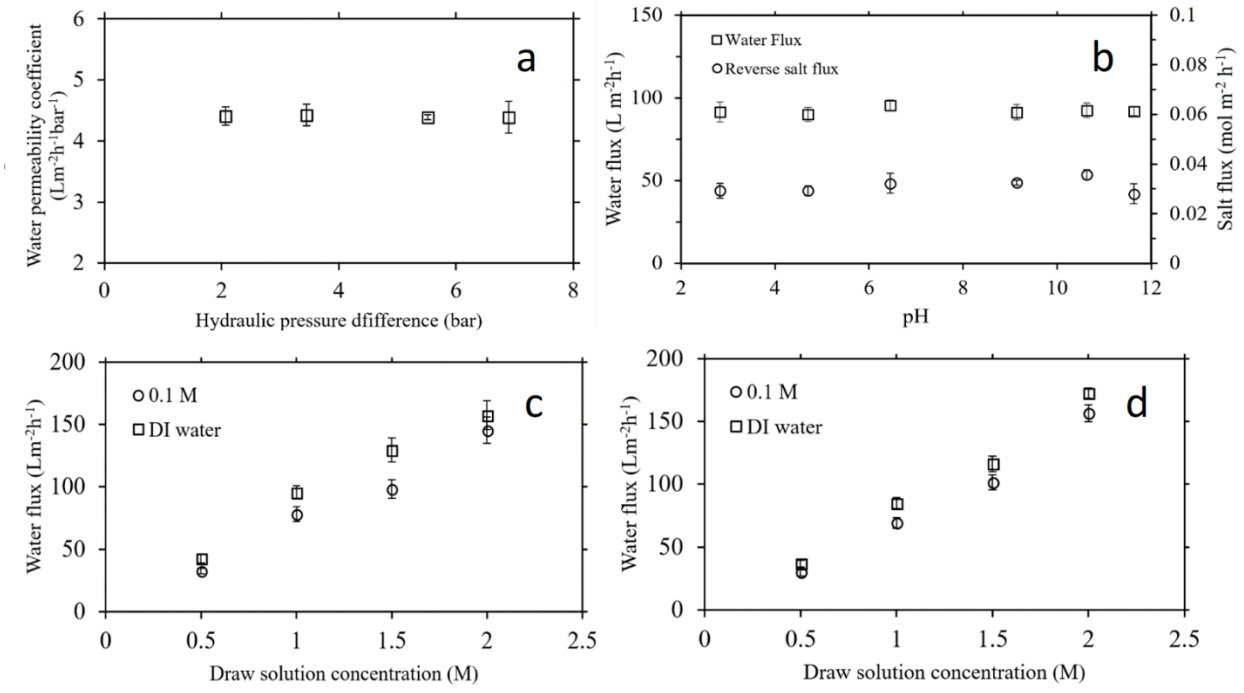

Figure 28 - (a) Water permeability coefficient of GOM under different hydraulic pressure differences, (b) water flux and salt flux change with the change of solution pH in FO system (1 M NaCl solution and DI water as draw and feed solutions, respectively), (c) water flux as a function of draw solution (NaCl) concentration in the FO system by using DI water or 0.1 M of NaCl as feed solution, and (d) water flux as a function of draw solution (NH_4HCO_3) concentration in the FO system by using DI water or 0.1 M of NH_4HCO_3 as a feed solution. Error bars are ±1 standard deviation.

6.4.3. Projected power density and energy efficiency in the osmotic heat engine

The electricity generation part of the osmotic heat engine determines how much electricity can be generated from the system. Power density in terms of unit membrane area is calculated based on the membrane water flux and the draw solution hydraulic pressure. Since the freestanding GOM does not have a support layer, and the water flux is almost proportional with the draw solution concentration (Figure 28c and d), the membrane ICP is neglected during the power density calculation. The membrane structural parameter (*S*) is used to quantify the influence of ICP on water flux and power density;[207] thus, the structural parameter is assumed to be zero in this study.

According to our calculation (using Eq (2) and (3)) as well as previous studies, the power density (W) increases with the increase of the applied hydraulic pressure on the draw solution side[6, 127]. When the hydraulic pressure is approximately half of the osmotic pressure difference between feed and draw solutions, peak power density is achieved (Figure 48). Fig 26a lists the calculated peak power density values from the different NH_4HCO_3 draw solutions (feed solution is DI water). As draw solution concentration increases from 0.5 M to 2 M, the peak power density increases from 7.3 W/m^2 to 56.3 W/m^2. Since the determined burst pressure is between 6.90 and 8.97 bar, the GOM in its current state cannot withstand half the osmotic pressure differences. The corresponding power density values were calculated for each hydraulic pressure below the burst pressure. As shown in Figure 29b, the power density increases with the increase of the hydraulic pressure on the draw solution side. Under a hydraulic pressure of 6.90 bar, the membrane power density reaches 6.7 W/m^2, 12.8 W/m^2, 16.9 W/m^2 and 20.0 W/m^2 when the NH_4HCO_3 draw solution concentrations are 0.5 M, 1 M, 1.5 M and 2 M, respectively. The

power density values, when considering the burst pressure, are lower than the peak values; however, they are higher than the power densities from previous studies under similar conditions[185, 189, 190, 208].

Energy efficiency measures the ratio of the thermal energy that can be converted into electricity. By assuming the temperature of the heat source is as low as 50 °C, an energy efficiency analysis on the osmotic heat engine that incorporates the GOM was conducted. It should be noted that according to our developed model (Appendix D.1), the energy efficiency is not influenced by the scale of the system. Instead, the system energy efficiency was found to increase with the increase of applied hydraulic pressure on the draw solution side (Figure 48). When the applied hydraulic pressure equals the osmotic pressure difference between the feed and draw solutions, the system energy efficiency reaches its highest value (around 5%), even though the power density is almost zero under such hydraulic pressure. When peak power density is reached (the hydraulic pressure is half the osmotic pressure difference), the osmotic heat engine achieves an energy efficiency of 2.48% (Figure 29c). The estimated optimal energy efficiency does not change with the draw solution concentration. When the draw solution of higher salt concentration is utilized, higher peak power density can be achieved, which is beneficial to energy generation. However, more thermal energy is needed to regenerate the feed and draw solutions when the draw solution concentration is higher, making the overall energy efficiency unchanged. The applied hydraulic pressure was found to have a significant influence on the energy efficiency: when the hydraulic pressure increases, the energy efficiency also increases (Figure 29d). For example, when the hydraulic pressure increases from 2.07 bar to 6.90 bar, the energy efficiency increases from 0.41%, 0.21%, 0.14% and

0.10% to 1.38%, 0.69%, 0.46% and 0.35% with the draw solution concentration of 0.5 M, 1 M, 1.5 M and 2 M, respectively. Although the system energy efficiency keeps increasing with the increase of the applied hydraulic pressure, the power density decreases when the applied hydraulic pressure is larger than half the osmotic pressure difference. At the same hydraulic pressure, lower draw solution concentration leads to higher energy efficiency because when the draw solution concentration is lower, less energy is needed to regenerate the feed and draw solutions.

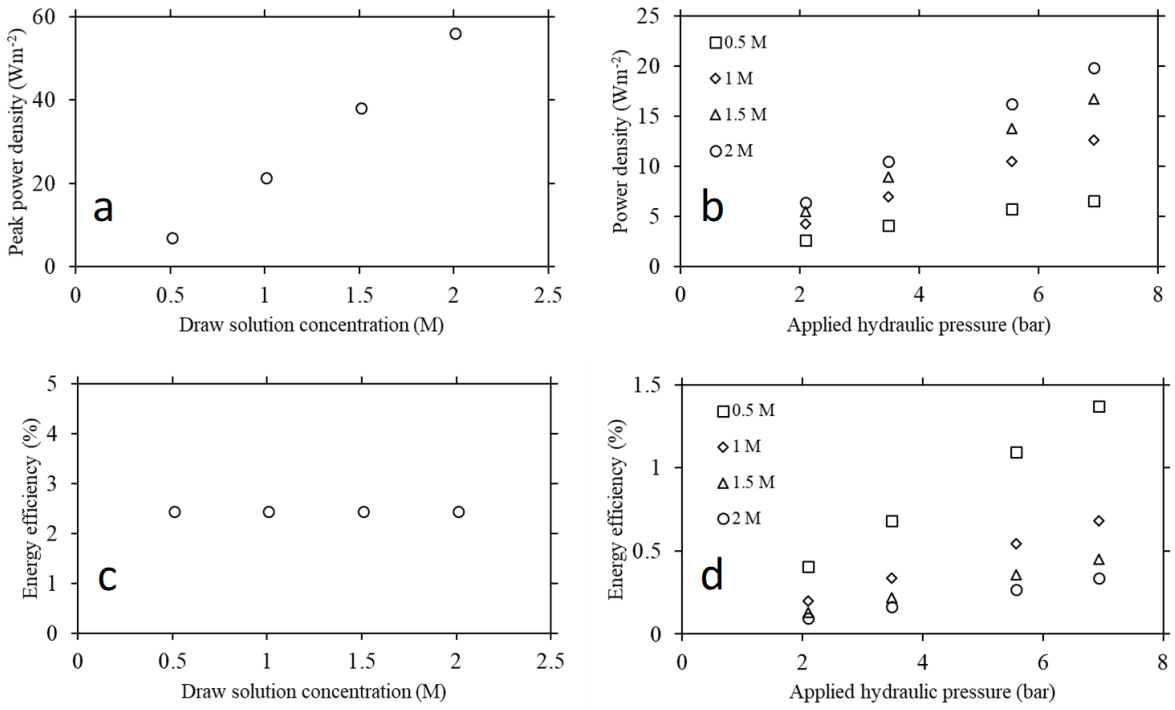

Figure 29 - Power generation of the GOM. (a) Peak power density values of the GOM with different draw solution concentrations. (b) Power density values of the GOM under different applied hydraulic pressures. (c) Energy efficiency values with different draw solution concentrations when peak power density is achieved. (d) Energy efficiency values of the GOM under different applied hydraulic pressures.

The osmotic heat engine outperforms existing technologies in terms of the feasible temperature. The system can generate electricity from heat sources of very low temperature as long as the solutes can be dissociated. According to previous studies, the NH_4HCO_3 solution can be ideally regenerated at a temperature of about 50 °C[189]. In this study, the membrane ICP is largely reduced by using the freestanding GOM. The reduction of

membrane ICP can significantly increase the effective driving force across the membrane. For commercial TFC membrane, high water flux and high power density can be achieved when DI water is used as the feed solution in the PRO system since there is no ICP in this situation[6]. However, it is a daunting task to eliminate all the solvent from the feed solution during the thermal separation process. When solvent residues retain in the feed solution, severe ICP will occur and water flux and power density will significantly decrease for TFC membranes. However, by using the freestanding GOM, a high water flux can still be achieved even when the feed solution contains a high concentration of salt (Figure 28c and d).

The results from this study show that when the applied hydraulic pressure is lower than half the osmotic pressure difference, both the power density and energy efficiency increase with the increase of the applied hydraulic pressure. However, the burst pressure of the GOM became the limiting factor for energy generation. The freestanding GOM in its current state can only resist about 6.90 bar of hydraulic pressure in the PRO system. The mechanical strength, and thus the burst pressure, might be increased by increasing the GOM thickness. However, when the GOM thickness increases, the water permeability coefficient will decrease, which would hinder the energy generation in the osmotic heat engine. In addition, the low stability of the GOM in water has been singled out as a key factor that has prevented the GOM from being applied on a large scale. It is quite possible that the low stability of GOM in water and the low burst pressure are related. Although GOMs were reported to have good mechanical properties in their dry state[170], the swelling of GOM upon hydration (indicated by the XRD result in this study) can decrease its stability, and thus the mechanical properties. Fortunately, many recent studies have

focused on increasing the stability and mechanical properties of the GO-related membranes[169, 209, 210]. The current study explores the suitability of freestanding GOMs in the osmotic heat engine for low-grade waste heat harvesting. Our efforts to develop GOMs with good transport properties as well as stability (in water) are essential to the success and further enhancement of system performance.

6.5. Conclusion

In summary, we have synthesized and investigated the performance of a freestanding GOM in the membrane-based osmotic heat engine. The water and ion transport properties of the freestanding GOM have been investigated. The GOM has an average water permeability coefficient of 4.4 LMH-bar. Due to the elimination of the membrane support layer, the ICP is largely minimized in the osmosis system. The GOM can achieve high power density in the osmotic heat engine using ammonium bicarbonate solution as the working fluid. Under an applied hydraulic pressure of 6.90 bar, the membrane power density reaches 6.7 W/m^2, 12.8 W/m^2, 16.9 W/m^2 and 20.0 W/m^2 when the draw solution concentration is 0.5 M, 1 M, 1.5 M and 2 M, respectively. The system energy efficiency was found to increase with the increase of applied hydraulic pressure. The current study concludes that the freestanding GOM is suitable for the application in the osmotic heat engine. However, future research on the development of GO-based membranes with higher burst pressure and better stability in water is needed to further advance this carbon neutral, transformative technology.

CHAPTER 7. MAJOR CONCLUSIONS AND FUTURE WORK

The major conclusions from this dissertation are:

1. RED-specific O-MWCNT nanocomposite CEMs were synthesized with different O-MWCNT loadings. The nanocomposite CEMs had better physiochemical properties (CD and SD) and electrochemical properties (IEC, permselectivity, and resistance) than the pristine polymeric CEM. Anti-fouling tests showed that the nanocomposite CEMs had better fouling resistant properties than the commercial CSO membrane. By incorporating O-MWCNTs, both membrane surface hydrophilicity and surface charge density increased. The enhancement of these surface properties might explain the enhancement of membrane anti-fouling properties. For energy generation in the RED system, the nanocomposite CEMs had higher power density than the commercial FKS membrane. Nanocomposite membranes were found to be attractive candidates for application in electrochemical systems like RED. By incorporating nanomaterials into polymer membranes, anti-fouling properties and energy generation in RED could be improved simultaneously.

2. Membrane micro-structure change and the influence on ion transport was explored for nanocomposite CEMs. A series of nanocomposite CEMs were synthesized by using SPPO as polymer material and silica NP (unsulfonated or sulfonated) as a nanomaterial. By analyzing the measured data with a computational model, we found that the membrane property change is closely related to the change of membrane micro-structure. With the adding of silica NPs, the interaction between the NP and the polymer chain leads to an increase of the membrane free volume (inter gel phase), allowing the

membrane to absorb more water upon hydration. Also, in the presence of NPs, the sulfonated polymer segments tend to expand, while the unsulfonated segments tend to depress. The increase of sulfonated polymer segments (pure gel phase) volume might explain the increase of membrane IEC. Generally, by the incorporation of nanomaterials, ion transport inside CEMs becomes more efficient. The results of this study can contribute to the value of future designs of new nanocomposite IEMs.

3. Ultrathin freestanding GOMs was synthesized and the performance in the PRO system was first evaluated. The freestanding GOMs showed moderate water permeability coefficient and excellent mechanical strength. Due to the elimination of the membrane support layer, the freestanding GOMs can mitigate internal concentration polarization during the PRO process. Although the GOMs showed high salt permeability coefficient when hydraulic pressure is applied to the draw solution side, high water flux and high power density were obtained. Furthermore, higher power density can be achieved by designing GOMs with better mechanical strength and higher water permeability coefficient. In general, the current study initiates a new way of designing PRO membranes and represents a step forward towards the application of the PRO for sustainable energy generation.

4. The freestanding GOM was investigated in membrane-based osmotic heat engine in terms of energy harvesting ability. The GOM can achieve high power density in the osmotic heat engine using ammonium bicarbonate solution as the working fluid. The system energy efficiency was found to increase with the increase of applied hydraulic pressure. The study concludes that the freestanding GOM is suitable for the application in the osmotic heat engine. However, future research on the development of GO-based

membranes with higher burst pressure and better stability in water is needed to further advance this carbon neutral, transformative technology.

Based on the conclusions from this dissertation, future works on the further advance of the technologies to harvest energy may include:

(1) Design of new types of nanocomposite ion exchange membranes with better energy generation performance in the RED system. Based on our analysis, nanomaterials can have a significant influence on the membrane properties since the micro-scale structure of the membrane can be influenceed by the nanomaterials. As diverse nanomaterials and more innovative synthesizing methods are developed, the nanocomposite membranes are expected to play more important roles in enhancing the performance of systems like RED and further diminish the membrane fouling problem.

(2) The development of more robust freestanding membranes for the application osmotic-driven processes. The freestanding membranes have great potential in osmotic-driven processes like PRO and FO since they can largely minimize internal concentration polarization and increase driving force across the membrane. However, since the freestanding membranes are ultrathin and act as an active layer, the osmotic and hydraulic pressures in the membrane system may destroy the membrane structural integrity easily. The development of robust freestanding membranes which can resist the pressures thus will evolutionally increase the efficiency of the osmotic-driven processes including PRO, FO, and osmotic heat engine. For the freestanding GOM, the relatively poor stability in water can reduce its mechanical property in the working state

(in an aqueous environment). A more robust GOM with higher burst pressure thus can be achieved by increasing the membrane stability in water. Adding cross-linkers inside the GO layers is an effective way to decrease swelling in water. Also, composite membranes synthesized by using GO and other organic/inorganic might also be effective. A freestanding membrane (with only an active layer) may also be designed by using other 2-dimensional nanomaterials or robust polymeric materials.

APPENDIX A. SUPPORTING INFORMATION FOR CHAPTER 3

A.1 Detailed description of the characterization of CEMs

A.1.1 Swelling Degree

The swelling degree (SD) refers to the wet membrane water content. The membrane SD was characterized by the weight difference between the dried and wet membrane. First, the membrane sample was immersed in DI water for 24 h. Then the wet membrane sample was weighted immediately after mopping with filter paper to remove surface water. The wet membrane sample was dried in the oven at 50 °C until a constant weight was obtained. The SD was calculated in wt % by the following equation:

$$SD = \frac{W_{wet} - W_{dry}}{W_{dry}} \times 100\% \quad (18)$$

where W_{wet} and W_{dry} are the mass (g) of wet and dried membrane samples, respectively.

A.1.2 Ion exchange capacity

Ion exchange capacity (IEC) is the number of charged functional groups per unit weight of the dried membrane. IEC of membranes was determined by titration. The membrane sample was first immersed in 1 M of HCl for 16 h. After rinsed with DI water, the sample was then immersed into 1 M of NaCl for another 6 h to undergo ion exchange (i.e., the replacement of proton by Na+). The resulting NaCl solution containing released protons was then titrated with 0.01 M of NaOH by using phenolphthalein as an indicator. The IEC of the membrane was calculated by the following equation:

$$IEC = \frac{C_{NaOH} \times V_{NaOH}}{W_{dry}} \quad (19)$$

where C_{NaOH} is the concentration of NaOH (M) used, and V_{NaOH} is the volume of NaOH.

A.1.3 Fixed charge density

Fixed charge density (CD), expressed in the number (mmol) of fixed charge groups per mass (g) of water in the membrane, was determined by the IEC over the SD of the membrane:

$$C_{fix} = \frac{IEC}{SD} \tag{20}$$

where C_{fix} is the fixed charge density (meq/g H_2O) of the membrane.

A.1.4 Ionic resistance

The membrane ionic resistance was measured by using a four-compartment cell made from Plexiglas. Totally three IEMs were set in the four compartments. The membrane in the center of the set-up was the membrane under investigation; the other two membranes were FKS (Fumasep®, Fumatech, Germany) commercial CEMs. All the membranes had an effective area of 7.91 cm^2. The two inner compartments were pumped with 0.5 M of NaCl solution; the outer compartments (electrode compartments) contained 0.5 M of Na_2SO_4 solution. Two titanium electrodes covered by platinum were used. The solutions were pumped by using two peristaltic pumps (Cole-Parmer, USA). A power supply was connected to the two electrodes. The voltage drop across the membrane was recorded for the applied current density. The measured resistance was obtained by the slope of current density versus the potential drop. Then the membrane ionic resistance was determined by subtracting the measured blank resistance (without membrane) from the measured membrane resistance.

A.1.5 Permselectivity

The permselectivity of the ion exchange membrane is an indicator of the ability to discriminate the cation from the anion. The apparent permselectivity (α) of the cation exchange membrane was measured by using a static potential method. A two-compartment cell was used, and the test membrane was placed to separate the two compartments with an effective area of 4.8 cm^2. 0.1 M and 0.5 M of NaCl solutions were used to fill the two compartments. Two Ag/AgCl reference electrodes (Hanna Instruments, USA) were applied to measure the potential difference across the membrane. In order to minimize the

effect of the diffusion boundary layer on the measurement, the aqueous solutions in both compartments were vigorously stirred by using magnetic stir bars. The apparent permselectivity was then determined by the ratio of the measured potential ($\Delta V_{measured}$) over the theoretical potential ($\Delta V_{theoretical}$), as shown in the following equation:

$$\alpha(\%) = \frac{\Delta V_{measured}}{\Delta V_{theoretical}} \times 100\% \quad (21)$$

where α is the apparent membrane permselectivity (%), and $\Delta V_{measured}$ and $\Delta V_{theoretical}$ are the measured and theoretical membrane potentials (mV), respectively. The theoretical membrane potential, which is the potential for an ideal membrane with 100% permselectivity, was calculated to be 37.9 mV by using the Nernst equation.

A.2 Surface AFM images of synthesized nanocomposite CEMs

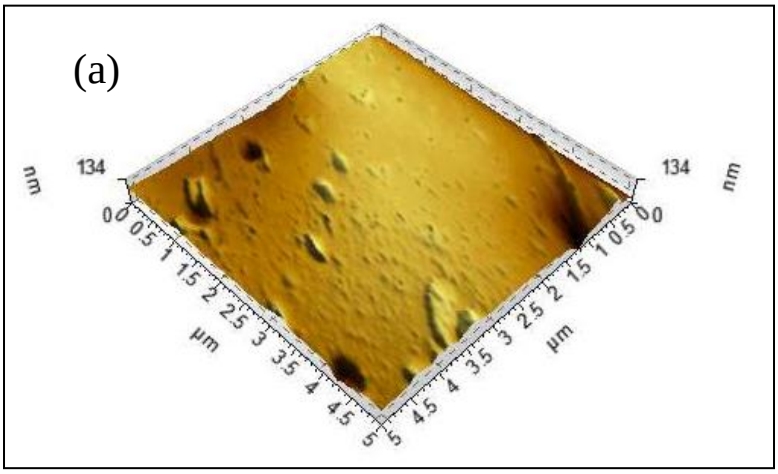

Figure 30 - Surface AFM images of nanocomposite membranes: (a) pristine SPPO membrane, (b) composite 0.1 wt % O-MWCNT membrane, (c) composite 0.2 wt % O-MWCNT membrane, (d) composite 0.3 wt % O-MWCNT membrane, (e) composite 0.5 wt % O-MWCNT membrane, and (f) composite 0.8 wt % O-MWCNT membrane.

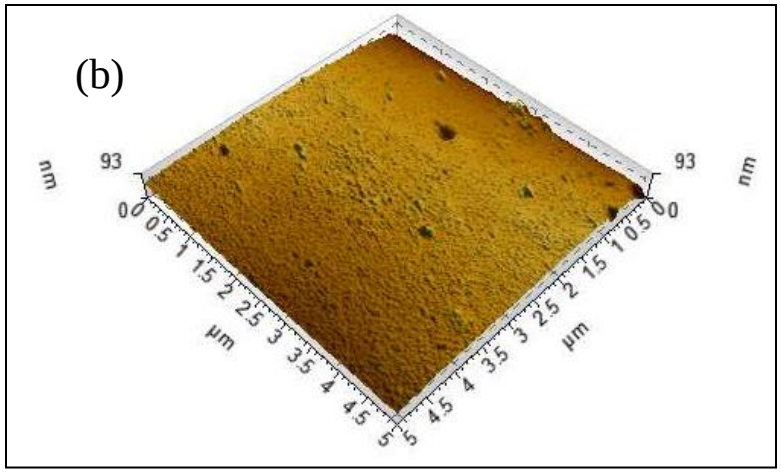

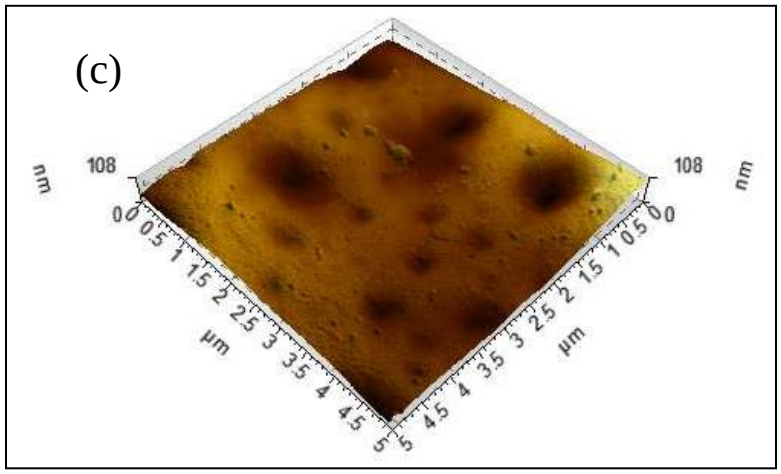

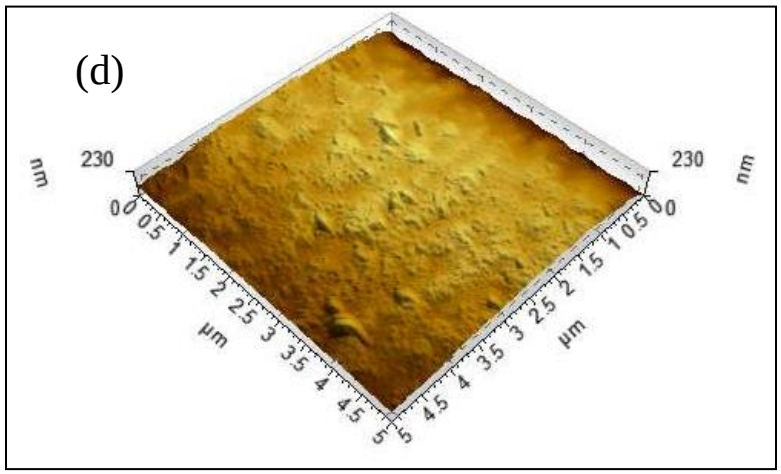

Figure 30 Continued.

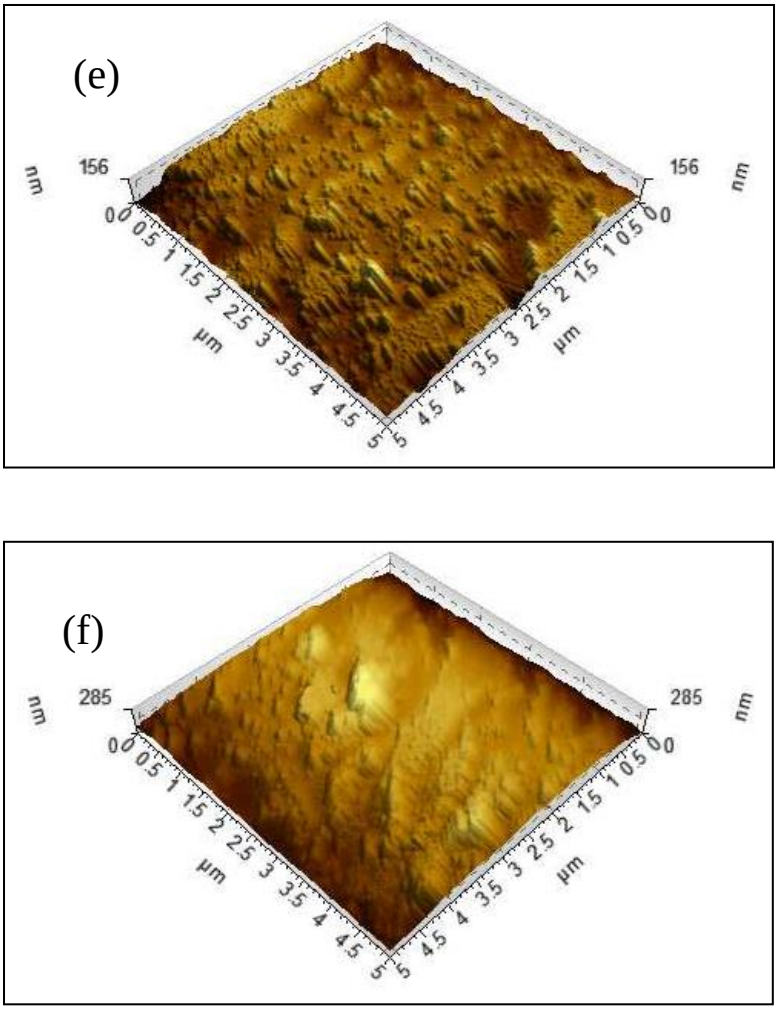

Figure 30 Continued.

A.3 Surface roughness parameters of synthesized nanocomposite CEMs

Table 8 - Complete surface roughness parameters of nanocomposite CEMs.

Membranes	S_a [nm]	S_q [nm]	S_z [nm]
SPPO	3.5	5.6	85.4
SPPO-0.1 O-MWCNT	7.0	9.0	93.6
SPPO-0.2 O-MWCNT	10.0	13.7	109.0
SPPO-0.3 O-MWCNT	14.6	18.8	157
SPPO-0.5 O-MWCNT	26.5	33.6	234
SPPO-0.8 O-MWCNT	36.7	45.7	289

Note: S_a, S_q, and S_z are mean roughness, root mean square of the Z data and mean difference between the highest peaks and lowest valleys, respectively.

A.4 List of the properties of all CEMs

Table 9 - Characteristics of CEMs.

Membranes	Thickness [μm]	IEC[a] [meq g dry^{-1}]	SD[b] [%]	CD[c] [meq g H_2O^{-1}]	Perm-selectivity [%]	Resistance [Ω cm^2]
SPPO	48	1.90	36.9	5.1	89.9	0.70
SPPO-0.1 O-MWCNT	47	2.12	38.6	5.5	90.0	0.60
SPPO-0.2 O-MWCNT	58	2.15	42.1	5.1	91.1	0.58
SPPO-0.3 O-MWCNT	61	2.20	42.6	5.2	91.7	0.51
SPPO-0.5 O-MWCNT	70	2.28	42.1	5.4	95.3	0.45
SPPO-0.8 O-MWCNT	62	1.78	38.9	4.6	91.2	0.62
SPPO-1.1 O-MWCNT	65	1.77	38.7	4.6	89.9	0.65
SPPO-1.5 O-MWCNT	69	1.77	37.6	4.7	90.8	0.67
CSO	100	1.04	16.0	6.5	94.7	2.26
FKS	50	1.40	22.0	6.4	98.3	1.87

[a] Ion exchange capacity.

[b] Swelling degree.

[c] Fixed charge density.

A.5 Potential (α^2/R) of IEMs

Nernst equation in the RED system:

$$P_{OCV} = \alpha \frac{NR_gT}{zF} ln(\frac{a_c}{a_d}) \quad (22)$$

where P_{OCV} is the open circuit voltage (OCV), α is the apparent membrane permselectivity, N is the total number of membranes, R_g is the gas constant (J/ mol·K), T is the temperature (K), z is the valence of the ions, F is the Faraday constant (96485 C/ mol), a_c and a_d are the activities of concentrated and diluted solutions (mol/ m^3), respectively.

Power density could be computed as:

$$P = \frac{{P_{OCV}}^2}{4R_{total}N} \quad (23)$$

where P is the power density (W/ m^2) of the RED system, and R_{total} is the total ionic resistance (Ω·cm^2) of the stack.

When combining the above two equations,

$$P = \frac{\alpha^2}{R_{total}} [\frac{R_gT}{2ZF} ln(\frac{a_c}{a_d})]^2 \quad (24)$$

When comparing different membranes, and keeping other factors (salinity gradient, electrodes, flow rate, intermembrane distance, etc.) the same, only apparent membrane permselectivity (α) and total ionic resistance (R_{total}) change in the equation. Thus, we can say that (α^2/R_{total}) is proportional to the power density of the RED system.

The total ionic resistance of the RED stack can be split into ohmic resistance and non-ohmic resistance. The non-ohmic resistance is generated by the change of the electromotive force during the process. For simplification, we assume that the non-ohmic resistance is constant for different membranes. Further, when only changing CEMs in the system, and keeping others (AEMs, spacers, and electrodes, etc.) the same, the total resistance (R_{total}) would be only influenced by the resistance of CEMs (R). The total resistance (R_{total}) and resistance of CEMs (R) should have a positive correlation. So

(α^2/R_{total}) and (α^2/R) also have a positive correlation. Thus, it is possible to predict and compare the power generation performance of different CEMs by assessing only (α^2/R). We call the term (α^2/R) the membrane performance potential. It is an intrinsic property and does not change with the environment.

A.6 Measured gross power density of CEMs

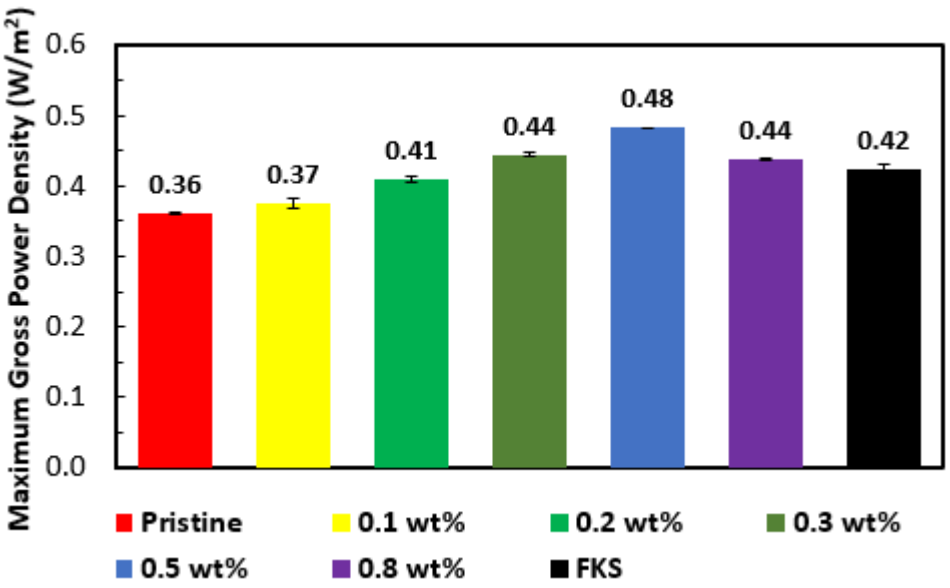

Figure 31 - Measured gross power density of CEMs.

APPENDIX B. SUPPORTING INFORMATION FOR CHAPTER 4

B.1 Chemical Reaction of Sulfonation of Silica NPs

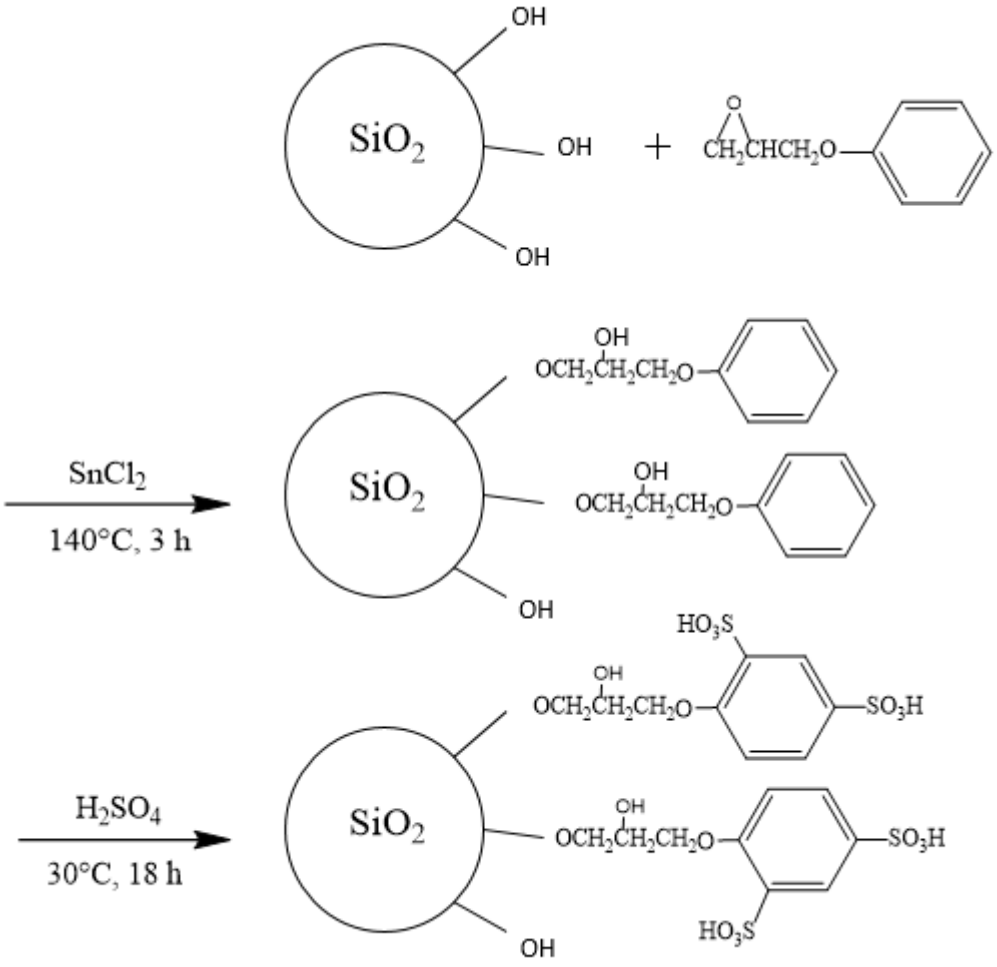

Figure 32 - Scheme of sulfonation reaction of silica NPs.

B.2 Molecular Weight of Sulfonated and Unsulfonated Silica NPs

Hydroxyl groups are attached to the surface of silica NPs. For the calculation of the molar weight of sulfonated silica NPs, first by assuming that all the hydroxyl groups are reacted, then

$$M_{silica\ NPs,sulfonated} = \frac{M_{silica} + M_{functional\ groups}}{1\ mol} \tag{25}$$

$$= \frac{60\text{g} + \left(\frac{0.82 \times 10^{-3}}{2} \times 325\right)\text{g}}{1\ \text{mol}}$$

$$= \frac{60\text{g} + 0.13\text{g}}{1\text{mol}}$$

$$\approx 60\text{g/mol}$$

Before the sulfonation reaction, all the functional groups were hydroxyl groups that attached on the NP surfaces.

$$M_{silica\ NPs,unfunctionalized} = \frac{M_{silica} + M_{hydroxyl\ groups}}{1\ mol} \tag{26}$$

$$= \frac{60\text{g} + \left(\frac{0.82 \times 10^{-3}}{2} \times 17\right)\text{g}}{1\ \text{mol}}$$

$$\approx 60\text{g/mol}$$

So, the molecular weight of silica NPs is almost unchanged during the sulfonation reaction. Thus, different silica NPs have different weight percentage as long as they have different molar numbers.

B.3 Characterization of IEMs

The membrane sample in the acid form (H^+) was immersed into 1 M of NaCl for 6 hours. The resulting NaCl solution containing released protons was then titrated with 0.01 M of NaOH solution by using phenolphthalein as an indicator. Then the membrane sample was immersed in DI water for one day. After that, the wet membrane sample was weighted immediately after mopping with filter paper. The membrane sample was then dried in the oven at 50 °C until a constant weight (as dry weight) was obtained. The membrane IEC and swelling degree (SD) were then calculated by:

$$IEC = \frac{C_{NaOH} \times V_{NaOH}}{W_{dry}} \tag{27}$$

$$SD = \frac{W_{wet} - W_{dry}}{W_{dry}} \times 100\% \tag{28}$$

where C_{NaOH} is the concentration (M) of NaOH solution used, V_{NaOH} is the volume (L) of the NaOH solution, and W_{wet} and W_{dry} are the mass (g) of wet and dried membrane samples, respectively. All the measurements were conducted for at least three times.

Membrane porosity was calculated by using measured membrane weight data [37]:

$$Porosity = \frac{W_{wet} - W_{dry}}{A\delta\rho_w} \times 100\% \tag{29}$$

where A is the area of the wet membrane sample, δ is the thickness of the wet membrane sample, and ρ_w is the density of water.

Membrane apparent permselectivity was determined by calculating the ratio of measured membrane potential and theoretical membrane potential derived from the Nernst equation. The membrane potential was measured by using a static potential method [35, 81]. The test membrane was set in between two cells with an open area of 4.8 cm^2. NaCl solutions of 0.5 M and 0.1 M were filled in the two cells, respectively. Two Ag/AgCl reference electrodes (Hanna Instruments, USA) were used two measure the potential difference across the membrane. The solutions in the two cells were vigorously stirred by using magnetic stir bars during the process, to minimize the diffusion boundary layer effect. The apparent permselectivity was then calculated by:

$$\alpha(\%) = \frac{\Delta V_{measured}}{\Delta V_{theoretical}} \times 100\% \quad (30)$$

Membrane ionic resistance was measured by using a four-compartment Plexiglas cell [35]. Totally three membranes were set inside the measuring system, the membrane in the center was the one under investigation, and the other two were commercial FKS (Fumasep®, Fumatech, Germany) CEMs. All membranes were stabilized and had an effective area of 7.9 cm^2. All four compartments were filled with 0.5 M of NaCl solution, with two outer compartments having an immobile solution, and two inner compartments having inflow and outflow. The water flows were managed by using two peristaltic pumps (Cole-Parmer, USA). Two titanium electrodes covered with platinum were placed at edges of the outer compartments and were connected to a power supply. Different current densities were applied, and corresponding potentials were recorded. The resistance was

obtained by the slope of current density versus the potential drop. The final membrane ionic resistance was calculated by subtracting the measured blank resistance (solution resistance) from the measured resistance.

B.4 AFM Phase Images of Membrane Surface

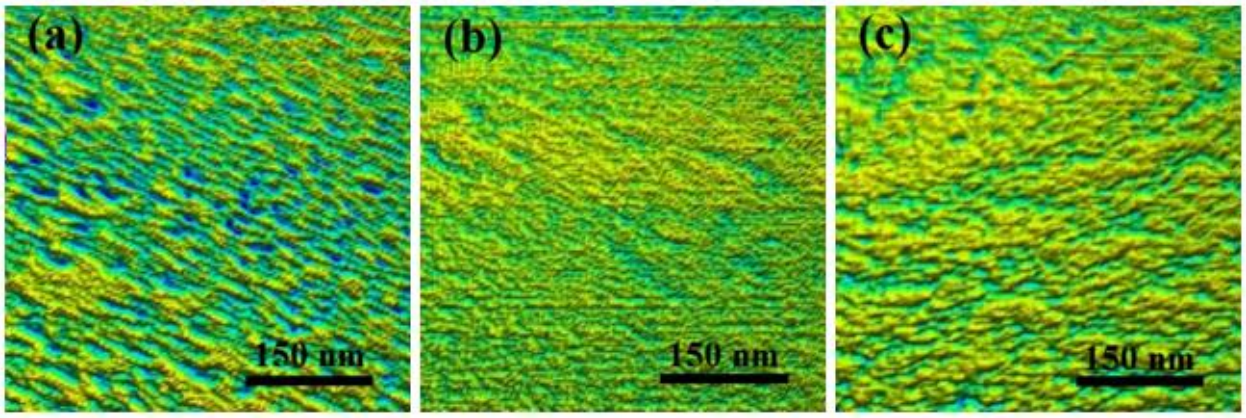

Figure 33 - AFM phase images of (a) membrane 1, (b) membrane 3a and (c) membrane 3b.

Tapping mode AFM phase images of membrane surface were obtained, on an area of 500 nm × 500 nm. Since the membrane surface roughness could influence the surface phase [106], only the regions with low morphological changes were recorded. Figure 33 shows the phase images of membranes 1, 3a and 3b. The lower domains indicate the soft and hydrophilic ionic clusters, and the higher domains correspond to the hard and

hydrophobic polymer backbone. Generally, the hydrophilic ionic clusters are responsible for ion transport, and the hydrophobic domains maintain the stiffness and stability of the membrane [111]. Figure 33 shows a nanophase separation morphology [106, 109], and some of the hydrophilic regions interconnect with each other to some degree. In literature, tapping mode AFM image has been extensively utilized to detect membrane microscale ion channels [108, 109, 111], and in many cases, the structural difference could be successfully distinguished for membranes with different microscale structures. Moreover, SEM or TEM images were also applied sometimes to characterize membrane microscale structures [110]. In this study, membrane 1 contains more lower domains than membrane 3a and membrane 3b.

The change of the small scale (500 nm × 500 nm) membrane morphology (phase images) might be due to the incorporation of nanomaterials; however, to get more detailed information of the membrane hydrophilic-hydrophobic domain relation and distribution, larger scale (50 μm × 50 μm) AFM phase images were obtained. Larger scale phase images contain more points; thus, they are more statistically significant. Furthermore, instead of categorizing the membrane domains into distinctly hydrophilic or hydrophobic, we classified different parts of membrane area according to the degree of stiffness by using Slice function in Pico Image software. At least six measurements were conducted for each sample. Figure 34 shows the large-scale phase images and stiffness distributions of all the membrane samples. The larger number of degrees, which results from larger water swelling on the hydration of the material, indicates the more hydrophilic nature of the material. Different degrees of stiffness represent by different colors in the phase images. It is obvious that with the addition of NPs, degree distribution shifts to the right, meaning that the

number of relatively hydrophilic domains as well as membrane mean surface hydrophilicity increased.

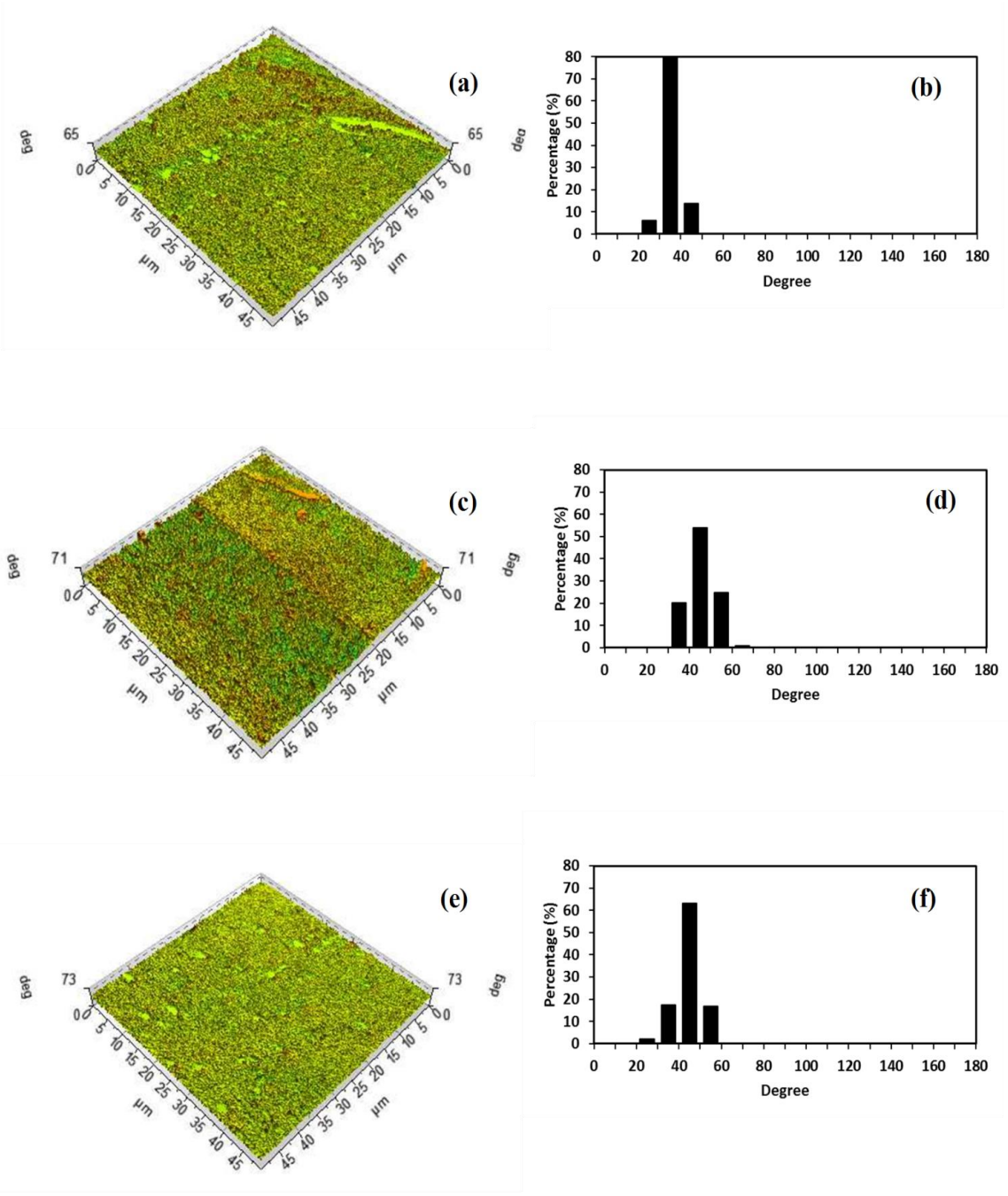

Figure 34 - Large scale (50 μm × 50 μm) phase images of (a) membrane 1, (c) membrane 2a, (e) membrane 2b, (g) membrane 3a, (i) membrane 3b, (k) membrane 4a, (m) membrane 4b, (o) membrane 5a, and (q) membrane 5b; areal phase (stiffness) distributions of (b) membrane 1, (d) membrane 2a, (f) membrane 2b, (h) membrane 3a, (j) membrane 3b, (l) membrane 4a, (n) membrane 4b, (p) membrane 5a, and (r) membrane 5b.

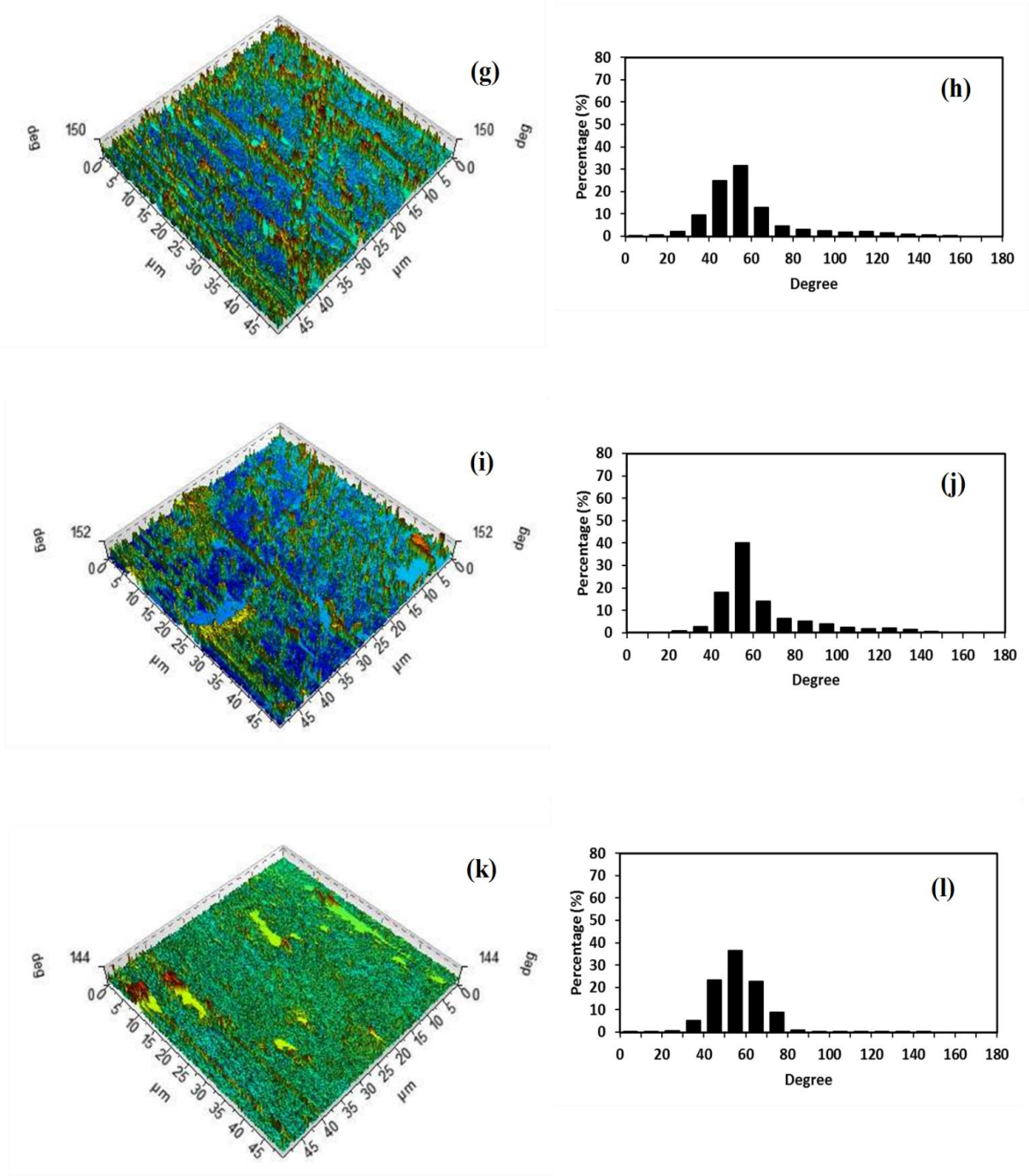

Figure 34 continued.

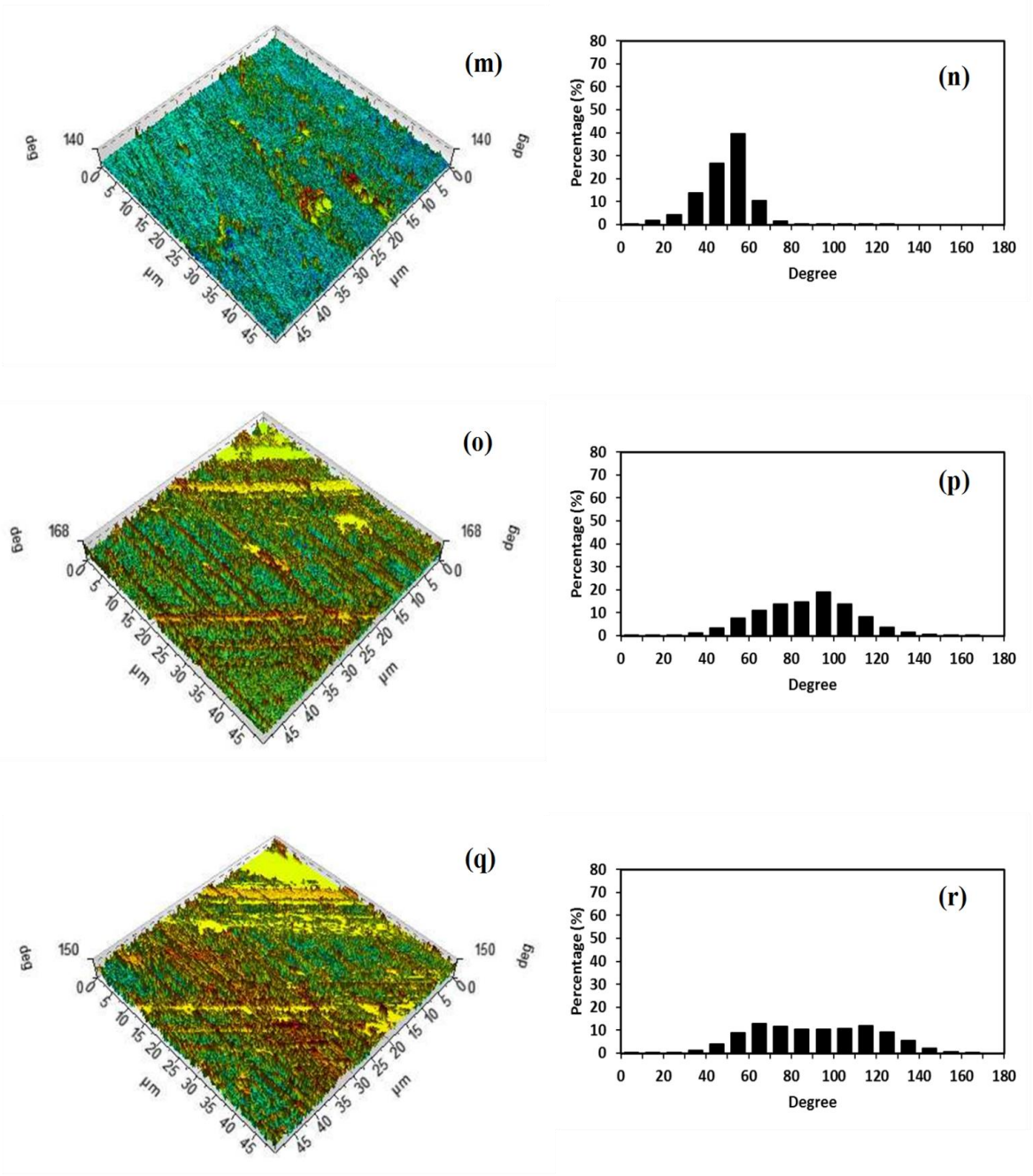

Figure 34 continued.

B.5 Additional SEM Image and EDX Results

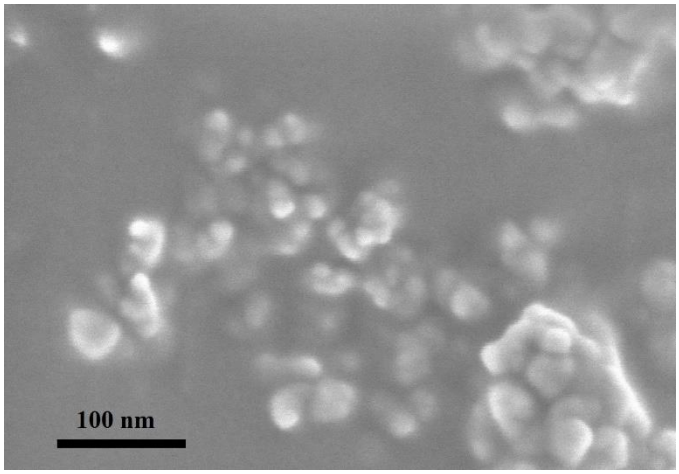

Figure 35 - SEM image of silica nanoparticles.

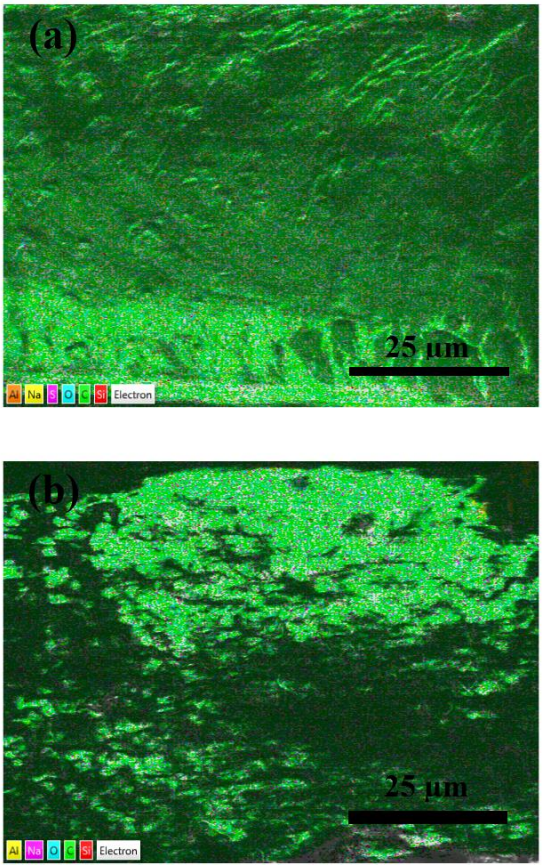

Figure 36 - Cross-sectional EDX images of (a) Membrane 5a, and (b) Membrane 5b.

Table 10 - Cross-sectional carbon and silicon elements weight percentages of selected membranes by EDX.

Membranes	C (wt%)	Si (wt%)
Membrane 3a	73.7	0.1
Membrane 3b	76.7	0.1
Membrane 5a	77.4	0.2
Membrane 5b	76.1	0.3

B.6 Membrane Ionic Resistance and Conductivity

Table 11 - Measured membrane ionic resistance (R) in different solution concentrations.

Membranes	Membrane ionic resistance [Ω cm^2] in different solution concentrations				
	0.01M	0.02M	0.05M	0.08M	0.1M
Membrane 1	16.81±0.56	13.49±0.46	7.92±0.33	5.69±0.18	4.81±0.26
Membrane 2a	16.29±0.35	12.97±0.39	7.19±0.46	5.11±0.25	4.17±0.17
Membrane 2b	16.22±0.29	12.63±0.48	7.48±0.25	5.35±0.27	4.12±0.39
Membrane 3a	16.39±0.75	12.78±0.64	7.27±0.19	5.39±0.19	4.17±0.34
Membrane 3b	16.24±1.16	12.83±0.29	7.37±0.36	5.21±0.46	4.22±0.29
Membrane 4a	15.92±0.09	12.18±0.46	6.77±0.43	4.83±0.43	3.62±0.11
Membrane 4b	16.03±0.26	12.24±0.75	6.94±0.26	4.68±0.27	3.67±0.03
Membrane 5a	16.34±0.46	12.72±0.81	7.35±0.41	5.26±0.61	4.25±0.15
Membrane 5b	16.28±0.49	12.64±0.40	7.38±0.18	5.32±0.24	4.18±0.27

Table 12 - Calculated membrane conductivity (k_m) in different solution concentrations.

Membranes	Membrane conductivity [μS cm^{-1}] in different solution concentrations				
	0.01M	0.02M	0.05M	0.08M	0.1M
Membrane 1	464.0±15.0	578.2±19.1	984.9±39.4	1370.8±42.0	1621.6±83.2
Membrane 2a	570.9±12.0	717.0±20.9	1293.5±77.8	1819.9±84.9	2230.2±87.4
Membrane 2b	579.5±10.2	744.3±27.2	1256.7±40.6	1757.0±84.4	2281.6±197.3
Membrane 3a	597.9±26.2	766.8±36.6	1348.0±34.3	1818.2±61.9	2350.1±177.2
Membrane 3b	603.5±40.2	763.8±16.9	1329.7±61.9	1881.0±152.6	2322.3±149.3
Membrane 4a	571.6±32.2	747.1±27.2	1344.2±80.3	1884.1±154.0	2513.8±74.1
Membrane 4b	555.2±8.9	727.1±42.0	1282.4±46.3	1901.7±103.7	2425.1±19.7
Membrane 5a	538.6±14.7	691.8±41.4	1197.3±63.3	1673.0±173.9	2070.6±70.6
Membrane 5b	595.8±17.4	767.4±23.5	1314.4±31.3	1823.3±78.7	2320.6±140.8

B.7 Degree of Sulfonation and Volume Fraction of Pure Gel Phase

The degree of sulfonation (DS) of polymers could be calculated by:

$$DS = \frac{IEC}{1000\times[\frac{(1-M_{SPPO}\times\frac{IEC}{1000})}{M_{PPO}}+\frac{IEC}{1000}]}\times 100\% \quad (31)$$

where M_{SPPO} is the molar weight (g/ mol) of sulfonated PPO, and M_{PPO} is the molar weight (g/ mol) of PPO. Theoretically, all the SPPO in this study should have the same DS, since all the PPO were sulfonated from the same batch. However, it is obvious that the addition of NPs increased the IEC of membranes, thus we rationalized the fact by assuming that the NPs change the DS of membrane polymeric material. So that different membranes could be treated as they were synthesized by using polymeric materials of different DS.

By assuming that all the monomers, whether sulfonated or not, occupy the same volume in the matrices, volume fraction of pure gel phase (f_{11}) could be obtained as the product of DS and polymer gel phase (f_1), and the rest of the gel phase is occupied by inert polymer phase (f_{12}):

$$f_{11} = DS \times f_1 \tag{32}$$

$$f_{12} = f_1 - f_{11} \tag{33}$$

Table 13 - Degree of sulfonation and different membrane gel phases.

Membranes	f_1 [%]	DS [%]	f_{11} [%]	f_{12} [%]
Membrane 1	44.8	30.9	13.8	31.0
Membrane 2a	40.1	33.7	13.5	26.6
Membrane 2b	41.6	33.7	14.0	27.6
Membrane 3a	41.2	33.4	13.8	27.4
Membrane 3b	41.2	34.0	14.0	27.2
Membrane 4a	36.8	37.4	13.8	23.0
Membrane 4b	36.4	37.0	13.5	22.9
Membrane 5a	41.5	32.2	13.4	28.1
Membrane 5b	41.6	32.5	13.5	28.1

B.8 Measured Porosity of Membranes

Membrane porosity was calculated by using the method in B.3. Porosity of all the synthesized membranes (wet state) is listed in Table 14. Standard deviations are not included.

Table 14 - Porosity of synthesized membranes.

Membranes	Porosity [%]
Membrane 1	55.4±3.6
Membrane 2a	57.8±5.7
Membrane 2b	57.0±2.6
Membrane 3a	59.1±4.3
Membrane 3b	58.5±6.2
Membrane 4a	65.7±1.7
Membrane 4b	62.2±4.7
Membrane 5a	55.6±5.9
Membrane 5b	58.8±4.7

B.9 Effective Ion Diffusion Coefficient and Tortuosity of Additional CEMs

SPPO based functionalized iron oxide [37] nanocomposite CEMs were discussed. Effective ion diffusion coefficient (presented as D_{eff}/ D) and tortuosity factor (τ) of all the CEMs were calculated. Membrane porosity data was used as the volume fraction of electrolyte solution phase in membrane, since they have the same physical meaning, and their values were attested to be approximately the same for nanocomposite silica NP CEMs. For iron oxide nanocomposite CEMs, porosity data was taken from the reference [37]. Membrane ionic resistance in 0.5 M of sodium chloride solution was used to calculate the membrane molar conductivity. For iron oxide nanocomposite CEMs, only membranes with thickness of 100 μm and 40 min of evaporation time were included in the discussion. More detailed information about the nanocomposite CEMs could be found in the corresponding references.

Table 15 - Porosity of additional nanocomposite CEMs.

Membranes	Porosity [%]
0-100 T	47.0
0.3-100 T	52.0
0.7-100 T	56.0

Table 16 - Effective diffusion coefficient of additional nanocomposite CEMs.

Membranes	D_{eff}/D
0-100 T	0.020
0.3-100 T	0.039
0.7-100 T	0.042

Table 17 - Tortuosity factor of additional nanocomposite CEMs.

Membranes	τ
0-100 T	23.62
0.3-100 T	13.39
0.7-100 T	13.30

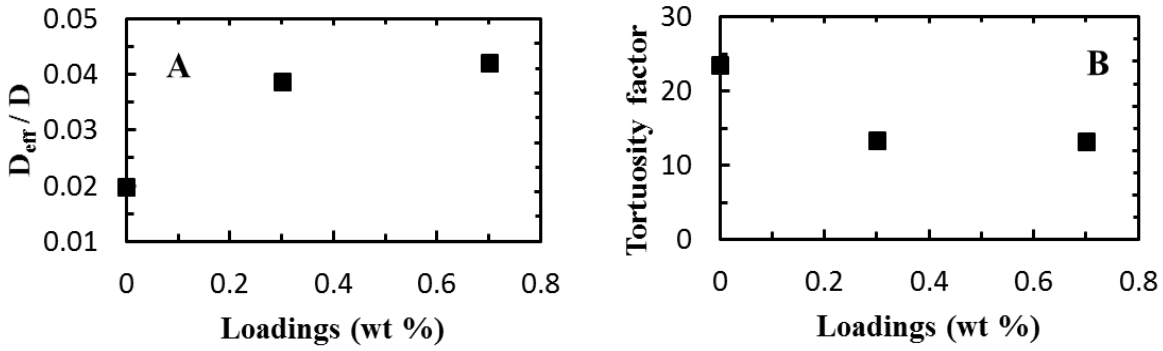

Figure 37 - Additional list of diffusion coefficient ratio and tortuosity of discussed CEMs. (A) D_{eff}/ D and (B) Tortuosity factor of CEMs with iron oxide (only membranes with a thickness of 100 µm are shown; standard deviations are not included since they are not shown in the corresponding reference).

B.10 Simulation of Nanoparticle Aggregation in Casting Solution

The concentration of nanoparticles added to the casting solution needs to be estimated before compared to the diffusivity. For large spherical nanoparticles, it can be assumed that the volume of the particle (V_p) is the overall volume of the basic unit (V_{unit}).

$$V_p = NV_{unit} \tag{34}$$

The number of basic unit in a particle is denoted N. If the diameter of nanoparticles (D_p) is deduced from TEM images, then, the estimation of unit diameter (D_{unit}) is possible as we have:

$$D_p = N^{1/3} D_{unit} \tag{35}$$

Therefore, the number of units (molecules) N in a nanoparticle is [211]:

$$N = \left(\frac{D_p}{D_{unit}} \right)^3 \tag{36}$$

For silica and iron oxide nanoparticles, the mole weight is summarized in Table 18.

Table 18 - Data of corresponding nanoparticles.

Nanoparticles	Diameter (nm) of a single unit	Molar weight (g/ mol) of a single unit	Molar weight of single nanoparticles	Reference
SiO_2 (17 nm)	0.342	60	4.05E+7	This study
SiO_2 (30 nm)	0.342	60	7.37E+6	[117]
SiO_2 (420 nm)	0.342	60	1.11E+11	[113]
SiO_2 (30 nm)	0.342	60	7.37E+6	[41]
Fe_2O_3 (30 nm)	0.830	160	7.56E+6	[37]

Model development:

Assumedly, the effective diffusivity is determined by the number concentration of nanoparticles incorporated into the polymer structure and the size of the nanocomposite structure:

$$D_{eff} = a + b \cdot \rho_n \tag{37}$$

The number concentration of nanomaterial groups, ρ_n, is calculated as the nanomaterial numbers in a given volume; a and b here are fitting constants for linear regression. To obtain the number of nanoparticle groups after the aggregation of individual particles, we also need to know the resulted number of groups given the number of nanoparticles we introduce to the casting solution. The characteristic relationship between the amount of nanoparticle added and the effective diffusivity can be simulated by a statistical model considering the aggregation of nanoparticles in the casting solution matrices.

The model assumes that at the micro-scale, van der Waals force is the dominating form of interactions between nanoparticles [212, 213]. The interaction energies between two similar particles can be calculated using van der Waals energy equation from DLVO theory expressed as:

$$V_A = -\frac{A a_1 a_2}{12h(a_1 + a_2)(1 + 11.12h/\lambda_c)} \tag{38}$$

where a_1 and a_2 are the radius of two nanoparticles, A is the Hamaker constant, nonetheless different from the value used in common aqueous environment. However, the constant is equivalently adjusted as the threshold energy is fit to experimental data as explained in the

following; h is the distance between two surfaces of particles, λ_c is the character wavelength (taken as 100 nm generally) [10]. By applying the model, we can get the pairwise binding energy of every two particles, assuming only two-body interactions. Because of the high viscosity of casting solution, the nanoparticle groups would be stable after formation, especially considering the membrane forming after casting of blend solution on a glass plate surface. Therefore, formed groups will not dissociate into single particles. An energy threshold value has been chosen as a cutoff because the aggregation can only progress within a limited time before solvent evaporation which leads to the drying-out.

Algorithm:

The input of the model is the added particle numbers; the output is the resulted number concentration of nanomaterial groups and fit to a linear model to D_{eff}/D. The program is coded in Matlab (2016b, education edition, MathWorks®). A certain number of particles are initialized randomly with radius and position coordinates in 3-D space. For each pair of particles, the van der Waals energy is calculated and the inverse of these values are saved as matrix *A*. *A* is then used in the agglomerative hieratical clustering algorithm with a threshold as the implementation of energy cut-off, and 'average' method was used for clustering [214]. The resulted group numbers can be obtained by counting cluster numbers given the threshold.

The added particle values are varied and at each value, 50 replicates are recorded. The results are shown in Figure 38 indicating the simulation in 1 μm^3 space with initial particles ranging from 0 to 2500. The particle diameter is normally distributed with a mean

of 20 nm and a standard deviation of 1 nm. Fitted values are obtained by minimize the root mean square error of averaged simulated values with respect to experimental data. Energy threshold and fitting constants are summarized in Table 19.

Table 19 - Parameters of corresponding nanoparticles.

Nanoparticles	*a*	*b*	Energy threshold (J)	Reference
Silica NPs (unsolfonated)	0.233	0.0117	2.86E-24	This study
Silica NPs (solfonated)	0.227	0.0134	2.63E-24	This study
Iron oxide (100 µm)	0.200	0.0083	1.00E-23	[37]
Silica NPs (30 µm)	0.451	0.0119	1.12E-23	[117]
Silica NPs (30 µm)	0.579	0.0074	5.05E-23	[41]
Silica NPs (420 µm)	0.550	0.0042	3.61E-24	[113]

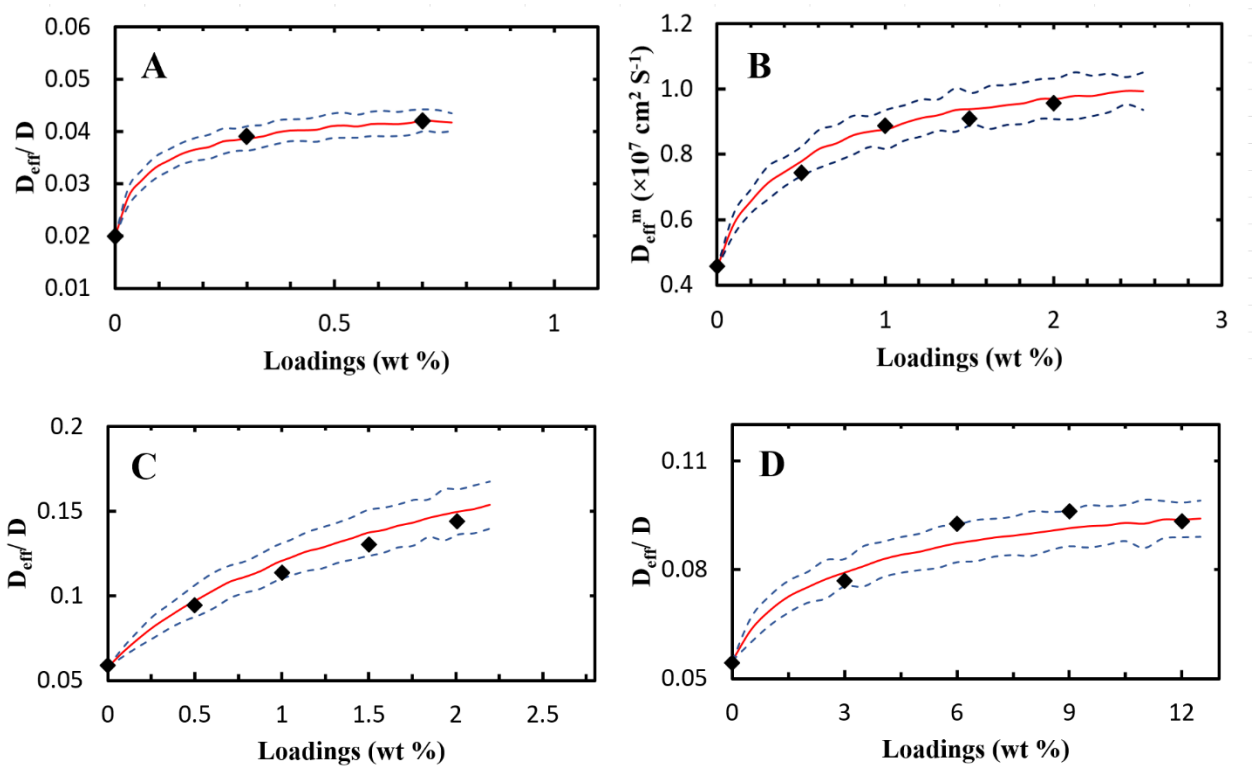

Figure 38 - (A) D_{eff}/D of sulfonated iron oxide based, (B) D_{eff}^{m} of silica (30 nm) based (C) D_{eff}/D of silica (30 nm) +based, and (D) D_{eff}/D of silica (420 nm) based nanocomposite IEMs as function of loadings (black dots are the experimental results, red lines are the average values of simulation, and blue dash lines are two standard deviations ($\mu \pm 2\sigma$)).

B.11 Matlab Codes of Simulation Model

binding_energy.m

```
function energy = binding_energy(single, whole)


% taking as arguments a 1-by-N vector <single> containing a single
observation

% from points, an M2-by-N matrix <whole> containing multiple observations
from

% points, and returning an M2-by-1 vector of distances D2, whose Jth

% element is the force between the observations single and whole(J,:).


%% The following calculation citing Abu-Lail et al. 2003 and Schenkel et
al.

% 1960 in Supporting Information


% Hamaker coefficient

A = 1E-20;

% distance between centers of spheres

dist = pdist2(single(2:end), whole(:, 2:end));


% inter surface distance D = r - R1 - R2

D = dist' - single(1) - whole(:,1);

% avoid the negative value if two points are initilized closer than their
radius combined

D(D<0) = min(D(D>0));

energy = A * single(1)*whole(:,1)./(single(1)+whole(:,1)) ./ D ./ (1 +
11.12*D / 1E-7);
```

```
%}


end
```

plot_fitting.m

```
%% Author: Bopeng Zhang; December 30, 2016

% this script takes experimental data and tries to find the best fitting

% of energy threshold


clear variables;

% different weight content of nanoparticles tested in experiments; vary
for  % different nanomaterials as inputs

loading = [0, 0.005, 0.01, 0.015, 0.02];

% experimental data of effective diffusivity for different loadings

% vary for different nanomaterials as inputs

data = [0.4578, 0.7438, 0.8878, 0.9091, 0.9565];

% density of membrane in unit g/um^3. We are dealing with 1 um^3 of

% material only

rho_m = 1E-12;

% molar weight of 1 mol of nanoparticles in g/mol

W_n = 4.05E7;

% calculating number of nanoparticles originally added

Av = 6.02E23; % Avogadro number

np = floor(rho_m / W_n * Av * loading); % number of nanoparticles added

REP = 10; % replicate times of simulation

observed = zeros(length(np),REP);
```

```
threshold = 8.85E22; % initialize the inverse of threshold energy
RADIUM = 15e-9; % particle redius


old_SS = 10;
SSresid = 100;
i = 1;
step = 1;
while abs(old_SS-SSresid) > 1E-9
    old_SS = SSresid;
    for j = 1:REP
        i = 1;
        for number = np
            if number == 0
                observed(i, j) = 0;
            else
                % first data store radius of particle
                radius = normrnd(RADIUM, 1E-9, [number, 1]);
                radius(radius<0) = RADIUM;
                % random initialization in 1 um^3
                points = [radius 1E-6*rand([number,3])];
                % follow the clustering algorithm
                energy_distance = 1./pdist(points,@binding_energy);


                Z = linkage(energy_distance, 'average');
                T      =      cluster(Z,      'cutoff',      threshold,
'criterion','distance');
                % resulted group number is the groups number of clusters
                observed(i, j) = max(T);
```

```
            end
            i = i + 1;
        end

    end
    sim = mean(observed, 2);

    % fit a linear regression model and calculate sum of squared residuals
    p = polyfit(sim', data, 1);
    yfit = polyval(p, sim');
    yresid = data - yfit;
    SSresid = sum(yresid.^2);
    fprintf('This is run %d at the cut-off of %.2e; the SSresid is %.6f.\n', step, 1/threshold, SSresid);
    threshold = threshold + 1E21;
    step = step + 1;

end

plot(np, data);hold on; plot(np, yfit)
```

plot_fitting_line.m

```
%% Author: Bopeng Zhang; December 30, 2016
% this script takes the best energy threshold and generates the simulated
% diffusivity (or effective diffusivity)

clear variables;
% simulation on 25 points on x-axis
list = 1:25;
observed = zeros(50,length(list));
% fitting parameters a and b for linear regression; get from fitting.m
a = 0.451; b = 0.0124;
% replicate for 50 times
for j = 1:50
    for i = list
        NUMBER = i*15; THRESHOLD = 8.93E22; RADIUM = 15E-9;

        % first data store radius of particle; three coordinates later
        radius = normrnd(RADIUM, 1E-9, [NUMBER, 1]);
        radius(radius<0) = RADIUM;
        % random initialization in 1 um^3
        points = [radius 1E-6*rand([NUMBER,3])];

        energy_distance = 1./pdist(points,@binding_energy);

        Z = linkage(energy_distance, 'average');
        T = cluster(Z, 'cutoff', THRESHOLD, 'criterion','distance');
        observed(j,i) = max(T);
    end
```

```
    plot(list*15, a+b*observed(j,:),'.');
    hold on;
    display(j);
end


xlabel('Added particle number');
ylabel('Effective diffusivity/diffusivity');
```

APPENDIX C. SUPPORTING INFORMATION FOR CHAPTER 5

C.1 Derivation of Equation (14)

In a PRO system, for a conventional thin film composite (TFC) membrane (with support layer) (Figure 42a), when water molecules transport across the membrane, the salt ions in feed solution are rejected by the membrane active layer. The reflux of the retained ions is however hindered by the tortuous membrane support layer and a higher concentration of salt ions is found in the support layer. A locally concentrated boundary layer then builds up in the support layer, resulting in internal concentration polarization (ICP) [159]. At the same time, as water permeates from the feed solution side to the draw solution side, the concentrated draw solution side suffers from a dilutive effect, the permeated water molecules displace and push the salt ions away from the active layer surface [159]. Thus, the salt concentration near the membrane surface decreases dramatically, especially when the water flux is high. The phenomenon is referred to as dilutive external concentration polarization (ECP). In addition, the concentrative effect at the feed solution side deteriorates by the (reverse) salt flux. The salt ions transport from the draw solution side to the feed solution side, further increasing the concentration inside the support layer. The ICP, ECP and (reverse) salt flux all have a negative influence on the driving force. The effective osmotic pressure across the membrane active layer is thus [127]:

$$\pi_{D,m} - \pi_{F,m} = \left\{ \frac{\pi_{D,b} \exp\left(-\frac{J_W}{k}\right) - \pi_{F,b} \exp\left(\frac{J_W S}{D}\right)}{1 + \frac{B}{J_W}\left[\exp\left(\frac{J_W S}{D}\right) - \exp\left(-\frac{J_W}{k}\right)\right]} \right\} \quad (39)$$

where $\pi_{D,m}$ is the osmotic pressure at the membrane surface on the draw solution side, $\pi_{D,b}$ is the osmotic pressure of the bulk draw solute, $\pi_{F,m}$ is the osmotic pressure at the membrane surface on the feed solution side, $\pi_{F,b}$ is the osmotic pressure of the bulk feed solute, J_w is the water flux, J_S is the reverse solute flux, B is the solute permeability coefficient, S is the structural parameter, D is the diffusion coefficient of the draw solution, and k is the mass transfer coefficient of the boundary layer for NaCl (calculation procedure is shown in Appendix C.2).

Ideally, water flux equals the water permeability coefficient (A) times the effective pressure across the membrane:

$$J_W = A(\Delta\pi_m - \Delta P) \tag{40}$$

where $\Delta\pi_m$ is the effective osmotic pressure difference, and ΔP is the applied external hydraulic pressure across the membrane. The effective osmotic pressure difference ($\Delta\pi_m$) is the osmotic pressure difference across the membrane active layer ($\pi_{D,m}$-$\pi_{F,m}$). By combining eq (S1) and (S2), equ (14) in Chapter 5 can be obtained:

$$J_W = A\left\{\frac{\pi_{D,b}\exp\left(-\frac{J_W}{k}\right)-\pi_{F,b}\exp\left(\frac{J_W S}{D}\right)}{1+\frac{B}{J_W}\left[\exp\left(\frac{J_W S}{D}\right)-\exp\left(-\frac{J_W}{k}\right)\right]} - \Delta P\right\} \tag{14}$$

C.2 Determination of boundary layer mass transfer coefficient

To quantify the influence of CP on water flux and power density, the value of boundary layer mass transfer coefficient (k) needs to be determined. The value of k could be determined by using boundary layer film theory, which can be expressed as [159]:

$$k = \frac{Sh\ D}{d_h} \tag{41}$$

where *Sh* is the Sherwood number, *D* is the solute diffusion coefficient, and d_h is the hydraulic diameter (2ab/(a+b)). The Sherwood number needs to be calculated before the mass transfer coefficient could be determined [215]:

$$Sh = 1.85(ReSc\frac{d_h}{L})^{0.33} \qquad \text{(laminar flow)} \tag{42}$$

$$Sh = 0.04Re^{0.75}Sc^{0.33} \qquad \text{(turbulent flow)} \tag{43}$$

where *Re* is the Reynolds number, *Sc* is the Schmidt number, and *L* is the channel length. The values of the Reynolds number and the Schmidt number are needed to determine the type of flow and calculate the Sherwood number:

$$Re = \frac{\rho v d_h}{\mu} \tag{44}$$

$$Sc = \frac{\mu}{\rho D} \tag{45}$$

where ρ is the water density, *v* is the velocity above the boundary layer, and μ is the water viscosity. The calculated *Re* indicates the type of flow is laminar flow, so eq (42) was used to calculate the Sherwood number. The determined average value of *k* for the crossflow FO cell is 26.8 μm/s.

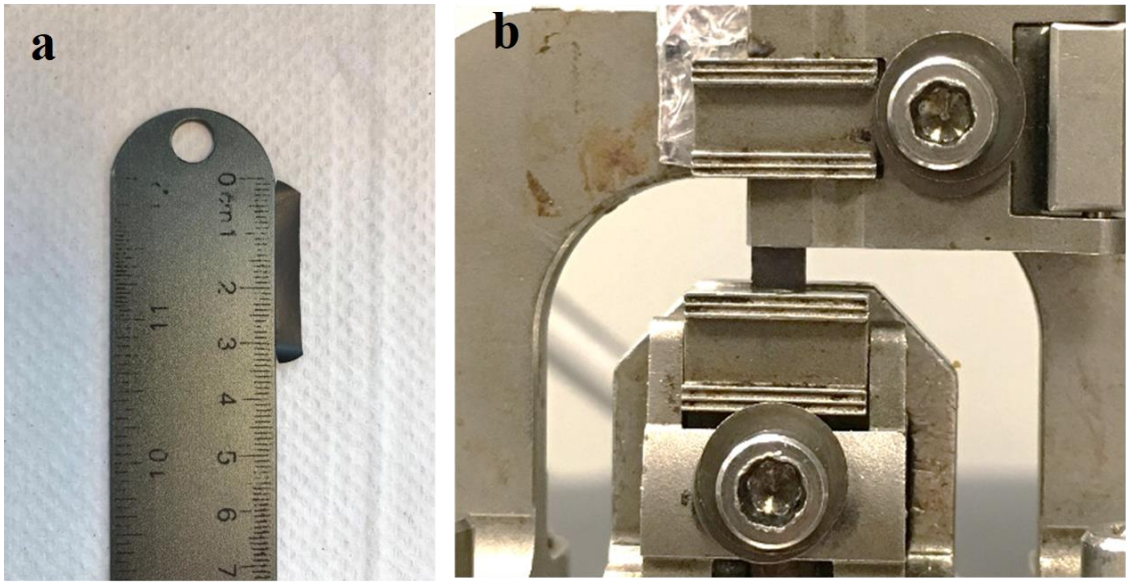

Figure 39 - Tensile test for freestanding GO membrane. (a) Photograph of the prepared GOM-1 sample for testing (three samples were tested to obtain average results). (b) Photograph of DMA tester grips (with the GOM-1 sample loaded).

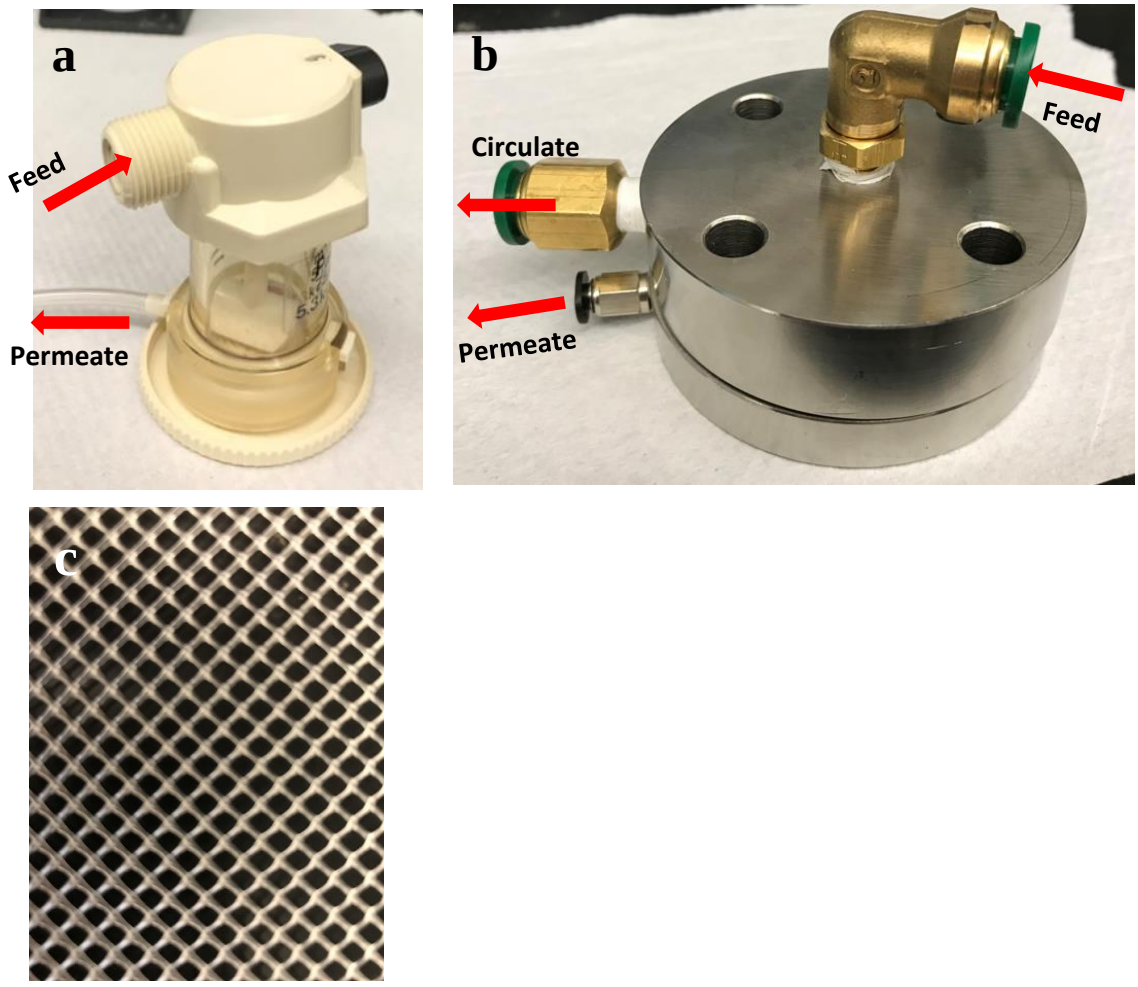

Figure 40 - (a) Photograph of the dead-end stirred cell (Amicon Model 8010, Millipore). (b) Photograph of the modified cross-flow reverse osmosis testing setup. (c) Photograph of the porous spacer (Sterlitech, SEPA CF medium foulant spacer). Note: During the cross-flow RO test, a macroporous filter was used to cover the freestanding GOM and a single-sided carbon tape was used to stabilize the GOM.

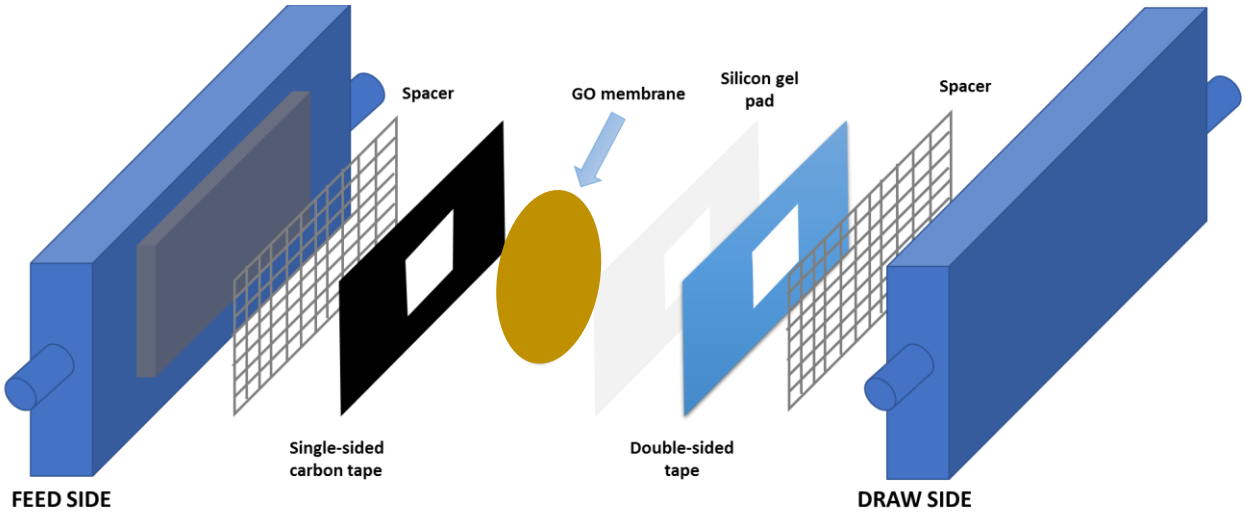

Figure 41 - Schematic illustration of forward osmosis (and pressure retarded osmosis) membrane testing cell. Note: To stabilize the freestanding GOM (as well as the silicon gel pad), a single-sided carbon tape was used at the feed solution side, and a double-sided tape was used at the draw solution side.

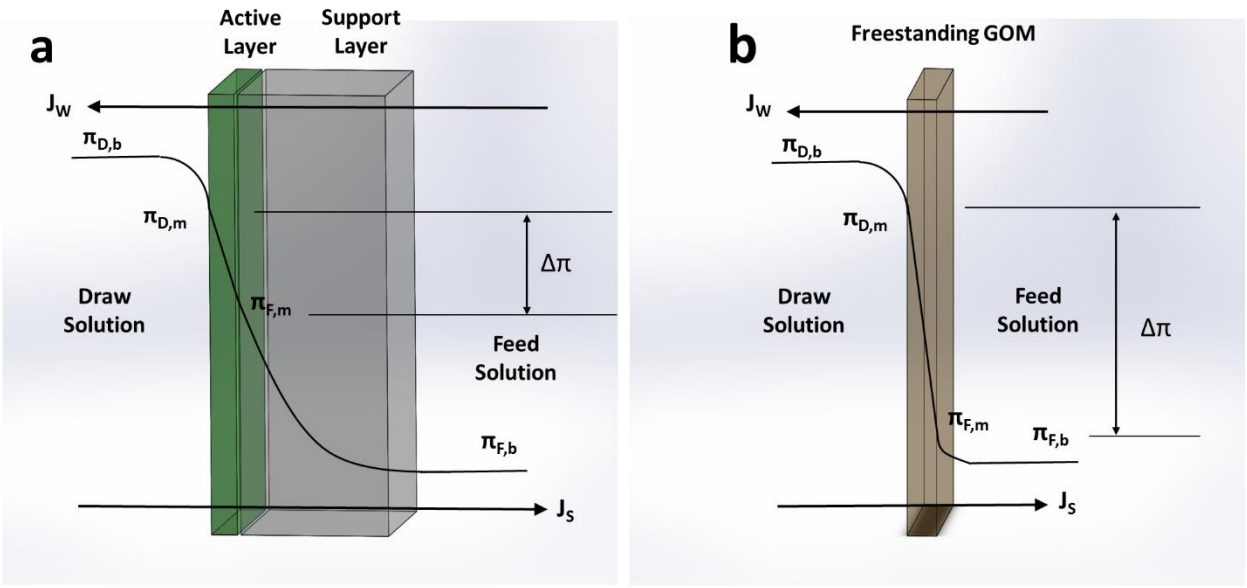

Figure 42 - Schematic view of the osmotic pressure profiles of (a) conventional thin-film composite membrane (PRO mode, active layer facing draw solution) and (b) freestanding GO membrane.

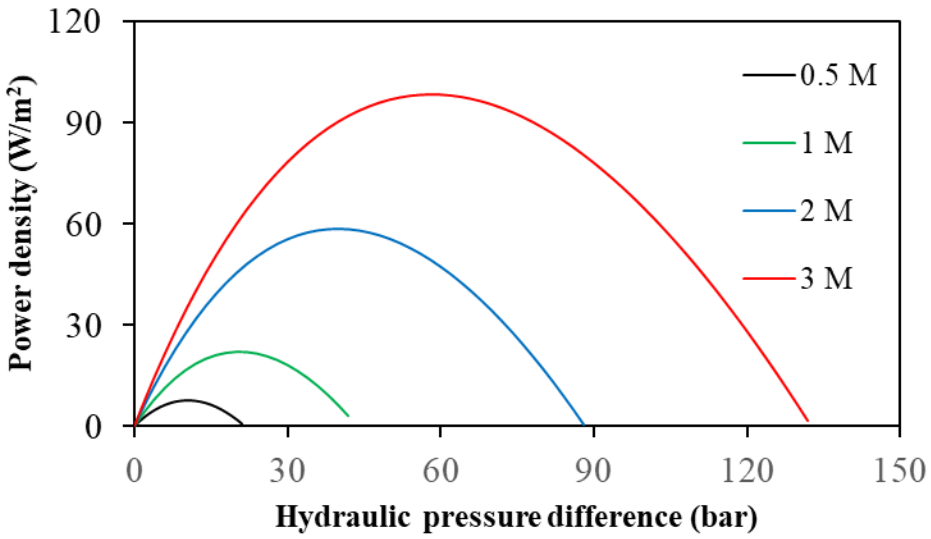

Figure 43 - The calculated theoretical power density of the GOM-1 as a function of hydraulic pressure in PRO system.

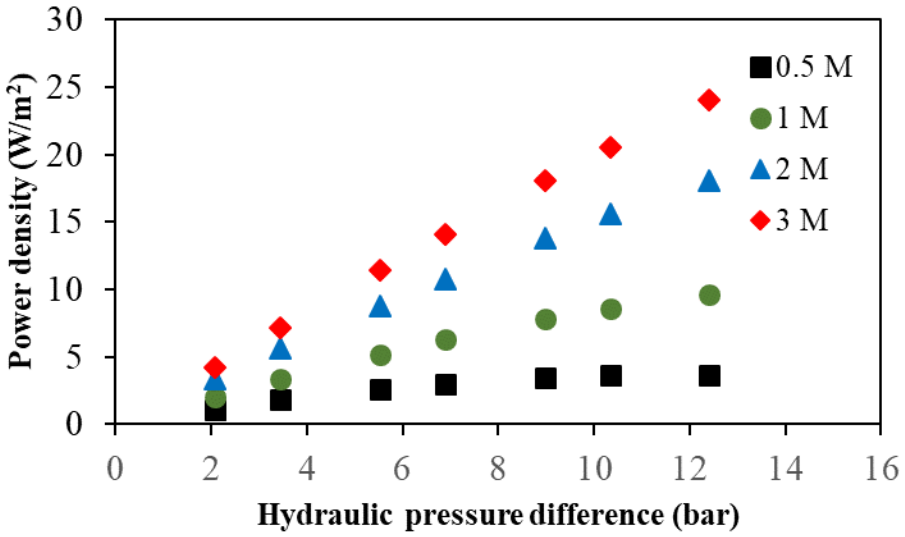

Figure 44 - Plots of the commercial TFC membrane power density as a function of hydraulic pressure in PRO system, with solutions of different NaCl concentrations acting as working solutions. The concentration of feed solution is 0.017 M of NaCl. (The solutions with concentrations of 0.017 M, 0.5 M, 1 M and 3 M represent river water, seawater, seawater brine (50% recovery) and hyper brine, respectively. The concentration of hyper brine is in the salinity range of the Great Salt Lake.)

Table 20 - Tensile properties of GOM-1 samples (average values).

Sample	Young's modulus (GPa)	Tensile stress (MPa)	Tensile strain (%)
GOM-1	37.3±5.0	174.5±3.7	0.47±0.06

APPENDIX D. SUPPORTING INFORMATION FOR CHAPTER 6

D.1 Energy efficiency of the osmotic heat engine

D.1.1. Energy efficiency of the osmotic heat engine

The osmotic heat engine energy efficiency equals the electricity generated from the electricity generation component divided by the thermal energy consumed in the thermal separation process:

$$\eta = \frac{P}{q_H} \tag{46}$$

where P is the electricity generated from the electricity generation component, and q_H is the thermal energy consumed in the thermal separation process.

The electricity generated from the electricity generation component can be expressed as:

$$P = WAt \tag{47}$$

where W is the membrane power density, A is the membrane area, and t is the operation time. The thermal energy consumed can be divided into two different types of energy: 1) the energy needed to increase the feed solution effluent stream ($F_{feed,\ out}$) temperature from room temperature to the temperature of the thermal source and 2) the energy needed to evaporate the solvent from the feed solution to regenerate the solutions. The energy needed to increase the solution temperature is related to the water flow rate and the temperature difference. The energy needed to regenerate the solutions is related to the flow rate and

concentrations of the solutions. By carefully considering the osmotic heat engine process (Figure 46), the thermal energy consumption can be described as:

$$q_H = c_P Q(T_H - T_{room}) + \beta J_W(c_d - c_f)At \quad (48)$$

where c_p is the specific heat capacity of the feed solution, Q is the water flow rate across the membrane (Figure 46), T_H is the temperature of the heat source, T_{room} is the room temperature (25 °C), β is the specific heat duty of ammonium bicarbonate, J_w is the water flux across the GOM, c_d is the concentration of the draw solution, and c_f is the concentration of the feed solution (normally assumed to be zero). To enhance the efficiency of the thermal separation, a heat exchanger is utilized to recover the latent heat accumulated in the feed solution flowing out from the heat source [181]. The recovered heat can then be applied to heat up the subsequent feed solution stream ($F_{feed,\ out}$). By assuming the efficiency of the heat exchanger is close to 1, the thermal energy consumption can be simplified:

$$q_H = \beta J_W(c_d - c_f)At \quad (49)$$

Combining equations (46), (48) and (49) gives:

$$\eta = \frac{W}{\beta J_W(c_d - c_f)} \quad (50)$$

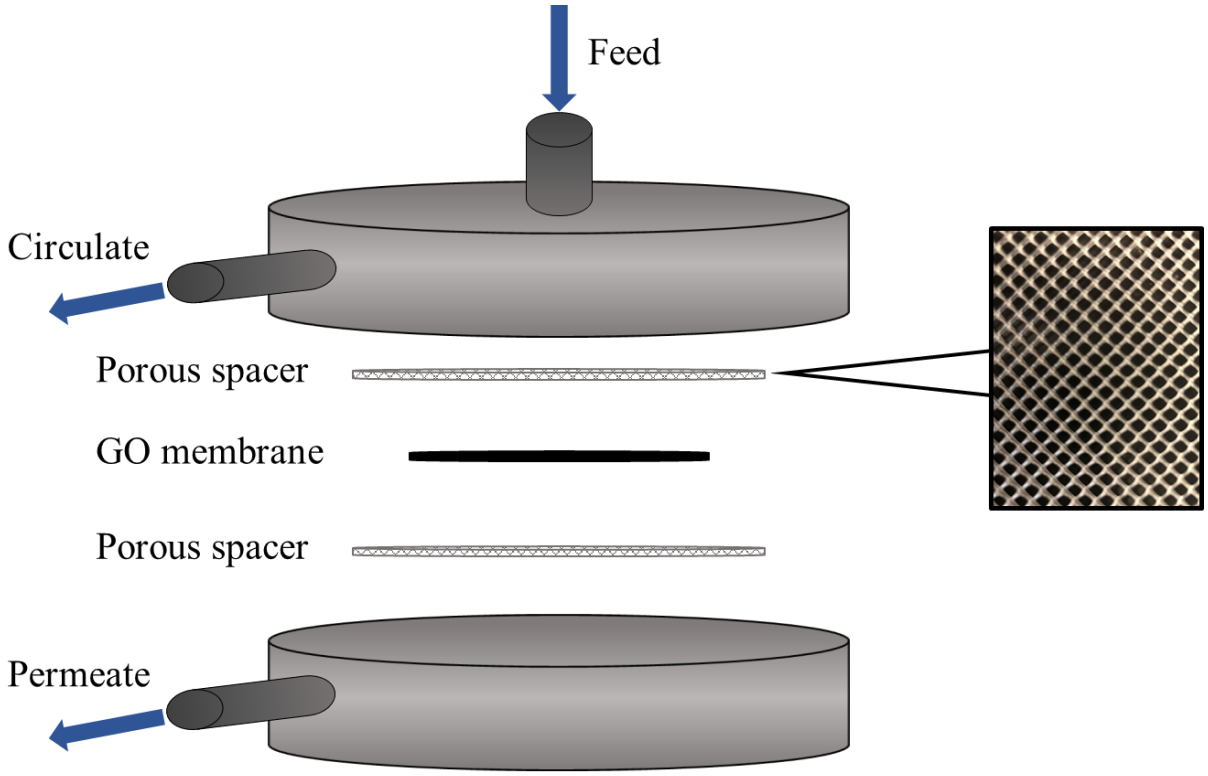

Figure 45 - Schematic illustration of the modified RO testing cell for determining the membrane water permeability coefficient (*A*) and salt permeability coefficient (*B*). The porous frit was replaced by a porous mesh-type SEPA CF medium foulant spacer (Sterlitech Corp., USA).

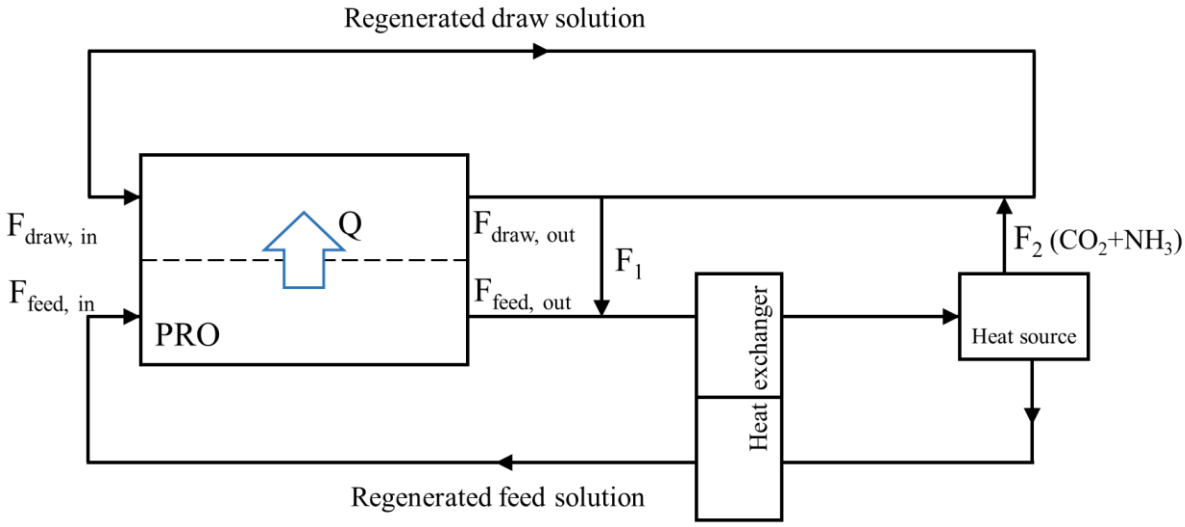

Figure 46 - Schematic illustration of the osmotic heat engine process. A heat exchanger is utilized to recover the latent heat accumulated in the feed water flowing out from the heat source. Q is the water flow rate across the membrane. A stream F_1 ensures a mass balance of the water in the system, and the flow rate of F_1 equals the flow rate across membrane Q.

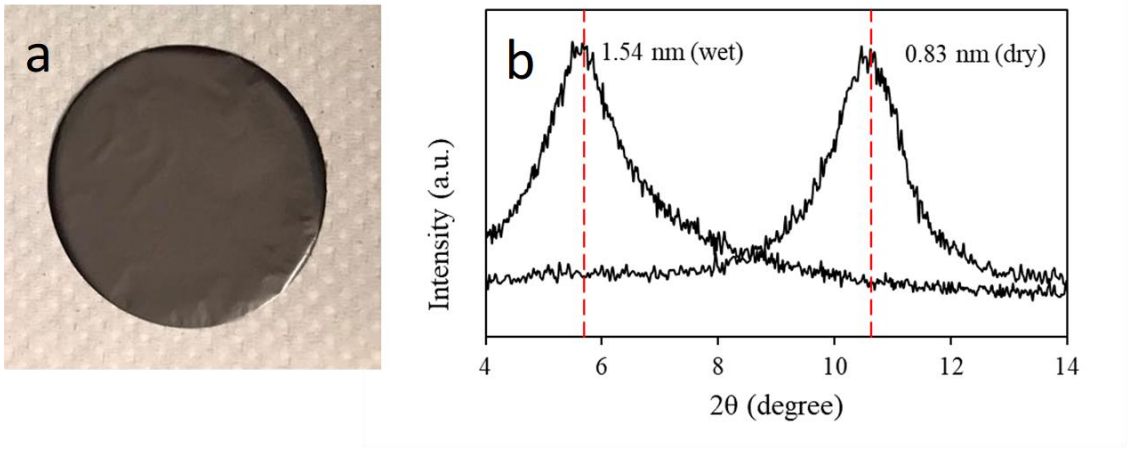

Figure 47 - Additional information on the freestanding GOM. (a) Photograph of the freestanding GOM, and (b) XRD patterns of the dry and wet GOMs.

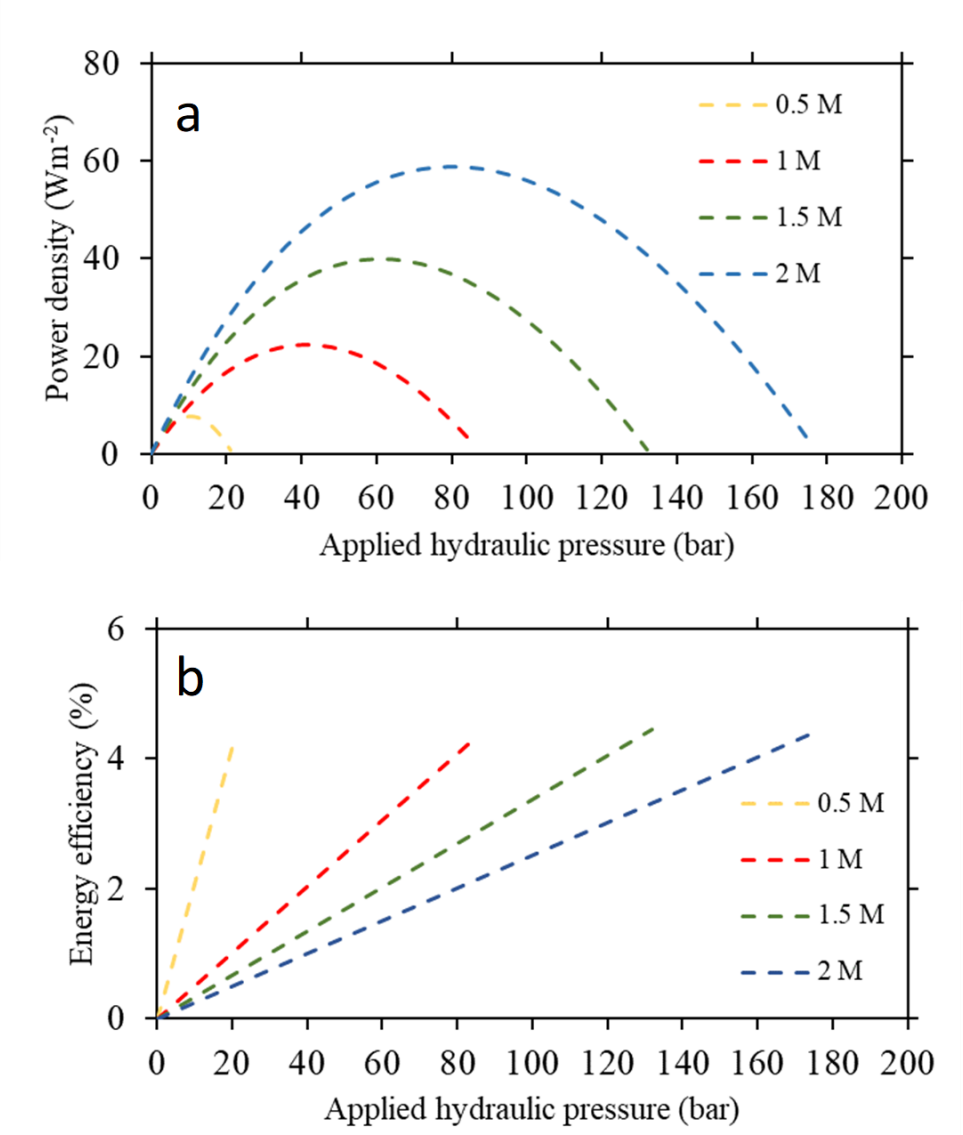

Figure 48 - Supplementary information on the power generation of GOM. (a) Power density values of the GOM with the change of applied hydraulic pressure and (b) energy efficiency values with the change of the applied hydraulic pressure. Several different draw solution concentrations were evaluated.

REFERENCES

[1] S. Chu, A. Majumdar, Opportunities and challenges for a sustainable energy future, nature, 488 (2012) 294-303.

[2] E. Bryant, E.A. Bryant, Climate process and change, Cambridge University Press, 1997.

[3] "Global Fossil Fuel Consumption Surges," a Vital Signs Online report, available at http://www.worldwatch.org/global-fossil-fuel-consumption-surges, accessed July 26, 2018, in.

[4] J.L. Schnoor, Water–energy nexus, in, ACS Publications, 2011.

[5] J.W. Post, J. Veerman, H.V. Hamelers, G.J. Euverink, S.J. Metz, K. Nymeijer, C.J. Buisman, Salinity-gradient power: Evaluation of pressure-retarded osmosis and reverse electrodialysis, Journal of Membrane Science, 288 (2007) 218-230.

[6] R.L. McGinnis, J.R. McCutcheon, M. Elimelech, A novel ammonia–carbon dioxide osmotic heat engine for power generation, Journal of membrane science, 305 (2007) 13-19.

[7] K.L. Hickenbottom, J. Vanneste, L. Miller-Robbie, A. Deshmukh, M. Elimelech, M.B. Heeley, T.Y. Cath, Techno-economic assessment of a closed-loop osmotic heat engine, Journal of Membrane Science, 535 (2017) 178-187.

[8] R.E. Pattle, Production of Electric Power by mixing Fresh and Salt Water in the Hydroelectric Pile, Nature, 174 (1954) 660-660.

[9] T. Humplik, J. Lee, S. O'hern, B. Fellman, M. Baig, S. Hassan, M. Atieh, F. Rahman, T. Laoui, R. Karnik, Nanostructured materials for water desalination, Nanotechnology, 22 (2011) 292001.

[10] G.Z. Ramon, B.J. Feinberg, E.M. Hoek, Membrane-based production of salinity-gradient power, Energy & environmental science, 4 (2011) 4423-4434.

[11] G.L. Wick, Power from salinity gradients, Energy, 3 (1978) 95-100.

[12] B.E. Logan, M. Elimelech, Membrane-based processes for sustainable power generation using water, Nature, 488 (2012) 313-319.

[13] K. Lee, R. Baker, H. Lonsdale, Membranes for power generation by pressure-retarded osmosis, Journal of Membrane Science, 8 (1981) 141-171.

[14] R.E. Lacey, Energy by reverse electrodialysis, Ocean Engineering, 7 (1980) 1-47.

[15] J.G. Hong, B. Zhang, S. Glabman, N. Uzal, X. Dou, H. Zhang, X. Wei, Y. Chen, Potential ion exchange membranes and system performance in reverse electrodialysis for power generation: A review, Journal of Membrane Science, 486 (2015) 71-88.

[16] D. Brogioli, Extracting renewable energy from a salinity difference using a capacitor, Physical review letters, 103 (2009) 058501.

[17] H. Lu, J.C. Walton, A.H. Swift, Desalination coupled with salinity-gradient solar ponds, Desalination, 136 (2001) 13-23.

[18] A. Siria, P. Poncharal, A.-L. Biance, R. Fulcrand, X. Blase, S.T. Purcell, L. Bocquet, Giant osmotic energy conversion measured in a single transmembrane boron nitride nanotube, Nature, 494 (2013) 455.

[19] Z. Jia, B. Wang, S. Song, Y. Fan, Blue energy: Current technologies for sustainable power generation from water salinity gradient, Renewable and Sustainable Energy Reviews, 31 (2014) 91-100.

[20] N.Y. Yip, D.A. Vermaas, K. Nijmeijer, M. Elimelech, Thermodynamic, Energy Efficiency, and Power Density Analysis of Reverse Electrodialysis Power Generation with Natural Salinity Gradients, Environmental Science & Technology, 48 (2014) 4925-4936.

[21] M. Turek, B. Bandura, Renewable energy by reverse electrodialysis, Desalination, 205 (2007) 67-74.

[22] J. Veerman, M. Saakes, S. Metz, G. Harmsen, Reverse electrodialysis: performance of a stack with 50 cells on the mixing of sea and river water, Journal of Membrane Science, 327 (2009) 136-144.

[23] D.A. Vermaas, J. Veerman, M. Saakes, K. Nijmeijer, Influence of multivalent ions on renewable energy generation in reverse electrodialysis, Energy & Environmental Science, 7 (2014) 1434-1445.

[24] J.G. Hong, W. Zhang, J. Luo, Y. Chen, Modeling of power generation from the mixing of simulated saline and freshwater with a reverse electrodialysis system: The effect of monovalent and multivalent ions, Applied Energy, 110 (2013) 244-251.

[25] E. Brauns, Salinity gradient power by reverse electrodialysis: effect of model parameters on electrical power output, Desalination, 237 (2009) 378-391.

[26] J.W. Post, C.H. Goeting, J. Valk, S. Goinga, J. Veerman, H.V.M. Hamelers, P.J.F.M. Hack, Towards implementation of reverse electrodialysis for power generation from salinity gradients, Desalination and Water Treatment, 16 (2010) 182-193.

[27] D.A. Vermaas, D. Kunteng, M. Saakes, K. Nijmeijer, Fouling in reverse electrodialysis under natural conditions, Water research, 47 (2013) 1289-1298.

[28] D.A. Vermaas, M. Saakes, K. Nijmeijer, Early detection of preferential channeling in reverse electrodialysis, Electrochimica acta, 117 (2014) 9-17.

[29] D.A. Vermaas, D. Kunteng, J. Veerman, M. Saakes, K. Nijmeijer, Periodic feedwater reversal and air sparging as antifouling strategies in reverse electrodialysis, Environmental science & technology, 48 (2014) 3065-3073.

[30] S. Mulyati, R. Takagi, A. Fujii, Y. Ohmukai, T. Maruyama, H. Matsuyama, Improvement of the antifouling potential of an anion exchange membrane by surface modification with a polyelectrolyte for an electrodialysis process, Journal of Membrane Science, 417 (2012) 137-143.

[31] S. Mulyati, R. Takagi, A. Fujii, Y. Ohmukai, H. Matsuyama, Simultaneous improvement of the monovalent anion selectivity and antifouling properties of an anion exchange membrane in an electrodialysis process, using polyelectrolyte multilayer deposition, Journal of Membrane Science, 431 (2013) 113-120.

[32] M. Vaselbehagh, H. Karkhanechi, S. Mulyati, R. Takagi, H. Matsuyama, Improved antifouling of anion-exchange membrane by polydopamine coating in electrodialysis process, Desalination, 332 (2014) 126-133.

[33] L. Bazinet, M. Araya-Farias, Electrodialysis of calcium and carbonate high concentration solutions and impact on composition in cations of membrane fouling, Journal of colloid and interface science, 286 (2005) 639-646.

[34] L. Bazinet, M. Araya-Farias, Effect of calcium and carbonate concentrations on cationic membrane fouling during electrodialysis, Journal of colloid and interface science, 281 (2005) 188-196.

[35] J.G. Hong, Y. Chen, Nanocomposite reverse electrodialysis (RED) ion-exchange membranes for salinity gradient power generation, Journal of Membrane Science, 460 (2014) 139-147.

[36] J.G. Hong, S. Glabman, Y. Chen, Effect of inorganic filler size on electrochemical performance of nanocomposite cation exchange membranes for salinity gradient power generation, Journal of Membrane Science, 482 (2015) 33-41.

[37] J.G. Hong, Y. Chen, Evaluation of electrochemical properties and reverse electrodialysis performance for porous cation exchange membranes with sulfate-functionalized iron oxide, Journal of Membrane Science, 473 (2015) 210-217.

[38] E. Güler, W. van Baak, M. Saakes, K. Nijmeijer, Monovalent-ion-selective membranes for reverse electrodialysis, Journal of membrane science, 455 (2014) 254-270.

[39] E. Guler, Y. Zhang, M. Saakes, K. Nijmeijer, Tailor‐made anion‐exchange membranes for salinity gradient power generation using reverse electrodialysis, ChemSusChem, 5 (2012) 2262-2270.

[40] D.A. Vermaas, M. Saakes, K. Nijmeijer, Power generation using profiled membranes in reverse electrodialysis, Journal of membrane science, 385 (2011) 234-242.

[41] X. Zuo, S. Yu, X. Xu, R. Bao, J. Xu, W. Qu, Preparation of organic–inorganic hybrid cation-exchange membranes via blending method and their electrochemical characterization, Journal of Membrane Science, 328 (2009) 23-30.

[42] X. Xiao, C. Wu, P. Cui, J. Luo, Y. Wu, T. Xu, Cation exchange hybrid membranes from SPPO and multi-alkoxy silicon copolymer: Preparation, properties and diffusion dialysis performances for sodium hydroxide recovery, Journal of Membrane Science, 379 (2011) 112-120.

[43] G. Kickelbick, Concepts for the incorporation of inorganic building blocks into organic polymers on a nanoscale, Progress in polymer science, 28 (2003) 83-114.

[44] T. Xu, Ion exchange membranes: state of their development and perspective, Journal of Membrane Science, 263 (2005) 1-29.

[45] S. Kango, S. Kalia, A. Celli, J. Njuguna, Y. Habibi, R. Kumar, Surface modification of inorganic nanoparticles for development of organic–inorganic nanocomposites—A review, Progress in Polymer Science, 38 (2013) 1232-1261.

[46] Z. Spitalsky, D. Tasis, K. Papagelis, C. Galiotis, Carbon nanotube–polymer composites: chemistry, processing, mechanical and electrical properties, Progress in polymer science, 35 (2010) 357-401.

[47] V. Datsyuk, M. Kalyva, K. Papagelis, J. Parthenios, D. Tasis, A. Siokou, I. Kallitsis, C. Galiotis, Chemical oxidation of multiwalled carbon nanotubes, Carbon, 46 (2008) 833-840.

[48] N.G. Sahoo, S. Rana, J.W. Cho, L. Li, S.H. Chan, Polymer nanocomposites based on functionalized carbon nanotubes, Progress in polymer science, 35 (2010) 837-867.

[49] D. Tasis, N. Tagmatarchis, A. Bianco, M. Prato, Chemistry of carbon nanotubes, Chemical reviews, 106 (2006) 1105-1136.

[50] J. Chen, M.A. Hamon, H. Hu, Y. Chen, A.M. Rao, P.C. Eklund, R.C. Haddon, Solution properties of single-walled carbon nanotubes, Science, 282 (1998) 95-98.

[51] Y. Yao, Z. Lin, Y. Li, M. Alcoutlabi, H. Hamouda, X. Zhang, Superacidic Electrospun Fiber‐Nafion Hybrid Proton Exchange Membranes, Advanced Energy Materials, 1 (2011) 1133-1140.

[52] V. Vatanpour, S.S. Madaeni, R. Moradian, S. Zinadini, B. Astinchap, Fabrication and characterization of novel antifouling nanofiltration membrane prepared from oxidized multiwalled carbon nanotube/polyethersulfone nanocomposite, Journal of Membrane Science, 375 (2011) 284-294.

[53] E. Celik, H. Park, H. Choi, H. Choi, Carbon nanotube blended polyethersulfone membranes for fouling control in water treatment, Water research, 45 (2011) 274-282.

[54] C. Li, J. Liu, R. Guan, P. Zhang, Q. Zhang, Effect of heating and stretching membrane on ionic conductivity of sulfonated poly (phenylene oxide), Journal of membrane science, 287 (2007) 180-186.

[55] B. Kosmala, J. Schauer, Ion-exchange membranes prepared by blending sulfonated poly(2,6-dimethyl-1,4-phenylene oxide) with polybenzimidazole, Journal of Applied Polymer Science, 85 (2002) 1118-1127.

[56] T. Xu, D. Wu, L. Wu, Poly (2, 6-dimethyl-1, 4-phenylene oxide)(PPO)—a versatile starting polymer for proton conductive membranes (PCMs), Progress in Polymer Science, 33 (2008) 894-915.

[57] X. Tongwen, Y. Weihua, H. Binglin, Ionic conductivity threshold in sulfonated poly (phenylene oxide) matrices: a combination of three-phase model and percolation theory, Chemical Engineering Science, 56 (2001) 5343-5350.

[58] H. Fu, L. Jia, J. Xu, Studies on the sulfonation of poly(phenylene oxide) (PPO) and permeation behavior of gases and water vapor through sulfonated PPO membranes. I. Sulfonation of PPO and characterization of the products, Journal of Applied Polymer Science, 51 (1994) 1399-1404.

[59] S.W. Lin, H. Espinoza-Gomez, Development of energy-saving spinning membrane systemand negatively charged ultrafiltration membranes for recovering oil from waste machine cutting fluid, Desalination, 174 (2005) 109-123.

[60] P. Długołęcki, B. Anet, S.J. Metz, K. Nijmeijer, M. Wessling, Transport limitations in ion exchange membranes at low salt concentrations, Journal of Membrane Science, 346 (2010) 163-171.

[61] J.-H. Chang, A.V. Ellis, C.-H. Tung, W.-C. Huang, Copper cation transport and scaling of ionic exchange membranes using electrodialysis under electroconvection conditions, Journal of Membrane Science, 361 (2010) 56-62.

[62] S. Hosseini, S. Madaeni, A. Khodabakhshi, The electrochemical characterization of ion exchange membranes in different electrolytic environments: investigation of concentration and pH effects, Separation Science and Technology, 47 (2012) 455-462.

[63] K.-H. Oh, D. Lee, M.-J. Choo, K.H. Park, S. Jeon, S.H. Hong, J.-K. Park, J.W. Choi, Enhanced durability of polymer electrolyte membrane fuel cells by functionalized 2D boron nitride nanoflakes, ACS applied materials & interfaces, 6 (2014) 7751-7758.

[64] S. Yun, H. Im, Y. Heo, J. Kim, Crosslinked sulfonated poly (vinyl alcohol)/sulfonated multi-walled carbon nanotubes nanocomposite membranes for direct methanol fuel cells, Journal of Membrane Science, 380 (2011) 208-215.

[65] A. Rahimpour, M. Jahanshahi, N. Mortazavian, S.S. Madaeni, Y. Mansourpanah, Preparation and characterization of asymmetric polyethersulfone and thin-film composite polyamide nanofiltration membranes for water softening, Applied Surface Science, 256 (2010) 1657-1663.

[66] S. Hosseini, F. Jeddi, M. Nemati, S. Madaeni, A. Moghadassi, Electrodialysis heterogeneous anion exchange membrane modified by PANI/MWCNT composite nanoparticles: Preparation, characterization and ionic transport property in desalination, Desalination, 341 (2014) 107-114.

[67] Y.-J. Choi, J.-H. Song, M.-S. Kang, B.-K. Seo, Preparation and electrochemical characterizations of anion-permselective membranes with structurally stable ion-exchange sites, Electrochimica Acta, 180 (2015) 71-77.

[68] B. Lin, S. Cheng, L. Qiu, F. Yan, S. Shang, J. Lu, Protic ionic liquid-based hybrid proton-conducting membranes for anhydrous proton exchange membrane application, Chemistry of Materials, 22 (2010) 1807-1813.

[69] P. Długołęcki, K. Nymeijer, S. Metz, M. Wessling, Current status of ion exchange membranes for power generation from salinity gradients, Journal of Membrane Science, 319 (2008) 214-222.

[70] G.M. Geise, M.A. Hickner, B.E. Logan, Ionic resistance and permselectivity tradeoffs in anion exchange membranes, ACS applied materials & interfaces, 5 (2013) 10294-10301.

[71] M. Tedesco, E. Brauns, A. Cipollina, G. Micale, P. Modica, G. Russo, J. Helsen, Reverse electrodialysis with saline waters and concentrated brines: A laboratory investigation towards technology scale-up, Journal of Membrane Science, 492 (2015) 9-20.

[72] D.A. Vermaas, E. Guler, M. Saakes, K. Nijmeijer, Theoretical power density from salinity gradients using reverse electrodialysis, Energy Procedia, 20 (2012) 170-184.

[73] A. Daniilidis, D.A. Vermaas, R. Herber, K. Nijmeijer, Experimentally obtainable energy from mixing river water, seawater or brines with reverse electrodialysis, Renewable energy, 64 (2014) 123-131.

[74] H. Zhang, P.K. Shen, Recent development of polymer electrolyte membranes for fuel cells, Chemical reviews, 112 (2012) 2780-2832.

[75] J.R. Varcoe, P. Atanassov, D.R. Dekel, A.M. Herring, M.A. Hickner, P.A. Kohl, A.R. Kucernak, W.E. Mustain, K. Nijmeijer, K. Scott, Anion-exchange membranes in electrochemical energy systems, Energy & environmental science, 7 (2014) 3135-3191.

[76] G. Merle, M. Wessling, K. Nijmeijer, Anion exchange membranes for alkaline fuel cells: A review, Journal of Membrane Science, 377 (2011) 1-35.

[77] K. Kreuer, On the development of proton conducting polymer membranes for hydrogen and methanol fuel cells, Journal of membrane science, 185 (2001) 29-39.

[78] T. Sata, Studies on ion exchange membranes with permselectivity for specific ions in electrodialysis, Journal of membrane science, 93 (1994) 117-135.

[79] M. Kariduraganavar, R. Nagarale, A. Kittur, S. Kulkarni, Ion-exchange membranes: preparative methods for electrodialysis and fuel cell applications, Desalination, 197 (2006) 225-246.

[80] C. Fernandez-Gonzalez, A. Dominguez-Ramos, R. Ibañez, Y. Chen, A. Irabien, Valorization of desalination brines by electrodialysis with bipolar membranes using nanocomposite anion exchange membranes, Desalination, 406 (2017) 16-24.

[81] X. Tong, B. Zhang, Y. Chen, Fouling resistant nanocomposite cation exchange membrane with enhanced power generation for reverse electrodialysis, Journal of Membrane Science, 516 (2016) 162-171.

[82] X. Li, H. Zhang, Z. Mai, H. Zhang, I. Vankelecom, Ion exchange membranes for vanadium redox flow battery (VRB) applications, Energy & Environmental Science, 4 (2011) 1147-1160.

[83] W. Wang, Q. Luo, B. Li, X. Wei, L. Li, Z. Yang, Recent progress in redox flow battery research and development, Advanced Functional Materials, 23 (2013) 970-986.

[84] J.R. Kim, S. Cheng, S.-E. Oh, B.E. Logan, Power generation using different cation, anion, and ultrafiltration membranes in microbial fuel cells, Environmental science & technology, 41 (2007) 1004-1009.

[85] Z. Du, H. Li, T. Gu, A state of the art review on microbial fuel cells: a promising technology for wastewater treatment and bioenergy, Biotechnology advances, 25 (2007) 464-482.

[86] G. He, Z. Li, J. Zhao, S. Wang, H. Wu, M.D. Guiver, Z. Jiang, Nanostructured Ion‐Exchange Membranes for Fuel Cells: Recent Advances and Perspectives, Advanced Materials, 27 (2015) 5280-5295.

[87] B.P. Tripathi, V.K. Shahi, Organic–inorganic nanocomposite polymer electrolyte membranes for fuel cell applications, Progress in Polymer Science, 36 (2011) 945-979.

[88] Y. Li, G. He, S. Wang, S. Yu, F. Pan, H. Wu, Z. Jiang, Recent advances in the fabrication of advanced composite membranes, Journal of Materials Chemistry A, 1 (2013) 10058-10077.

[89] S. Chung, Y. Wang, L. Persi, F. Croce, S. Greenbaum, B. Scrosati, E. Plichta, Enhancement of ion transport in polymer electrolytes by addition of nanoscale inorganic oxides, Journal of Power Sources, 97 (2001) 644-648.

[90] J.R. Capadona, O. Van Den Berg, L.A. Capadona, M. Schroeter, S.J. Rowan, D.J. Tyler, C. Weder, A versatile approach for the processing of polymer nanocomposites with self-assembled nanofibre templates, Nature Nanotechnology, 2 (2007) 765-769.

[91] Y.-H. Su, Y.-L. Liu, Y.-M. Sun, J.-Y. Lai, D.-M. Wang, Y. Gao, B. Liu, M.D. Guiver, Proton exchange membranes modified with sulfonated silica nanoparticles for direct methanol fuel cells, Journal of Membrane Science, 296 (2007) 21-28.

[92] H. Zarrin, D. Higgins, Y. Jun, Z. Chen, M. Fowler, Functionalized graphene oxide nanocomposite membrane for low humidity and high temperature proton exchange membrane fuel cells, The Journal of Physical Chemistry C, 115 (2011) 20774-20781.

[93] M. Tortello, S. Bianco, V. Ijeri, P. Spinelli, E. Tresso, Nafion membranes with vertically-aligned CNTs for mixed proton and electron conduction, Journal of Membrane Science, 415 (2012) 346-352.

[94] C.H. Rhee, H.K. Kim, H. Chang, J.S. Lee, Nafion/sulfonated montmorillonite composite: a new concept electrolyte membrane for direct methanol fuel cells, Chemistry of materials, 17 (2005) 1691-1697.

[95] B.P. Ladewig, R.B. Knott, D.J. Martin, J.C.D. da Costa, G.Q. Lu, Nafion-MPMDMS nanocomposite membranes with low methanol permeability, Electrochemistry communications, 9 (2007) 781-786.

[96] C. Jia, Y. Cheng, X. Ling, G. Wei, J. Liu, C. Yan, Sulfonated Poly (Ether Ether Ketone)/Functionalized Carbon Nanotube Composite Membrane for Vanadium Redox Flow Battery Applications, Electrochimica Acta, 153 (2015) 44-48.

[97] S.L. Avilés-Barreto, D. Suleiman, Effect of single-walled carbon nanotubes on the transport properties of sulfonated poly (styrene–isobutylene–styrene) membranes, Journal of Membrane Science, 474 (2015) 92-102.

[98] B.G. Choi, J. Hong, Y.C. Park, D.H. Jung, W.H. Hong, P.T. Hammond, H. Park, Innovative polymer nanocomposite electrolytes: nanoscale manipulation of ion channels by functionalized graphenes, ACS nano, 5 (2011) 5167-5174.

[99] Y.-L. Liu, C.-Y. Hsu, Y.-H. Su, J.-Y. Lai, Chitosan-silica complex membranes from sulfonic acid functionalized silica nanoparticles for pervaporation dehydration of ethanol-water solutions, Biomacromolecules, 6 (2005) 368-373.

[100] D. Wu, T. Xu, L. Wu, Y. Wu, Hybrid acid–base polymer membranes prepared for application in fuel cells, Journal of Power Sources, 186 (2009) 286-292.

[101] A.N. Mondal, C. Dai, J. Pan, C. Zheng, M.M. Hossain, M.I. Khan, L. Wu, T. Xu, Novel pendant benzene disulfonic acid blended SPPO membranes for alkali recovery: fabrication and properties, ACS applied materials & interfaces, 7 (2015) 15944-15954.

[102] C. Klaysom, R. Marschall, S.-H. Moon, B.P. Ladewig, G.M. Lu, L. Wang, Preparation of porous composite ion-exchange membranes for desalination application, Journal of Materials Chemistry, 21 (2011) 7401-7409.

[103] V.I. Zabolotsky, V.V. Nikonenko, Effect of structural membrane inhomogeneity on transport properties, Journal of Membrane Science, 79 (1993) 181-198.

[104] L.V. Karpenko-Jereb, N.P. Berezina, Determination of structural, selective, electrokinetic and percolation characteristics of ion-exchange membranes from conductive data, Desalination, 245 (2009) 587-596.

[105] M. Marino, J. Melchior, A. Wohlfarth, K. Kreuer, Hydroxide, halide and water transport in a model anion exchange membrane, Journal of Membrane Science, 464 (2014) 61-71.

[106] A. Amel, N. Gavish, L. Zhu, D.R. Dekel, M.A. Hickner, Y. Ein-Eli, Bicarbonate and chloride anion transport in anion exchange membranes, Journal of Membrane Science, 514 (2016) 125-134.

[107] B. Mistry, A handbook of spectroscopic data, New Delhi: Oxford Book Company, 2009.

[108] P. Leclère, R. Lazzaroni, J.-L. Brédas, J.M. Yu, P. Dubois, R. Jérôme, Microdomain morphology analysis of block copolymers by atomic force microscopy with phase detection imaging, Langmuir, 12 (1996) 4317-4320.

[109] R.S. McLean, B.B. Sauer, Tapping-mode AFM studies using phase detection for resolution of nanophases in segmented polyurethanes and other block copolymers, Macromolecules, 30 (1997) 8314-8317.

[110] O. Diat, G. Gebel, Fuel cells: Proton channels, Nature materials, 7 (2008) 13-14.

[111] N. Tan, G. Xiao, D. Yan, Sulfonated Polybenzothiazoles: A Novel Candidate for Proton Exchange Membranes†, Chemistry of Materials, 22 (2009) 1022-1031.

[112] S. Yun, J. Parrondo, F. Zhang, V. Ramani, Microstructure-property relationships in sulfonated polyether ether ketone/silsesquioxane composite membranes for direct methanol fuel cells, Journal of The Electrochemical Society, 161 (2014) F815-F822.

[113] J.-H. Kim, S.-K. Kim, K. Nam, D.-W. Kim, Composite proton conducting membranes based on Nafion and sulfonated SiO 2 nanoparticles, Journal of membrane science, 415 (2012) 696-701.

[114] C. Klaysom, S.-H. Moon, B.P. Ladewig, G.M. Lu, L. Wang, The influence of inorganic filler particle size on composite ion-exchange membranes for desalination, The Journal of Physical Chemistry C, 115 (2011) 15124-15132.

[115] W.Y. Hsu, J.R. Barkley, P. Meakin, Ion percolation and insulator-to-conductor transition in Nafion perfluorosulfonic acid membranes, Macromolecules, 13 (1980) 198-200.

[116] C. Peng, W. Zhang, H. Gao, Y. Li, X. Tong, K. Li, X. Zhu, Y. Wang, Y. Chen, Behavior and Potential Impacts of Metal-Based Engineered Nanoparticles in Aquatic Environments, Nanomaterials, 7 (2017) 21.

[117] X. Zuo, S. Yu, X. Xu, J. Xu, R. Bao, X. Yan, New PVDF organic–inorganic membranes: the effect of SiO 2 nanoparticles content on the transport performance of anion-exchange membranes, Journal of Membrane Science, 340 (2009) 206-213.

[118] O. Ellabban, H. Abu-Rub, F. Blaabjerg, Renewable energy resources: Current status, future prospects and their enabling technology, Renewable and Sustainable Energy Reviews, 39 (2014) 748-764.

[119] J. Feng, M. Graf, K. Liu, D. Ovchinnikov, D. Dumcenco, M. Heiranian, V. Nandigana, N.R. Aluru, A. Kis, A. Radenovic, Single-layer MoS2 nanopores as nanopower generators, Nature, 536 (2016) 197-200.

[120] G. Wick, Prospects for renewable energy from sea, Mar. Technol. Soc. J., 11 (1977) 16-21.

[121] S. Loeb, Production of energy from concentrated brines by pressure-retarded osmosis: I. Preliminary technical and economic correlations, Journal of Membrane Science, 1 (1976) 49-63.

[122] T.Y. Cath, A.E. Childress, M. Elimelech, Forward osmosis: principles, applications, and recent developments, Journal of membrane science, 281 (2006) 70-87.

[123] C. Klaysom, T.Y. Cath, T. Depuydt, I.F. Vankelecom, Forward and pressure retarded osmosis: potential solutions for global challenges in energy and water supply, Chemical society reviews, 42 (2013) 6959-6989.

[124] Y.C. Kim, Y. Kim, D. Oh, K.H. Lee, Experimental investigation of a spiral-wound pressure-retarded osmosis membrane module for osmotic power generation, Environmental science & technology, 47 (2013) 2966-2973.

[125] A.P. Straub, A. Deshmukh, M. Elimelech, Pressure-retarded osmosis for power generation from salinity gradients: is it viable?, Energy & Environmental Science, 9 (2016) 31-48.

[126] S. Lin, A.P. Straub, M. Elimelech, Thermodynamic limits of extractable energy by pressure retarded osmosis, Energy & Environmental Science, 7 (2014) 2706-2714.

[127] N.Y. Yip, A. Tiraferri, W.A. Phillip, J.D. Schiffman, L.A. Hoover, Y.C. Kim, M. Elimelech, Thin-film composite pressure retarded osmosis membranes for sustainable

power generation from salinity gradients, Environmental science & technology, 45 (2011) 4360-4369.

[128] G.D. Mehta, S. Loeb, Internal polarization in the porous substructure of a semipermeable membrane under pressure-retarded osmosis, Journal of Membrane Science, 4 (1978) 261-265.

[129] G. Mehta, S. Loeb, Performance of permasep B-9 and B-10 membranes in various osmotic regions and at high osmotic pressures, Journal of Membrane Science, 4 (1978) 335-349.

[130] H. Jellinek, H. Masuda, Osmo-power. Theory and performance of an osmo-power pilot plant, Ocean engineering, 8 (1981) 103-128.

[131] A. Achilli, T.Y. Cath, A.E. Childress, Power generation with pressure retarded osmosis: An experimental and theoretical investigation, Journal of membrane science, 343 (2009) 42-52.

[132] S. Chou, R. Wang, L. Shi, Q. She, C. Tang, A.G. Fane, Thin-film composite hollow fiber membranes for pressure retarded osmosis (PRO) process with high power density, Journal of membrane science, 389 (2012) 25-33.

[133] J.T. Arena, B. McCloskey, B.D. Freeman, J.R. McCutcheon, Surface modification of thin film composite membrane support layers with polydopamine: enabling use of reverse osmosis membranes in pressure retarded osmosis, Journal of Membrane Science, 375 (2011) 55-62.

[134] G. Han, S. Zhang, X. Li, T.-S. Chung, High performance thin film composite pressure retarded osmosis (PRO) membranes for renewable salinity-gradient energy generation, Journal of membrane science, 440 (2013) 108-121.

[135] D.A. Dikin, S. Stankovich, E.J. Zimney, R.D. Piner, G.H. Dommett, G. Evmenenko, S.T. Nguyen, R.S. Ruoff, Preparation and characterization of graphene oxide paper, Nature, 448 (2007) 457.

[136] Y. Shin, W. Liu, B. Schwenzer, S. Manandhar, D. Chase-Woods, M.H. Engelhard, R. Devanathan, L.S. Fifield, W.D. Bennett, B. Ginovska, Graphene oxide membranes with high permeability and selectivity for dehumidification of air, Carbon, 106 (2016) 164-170.

[137] R. Nair, H. Wu, P. Jayaram, I. Grigorieva, A. Geim, Unimpeded permeation of water through helium-leak–tight graphene-based membranes, Science, 335 (2012) 442-444.

[138] N. Wei, X. Peng, Z. Xu, Breakdown of fast water transport in graphene oxides, Physical Review E, 89 (2014) 012113.

[139] N. Wei, X. Peng, Z. Xu, Understanding water permeation in graphene oxide membranes, ACS applied materials & interfaces, 6 (2014) 5877-5883.

[140] H. Dai, Z. Xu, X. Yang, Water Permeation and Ion Rejection in Layer-by-Layer Stacked Graphene Oxide Nanochannels: A Molecular Dynamics Simulation, The Journal of Physical Chemistry C, 120 (2016) 22585-22596.

[141] A. Montessori, C. Amadei, G. Falcucci, M. Sega, C. Vecitis, S. Succi, Extended friction elucidates the breakdown of fast water transport in graphene oxide membranes, EPL (Europhysics Letters), 116 (2017) 54002.

[142] M. Hu, B. Mi, Enabling graphene oxide nanosheets as water separation membranes, Environmental science & technology, 47 (2013) 3715-3723.

[143] Y. Han, Z. Xu, C. Gao, Ultrathin graphene nanofiltration membrane for water purification, Advanced Functional Materials, 23 (2013) 3693-3700.

[144] J.-H. Jang, J.Y. Woo, J. Lee, C.-S. Han, Ambivalent effect of thermal reduction in mass rejection through graphene oxide membrane, Environmental Science & Technology, 50 (2016) 10024-10030.

[145] Y. You, X. Jin, X. Wen, V. Sahajwalla, V. Chen, H. Bustamante, R. Joshi, Application of graphene oxide membranes for removal of natural organic matter from water, Carbon, 129 (2018) 415-419.

[146] L. Chen, J.-H. Moon, X. Ma, L. Zhang, Q. Chen, L. Chen, R. Peng, P. Si, J. Feng, Y. Li, High performance graphene oxide nanofiltration membrane prepared by electrospraying for wastewater purification, Carbon, (2018).

[147] R. Joshi, P. Carbone, F.-C. Wang, V.G. Kravets, Y. Su, I.V. Grigorieva, H. Wu, A.K. Geim, R.R. Nair, Precise and ultrafast molecular sieving through graphene oxide membranes, Science, 343 (2014) 752-754.

[148] W.S. Hummers Jr, R.E. Offeman, Preparation of graphitic oxide, Journal of the American Chemical Society, 80 (1958) 1339-1339.

[149] D.R. Dreyer, S. Park, C.W. Bielawski, R.S. Ruoff, The chemistry of graphene oxide, Chemical Society Reviews, 39 (2010) 228-240.

[150] P. Sun, K. Wang, H. Zhu, Recent Developments in Graphene‐Based Membranes: Structure, Mass‐Transport Mechanism and Potential Applications, Advanced Materials, (2016).

[151] C.-N. Yeh, K. Raidongia, J. Shao, Q.-H. Yang, J. Huang, On the origin of the stability of graphene oxide membranes in water, Nature chemistry, 7 (2015) 166-170.

[152] Y.C. Kim, M. Elimelech, Adverse impact of feed channel spacers on the performance of pressure retarded osmosis, Environmental science & technology, 46 (2012) 4673-4681.

[153] X. Song, Z. Liu, D.D. Sun, Nano gives the answer: breaking the bottleneck of internal concentration polarization with a nanofiber composite forward osmosis membrane for a high water production rate, Advanced materials, 23 (2011) 3256-3260.

[154] N.Y. Yip, M. Elimelech, Performance limiting effects in power generation from salinity gradients by pressure retarded osmosis, Environmental Science & Technology, (2011).

[155] S. Loeb, L. Titelman, E. Korngold, J. Freiman, Effect of porous support fabric on osmosis through a Loeb-Sourirajan type asymmetric membrane, Journal of Membrane Science, 129 (1997) 243-249.

[156] X. Song, Z. Liu, D.D. Sun, Energy recovery from concentrated seawater brine by thin-film nanofiber composite pressure retarded osmosis membranes with high power density, Energy & Environmental Science, 6 (2013) 1199-1210.

[157] C.Y. Tang, Q. She, W.C. Lay, R. Wang, A.G. Fane, Coupled effects of internal concentration polarization and fouling on flux behavior of forward osmosis membranes during humic acid filtration, Journal of membrane science, 354 (2010) 123-133.

[158] S. Chou, R. Wang, A.G. Fane, Robust and high performance hollow fiber membranes for energy harvesting from salinity gradients by pressure retarded osmosis, Journal of membrane science, 448 (2013) 44-54.

[159] J.R. McCutcheon, M. Elimelech, Influence of concentrative and dilutive internal concentration polarization on flux behavior in forward osmosis, Journal of Membrane Science, 284 (2006) 237-247.

[160] G.T. Gray, J.R. McCutcheon, M. Elimelech, Internal concentration polarization in forward osmosis: role of membrane orientation, Desalination, 197 (2006) 1-8.

[161] W. Koros, G. Fleming, S. Jordan, T. Kim, H. Hoehn, Polymeric membrane materials for solution-diffusion based permeation separations, Progress in Polymer Science, 13 (1988) 339-401.

[162] M. Elimelech, W.A. Phillip, The future of seawater desalination: energy, technology, and the environment, science, 333 (2011) 712-717.

[163] N.Y. Yip, A. Tiraferri, W.A. Phillip, J.D. Schiffman, L.A. Hoover, Y.C. Kim, M. Elimelech, Thin-film composite pressure retarded osmosis membranes for sustainable power generation from salinity gradients, Environmental science & technology, (2011).

[164] G.M. Geise, H.B. Park, A.C. Sagle, B.D. Freeman, J.E. McGrath, Water permeability and water/salt selectivity tradeoff in polymers for desalination, Journal of Membrane Science, 369 (2011) 130-138.

[165] K.L. Hickenbottom, J. Vanneste, M. Elimelech, T.Y. Cath, Assessing the current state of commercially available membranes and spacers for energy production with pressure retarded osmosis, Desalination, 389 (2016) 108-118.

[166] Q. She, J. Wei, N. Ma, V. Sim, A.G. Fane, R. Wang, C.Y. Tang, Fabrication and characterization of fabric-reinforced pressure retarded osmosis membranes for osmotic power harvesting, Journal of Membrane Science, 504 (2016) 75-88.

[167] A. Akbari, P. Sheath, S.T. Martin, D.B. Shinde, M. Shaibani, P.C. Banerjee, R. Tkacz, D. Bhattacharyya, M. Majumder, Large-area graphene-based nanofiltration membranes by shear alignment of discotic nematic liquid crystals of graphene oxide, Nature communications, 7 (2016) 10891.

[168] Y.-H. Xi, J.-Q. Hu, Z. Liu, R. Xie, X.-J. Ju, W. Wang, L.-Y. Chu, Graphene oxide membranes with strong stability in aqueous solutions and controllable lamellar spacing, ACS applied materials & interfaces, 8 (2016) 15557-15566.

[169] S. Park, K.-S. Lee, G. Bozoklu, W. Cai, S.T. Nguyen, R.S. Ruoff, Graphene oxide papers modified by divalent ions—enhancing mechanical properties via chemical cross-linking, ACS nano, 2 (2008) 572-578.

[170] C. Chen, Q.H. Yang, Y. Yang, W. Lv, Y. Wen, P.X. Hou, M. Wang, H.M. Cheng, Self‐Assembled Free‐Standing Graphite Oxide Membrane, Advanced materials, 21 (2009) 3007-3011.

[171] S. Park, D.A. Dikin, S.T. Nguyen, R.S. Ruoff, Graphene oxide sheets chemically cross-linked by polyallylamine, The Journal of Physical Chemistry C, 113 (2009) 15801-15804.

[172] K.W. Putz, O.C. Compton, M.J. Palmeri, S.T. Nguyen, L.C. Brinson, High‐nanofiller‐content graphene oxide–polymer nanocomposites via vacuum‐assisted self‐assembly, Advanced Functional Materials, 20 (2010) 3322-3329.

[173] S. Stankovich, D.A. Dikin, O.C. Compton, G.H. Dommett, R.S. Ruoff, S.T. Nguyen, Systematic post-assembly modification of graphene oxide paper with primary alkylamines, Chemistry of Materials, 22 (2010) 4153-4157.

[174] H. Huang, Z. Song, N. Wei, L. Shi, Y. Mao, Y. Ying, L. Sun, Z. Xu, X. Peng, Ultrafast viscous water flow through nanostrand-channelled graphene oxide membranes, Nature communications, 4 (2013) 2979.

[175] W.L. Xu, C. Fang, F. Zhou, Z. Song, Q. Liu, R. Qiao, M. Yu, Self-Assembly: A Facile Way of Forming Ultrathin, High-Performance Graphene Oxide Membranes for Water Purification, Nano letters, 17 (2017) 2928-2933.

[176] A. Richter, J.P. Burrows, H. Nüß, C. Granier, U. Niemeier, Increase in tropospheric nitrogen dioxide over China observed from space, Nature, 437 (2005) 129-132.

[177] S. Solomon, G.-K. Plattner, R. Knutti, P. Friedlingstein, Irreversible climate change due to carbon dioxide emissions, Proceedings of the national academy of sciences, 106 (2009) 1704-1709.

[178] R.E. Sims, H.-H. Rogner, K. Gregory, Carbon emission and mitigation cost comparisons between fossil fuel, nuclear and renewable energy resources for electricity generation, Energy policy, 31 (2003) 1315-1326.

[179] H. Herring, Energy efficiency—a critical view, Energy, 31 (2006) 10-20.

[180] T.-C. Hung, T. Shai, S.K. Wang, A review of organic Rankine cycles (ORCs) for the recovery of low-grade waste heat, Energy, 22 (1997) 661-667.

[181] S. Lin, N.Y. Yip, T.Y. Cath, C.O. Osuji, M. Elimelech, Hybrid pressure retarded osmosis–membrane distillation system for power generation from low-grade heat: Thermodynamic analysis and energy efficiency, Environmental science & technology, 48 (2014) 5306-5313.

[182] J. Holman, Perspective: Waste heat to power 炯 still waiting for a breakthrough, Renewable Energy Strategies: Perspective, (2011) EI229456.

[183] X. Zhu, M. Rahimi, C.A. Gorski, B. Logan, A Thermally‐Regenerative Ammonia‐Based Flow Battery for Electrical Energy Recovery from Waste Heat, ChemSusChem, 9 (2016) 873-879.

[184] E. Barbier, Geothermal energy technology and current status: an overview, Renewable and Sustainable Energy Reviews, 6 (2002) 3-65.

[185] X. Luo, X. Cao, Y. Mo, K. Xiao, X. Zhang, P. Liang, X. Huang, Power generation by coupling reverse electrodialysis and ammonium bicarbonate: Implication for recovery of waste heat, Electrochemistry Communications, 19 (2012) 25-28.

[186] M. Rahimi, A.P. Straub, F. Zhang, X. Zhu, M. Elimelech, C.A. Gorski, B.E. Logan, Emerging electrochemical and membrane-based systems to convert low-grade heat to electricity, Energy & Environmental Science, 11 (2018) 276-285.

[187] X. Tong, B. Zhang, Y. Fan, Y. Chen, Mechanism exploration of ion transport in nanocomposite cation exchange membranes, ACS Applied Materials & Interfaces, 9 (2017) 13491-13499.

[188] N.Y. Yip, D. Brogioli, H.V. Hamelers, K. Nijmeijer, Salinity Gradients for Sustainable Energy: Primer, Progress, and Prospects, Environmental science & technology, 50 (2016) 12072-12094.

[189] A. Tamburini, M. Tedesco, A. Cipollina, G. Micale, M. Ciofalo, M. Papapetrou, W. Van Baak, A. Piacentino, Reverse electrodialysis heat engine for sustainable power production, Applied Energy, 206 (2017) 1334-1353.

[190] H. Gong, D.D. Anastasio, K. Wang, J.R. McCutcheon, Finding better draw solutes for osmotic heat engines: Understanding transport of ions during pressure retarded osmosis, Desalination, 421 (2017) 32-39.

[191] S. Loeb, Method and apparatus for generating power utilizing pressure-retarded-osmosis, in, Google Patents, 1975.

[192] G. Han, Q. Ge, T.-S. Chung, Conceptual demonstration of novel closed-loop pressure retarded osmosis process for sustainable osmotic energy generation, Applied Energy, 132 (2014) 383-393.

[193] R. Long, B. Li, Z. Liu, W. Liu, Hybrid membrane distillation-reverse electrodialysis electricity generation system to harvest low-grade thermal energy, Journal of Membrane Science, 525 (2017) 107-115.

[194] E. Shaulsky, C. Boo, S. Lin, M. Elimelech, Membrane-based osmotic heat engine with organic solvent for enhanced power generation from low-grade heat, Environmental science & technology, 49 (2015) 5820-5827.

[195] K.L. Hickenbottom, J. Vanneste, T.Y. Cath, Assessment of alternative draw solutions for optimized performance of a closed-loop osmotic heat engine, Journal of Membrane Science, 504 (2016) 162-175.

[196] N.Y. Yip, A. Tiraferri, W.A. Phillip, J.D. Schiffman, M. Elimelech, High performance thin-film composite forward osmosis membrane, Environmental science & technology, (2010).

[197] Z.P. Smith, B.D. Freeman, Graphene Oxide: A New Platform for High‐Performance Gas‐and Liquid‐Separation Membranes, Angewandte Chemie International Edition, 53 (2014) 10286-10288.

[198] K. Huang, G. Liu, Y. Lou, Z. Dong, J. Shen, W. Jin, A graphene oxide membrane with highly selective molecular separation of aqueous organic solution, Angewandte chemie international edition, 53 (2014) 6929-6932.

[199] C.A. Amadei, A. Montessori, J.P. Kadow, S. Succi, C.D. Vecitis, Role of Oxygen Functionalities in Graphene Oxide Architectural Laminate Subnanometer Spacing and Water Transport, Environmental Science & Technology, 51 (2017) 4280-4288.

[200] N.Y. Yip, M. Elimelech, Performance limiting effects in power generation from salinity gradients by pressure retarded osmosis, Environmental science & technology, 45 (2011) 10273-10282.

[201] F. Rashidi, N.S. Kevlich, S.A. Sinquefield, M.L. Shofner, S. Nair, Graphene Oxide Membranes in Extreme Operating Environments: Concentration of Kraft Black Liquor by Lignin Retention, ACS Sustainable Chemistry & Engineering, 5 (2016) 1002-1009.

[202] L.A. Hoover, J.D. Schiffman, M. Elimelech, Nanofibers in thin-film composite membrane support layers: Enabling expanded application of forward and pressure retarded osmosis, Desalination, 308 (2013) 73-81.

[203] G. Han, T.S. Chung, Robust and high performance pressure retarded osmosis hollow fiber membranes for osmotic power generation, AIChE Journal, 60 (2014) 1107-1119.

[204] D. Chen, H. Feng, J. Li, Graphene oxide: preparation, functionalization, and electrochemical applications, Chemical reviews, 112 (2012) 6027-6053.

[205] S. Yu, G.M. Chow, Carboxyl group (–CO 2 H) functionalized ferrimagnetic iron oxide nanoparticles for potential bio-applications, Journal of Materials Chemistry, 14 (2004) 2781-2786.

[206] L. Wang, J. Zhang, R. Zhao, Y. Li, C. Li, C. Zhang, Adsorption of Pb (II) on activated carbon prepared from Polygonum orientale Linn.: kinetics, isotherms, pH, and ionic strength studies, Bioresource Technology, 101 (2010) 5808-5814.

[207] Y. Xu, X. Peng, C.Y. Tang, Q.S. Fu, S. Nie, Effect of draw solution concentration and operating conditions on forward osmosis and pressure retarded osmosis performance in a spiral wound module, Journal of Membrane Science, 348 (2010) 298-309.

[208] K. Kwon, B.H. Park, D.H. Kim, D. Kim, Parametric study of reverse electrodialysis using ammonium bicarbonate solution for low-grade waste heat recovery, Energy Conversion and Management, 103 (2015) 104-110.

[209] J. Lee, H.-R. Chae, Y.J. Won, K. Lee, C.-H. Lee, H.H. Lee, I.-C. Kim, J.-m. Lee, Graphene oxide nanoplatelets composite membrane with hydrophilic and antifouling properties for wastewater treatment, Journal of membrane science, 448 (2013) 223-230.

[210] Z. Xu, J. Zhang, M. Shan, Y. Li, B. Li, J. Niu, B. Zhou, X. Qian, Organosilane-functionalized graphene oxide for enhanced antifouling and mechanical properties of polyvinylidene fluoride ultrafiltration membranes, Journal of Membrane Science, 458 (2014) 1-13.

[211] D.J. Lewis, T.M. Day, J.V. MacPherson, Z. Pikramenou, Luminescent nanobeads: attachment of surface reactive Eu (III) complexes to gold nanoparticles, Chemical communications, (2006) 1433-1435.

[212] N.I. Abu-Lail, T.A. Camesano, Role of Ionic Strength on the Relationship of Biopolymer Conformation, DLVO Contributions, and Steric Interactions to Bioadhesion of P seudomonas p utida KT2442, Biomacromolecules, 4 (2003) 1000-1012.

[213] J. Schenkel, J. Kitchener, A test of the Derjaguin-Verwey-Overbeek theory with a colloidal suspension, Transactions of the Faraday Society, 56 (1960) 161-173.

[214] Agglomerative hierarchical cluster tree - MATLAB linkage (https://www.mathworks.com/help/stats/linkage.html?requestedDomain=www.mathwork

s.com;%20https://www.mathworks.com/help/stats/cluster.html&requestedDomain=www.mathworks.com), in.

[215] J.R. McCutcheon, R.L. McGinnis, M. Elimelech, Desalination by ammonia–carbon dioxide forward osmosis: influence of draw and feed solution concentrations on process performance, Journal of membrane science, 278 (2006) 114-123.